



Office de la propriété
intellectuelle
du Canada

Un organisme
d'Industrie Canada

Canadian
Intellectual Property
Office

An Agency of
Industry Canada

PCT/CA 2005/000162

09 FEBRUARY 2005 09:02:05

REC'D 10 MAR 2005

WIPO PCT

*Bureau canadien
des brevets*
Certification

*Canadian Patent
Office*
Certification

La présente atteste que les documents
ci-joints, dont la liste figure ci-dessous,
sont des copies authentiques des docu-
ments déposés au Bureau des brevets.

This is to certify that the documents
attached hereto and identified below are
true copies of the documents on file in
the Patent Office.

Specification and Drawings, as originally filed, with Application for Patent Serial No:
2,457,171, on February 9, 2004, by **CENTRE HOSPITALIER DE L'UNIVERSITÉ DE
MONTREAL-CHUM**, assignee of Roch Listz Maurice, Guy Cloutier, Jacques Ohayon and
Gilles Soulez, for "Imaging Apparatus and Methods".

**PRIORITY
DOCUMENT**
SUBMITTED OR TRANSMITTED IN
COMPLIANCE WITH RULE 17.1(a) OR (b)

[Signature]
Agent certificateur/Certifying Officer

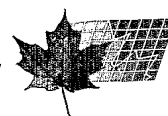
December 2, 2004

Date

Canada

(CIPO 68)
31-03-04

OPIC



CIPC

ABSTRACT

The present invention relates to a computer-aided method to estimate the coil volumes using only two orthogonal angiographic projections and Non-invasive Vascular Elastography: Theoretical Framework. The invention relates to the validation on tissue mimicking phantoms of non-invasive elasticity imaging in small vessels. The Lagrangian speckle tissue model estimator was used to assess the 2-D-strain tensor, and the composite Von Mises elastograms were computed. The invention also relates to a model-based approach devoted to endovascular elastography (EVE). A model-based approach is proposed and the Lagrangian speckle model estimator is provided and the theoretical framework is validated. Moreover, the invention relates to the *in vitro* experiments using excised human carotid artery to validate the potential of endovascular elastography to detect hard plaques.

IMAGING APPARATUS AND METHODS

FIELD OF THE INVENTION

This invention relates generally to the field of ultrasound electrography and more particularly, but not exclusively, to a non-invasive ultrasound elastography system and a method for characterising the mechanical properties of superficial arteries.

BACKGROUND OF THE INVENTION

10

In the early nineties, Ophir *et al.* introduced elastography, which is defined as biological tissue elasticity imaging. Primary objectives of elastography were to complement B-mode ultrasound as a screening method to detect hard areas in the breast. Basically, the tissue under inspection is externally compressed and the displacement between pairs of pre- and post-compression radio frequency (RF) lines is estimated using cross-correlation analysis. The strain profile in the tissue is then determined from the gradient of the axial displacement field.

1.1 Non-invasive vascular elastography (NIVE)

20

Elastography has also found application in vessel wall characterization. However, vascular elastography is invasive; it is known in the literature as intravascular elastography or, sometimes, as endovascular elastography (EVE). In EVE, the vascular tissue is compressed by applying a force from within the lumen. Indeed, the compression can be induced by the normal cardiac pulsation or by using a compliant intravascular angioplasty balloon.

To validate the feasibility of EVE, phantom studies have been conducted. In most cases, tissue-mimicking phantoms with typical morphology and hardness topology synthesizing atherosclerotic vessels were constructed. de Korte *et al.* concluded that EVE may allow identifying hard and soft plaques independently of the

echogeneity contrast between the plaque and the vessel wall. The potential of such an approach was emphasized by the fact that it provides information that may be unavailable from intravascular B-mode ultrasound (IVUS) alone.

In vitro studies with excised vessels were also conducted for further validation of EVE feasibility. For instance, de Korte *et al.* computed elastograms from diseased human femoral and coronary arteries. They found different strain values between fibrous, fibro-fatty and fatty plaques, indicating the potential of EVE to distinguish different plaque constituents. Such results were compared with IVUS echograms and were corroborated with histology. They found that the elastograms were capable of demarcating regions within the plaque representing differences in strain, whereas in IVUS echograms, these regions could not be discriminated. Using excised postmortem carotid arteries, similar results were recently observed.

1.2 Non-invasive vascular elastography (NIVE)

So far, vascular elastography is invasive. Its clinical application is restricted to a complementary tool to assist IVUS echograms in pre-operative lesion assessments and to plan endovascular therapy. Our group recently investigated the potential of elastography to non-invasively characterize mechanical properties of superficial arteries; the approach was labeled as "non-invasive vascular elastography" (NIVE).

Investigating the forward problem in NIVE, it was shown that motion parameters might be difficult to interpret; that is because tissue motion occurs radially within the vessel wall while the ultrasound beam propagates axially. As a consequence of that, the elastograms are subjected to hardening and softening artifacts, which are to be counteracted. With NIVE, the Von Mises coefficient was proposed as a new parameter to circumvent such mechanical artifacts and to appropriately characterize the vessel wall. The Lagrangian estimator was used, that is because it provides the full 2D-strain tensor necessary to compute the Von Mises

coefficient. The theoretical model was validated with biomechanical simulations of the vascular wall properties.

Simultaneously to the NIVE approach development, another group addressed the feasibility of strain imaging of internal deformation. A tissue-like gelatin elasticity-flow phantom was used to develop ultrasonic strain imaging for the detection of internal pulsatile deformations. Such an imaging technique also was applied *in vivo* to monitor deformation in tissues surrounding the normal brachial artery. Results suggested that the method may be feasible to detect regional artery elasticity changes caused by the formation of plaques and calcification. Although this last study investigated the deformation of soft tissues surrounding an artery, the current study represents the first *in vitro* experimental results on the non-invasive characterization of small vessel mechanical properties.

SUMMARY OF THE INVENTION

According to the present invention there is provided a method for characterising the mechanical properties of tissues in small vessels using the Non-Invasive Ultrasound Elastography (NIVE), the method comprising the steps of :

- Acquiring pre- and post- deformation images
- Using the Lagrangian speckle model estimator to assess the 2-D strain tensor
- Computing the Von Mises elastograms
- Modelling the tissue mechanical characteristics

According to the present invention there is also provided an apparatus for investigating the feasibility of NIVE for characterising tissues in small vessels.

The feasibility of NIVE is investigated for the specific purpose of studying small vessels in humans and transgenic rodents with vascular diseases. Experiments

were conducted on tissue-mimicking phantoms. The equivalent vessel wall was made of polyvinyl alcohol cryogel (PVA-C) and it was inserted into a close-loop pressurized device.

The apparatus and the acquisition system are detailed in the section below.

DETAILED DESCRIPTION OF A PREFERRED EMBODIMENT OF THE INVENTION

2.1 Experimental set-up

- 10 Figure 1 gives an overview of the experimental set-up used to produce mechanical deformation of the PVA-C vessel-mimicking phantom, and the procedure utilized to collect RF ultrasound raw data allowing to compute vascular elastograms. A mixture of water-glycerol was circulated in the flow phantom. The height difference between the top (1) and bottom reservoirs (9) allowed to adjust the gravity driven flow rate and static pressure within the lumen of the phantom (3). A peristaltic pump (10) was used to circulate the fluid from the bottom to the top reservoir. The flow rate (7) was measured with an electromagnetic flowmeter (Cliniflow II, model FM 701D), and the pressure (8) was monitored by a MDE Escort instrument (Uniflow pressure transducer from Baxter). As illustrated in Figure 1, the flow
- 20 phantom was not directly connected to the tubing of the top reservoir to facilitate the small incremental pressure step adjustments necessary to obtain correlated deformation of the RF signals within the PVA-C vessel wall. As described later on, the elastograms were computed from RF images obtained at two incremental pressure values.

2.2 High frequency imaging system (labels 2 and 4 on Figure 1)

To allow computing vascular elastograms of small vessels, a high resolution ultrasound system with access to the raw RF data was required (Ultrasound biomicroscope, Visualsonics, VS-40, Toronto, Canada). This system was

equipped with a single element oscillating transducer with a central frequency of 32 MHz, f-number = 2, diameter = 3 mm, focal length = 6 mm, and bandwidth at -6 dB of 110 %. As recently reported, the axial and lateral resolutions of the instrument are 30 μ m and 70 μ m, respectively. A transmit frequency of 40 MHz was used and the frame rate was 8 Hz. The bandpass filter was selected to optimize the bandwidth of the received echoes, and thus the axial resolution.

2.3 Vascular phantom (label 3 on Figure 1)

10 As shown in Figure 2, the PVA-C vessel of the flow phantom was positioned between two watertight connectors, in a Plexiglas box filled with degassed water at room temperature. Rubber o-rings were used to tight the PVA-C vessel onto Plexiglas tubes at both extremities.

As performed by others, the tissue-mimicking vessel was made of PVA-C (polyvinyl alcohol cryogel). This biogel solidifies and acquires its mechanical rigidity by increasing the number of freeze/thaw cycles. The freeze/thaw cycles modified the structure of the material by increasing the reticulation of fibers. It was shown that the elastic and acoustic properties of PVA-C are in the range of values found for soft biological tissues. More specifically, Chu and Rutt demonstrated that the stress-strain relationship is very close to that of a pig aorta.

20

The vessel-mimicking phantom investigated had a 1.5-mm lumen diameter, 1.5-mm wall thickness, and 52-mm length. A 1.5% in weight of Sigmacell was added to the PVA-C to provide acoustical scatterers. The phantom simulated a double-layer vessel wall of approximately 0.75-mm thickness each. The stiffness of the inner wall was made softer by controlling the number and temperature of the freeze/thaw cycles. For this study, the numbers of cycles were set at 2 and 8 for the inner and the outer portions of the wall, respectively.

Figure 3 shows a schematic representation of both moulds that were used to produce the double-layer vessel-mimicking phantom. At a first instance, PVA-C was poured between the first and second templates; that underwent 6 freeze/thaw cycles to provide the external layer. At a second instance, liquid PVA-C was poured between the second and third templates; that underwent 2 freeze/thaw cycles to provide the double-layer vessel-mimicking phantom.

2.4 Acquisition protocol

10 The ultrasound biomicroscope is a PC-based system (label 4 on Figure 1) providing RF data that were pre-amplified (Panametrics, model 5900PR, label 5 on Figure 1) before analog-to-digital conversion. After amplification, the signals were digitized at 500 MHz with an 8-bit format by using a PC-based acquisition board (Compuscope, Gage-Techmatron, model CS-8500, label 6 on Figure 1).

2.5 Methods

20 NIVE is based on the Lagrangian speckle model estimator (LSME) developed already. The LSME is a 2D model-based estimator that allows computing the full 2D-strain tensor. As illustrated in Figure 4, in NIVE, the observer's coordinate system is the Cartesian (x,y) -plane while the motion coordinate system is the radial (r,φ) -plane. In such a situation, the parameters of an estimator are expected to be very difficult to interpret. The approach thus assumes a constant deformation for small regions of interest (ROI), equivalent to W_{mn} in Figure 4. If translation is appropriately compensated for, this leads to a simple linear transformation (LT) of the ROI. The LT matrix relates the strain tensor ϵ as follows:

$$\begin{aligned}
 LT &= \begin{bmatrix} m_1 & m_2 \\ m_3 & m_4 \end{bmatrix} \\
 \Delta &= \begin{bmatrix} \Delta_{11} & \Delta_{12} \\ \Delta_{21} & \Delta_{22} \end{bmatrix} = \begin{bmatrix} 1-m_1 & m_2 \\ m_3 & 1-m_4 \end{bmatrix} \\
 \Rightarrow \varepsilon &= \begin{bmatrix} \Delta_{11} & \frac{\Delta_{12} + \Delta_{21}}{2} \\ \frac{\Delta_{12} + \Delta_{21}}{2} & \Delta_{22} \end{bmatrix}
 \end{aligned} \tag{1}$$

The Von Mises (VM) coefficient was derived from the strain tensor ε (Eq. 1) and it was proposed to counteract elastogram mechanical artifacts (such as hardening and softening artifacts). The VM coefficient can be expressed as:

$$\xi = \sqrt{\Delta_{11}^2 + \Delta_{22}^2 - \Delta_{11}\Delta_{22} + \frac{3}{4}(\Delta_{12} + \Delta_{21})^2} \tag{2}$$

Results

10 This section reports preliminary results for the double-layer phantom presented above. The pre-load static pressure was set at 3 mmHg (flow-rate of 70 ml/min), and pre-motion radio-frequency (RF) images were acquired. The static pressure was then increased at 7 mmHg, and post-motion RF images were recorded. Those RF images had a dimension of 8 mm \times 8 mm, that is 5888 samples \times 513 RF lines. To apply the LSME, a measurement-window (W_{mn} in Figure 4) of 272 μ m \times 312 μ m (200 samples \times 20 RF lines) was chosen. The motion was assessed for windows W_{mn} with 85 % and 85 % axial and lateral overlaps, respectively.

20 Pre- and post-motion images were pre-processed to compensate for motion of the experimental apparatus, and then correlation coefficients were computed. It was then possible to examine the most relevant data among all experiments performed. Figures 5a and 5b show pre- and post-motion B- mode images; they are displayed for illustration purpose since computations were done on the RF images. Figure 5c presents a map of the correlation coefficient between the pre- and post-motion RF images; an average close to 0.6 clearly allows demarcating

the vessel wall from the lumen and the surrounding water environment. Figure 5d shows the composite elastogram (ξ in Eq. 2) as computed by the LSME. Because of the limited lateral resolution of the imaging system, motion estimates seem specifically reliable in the axial portion of ξ , delimited with dotted lines. For clarity, this axial part of the image is displayed in Figure 5e, showing clearly the inner layer (softer) with higher strain values (close to 3 %), whereas the outer layer (harder) shows lower strain values (around 1%) as expected. This observation is more explicit in Figure 5f, where an average of 20 axial lines chosen in the middle of ξ is plotted.

10

This invention addressed the feasibility of non-invasive vascular elastography for the purpose of investigating small vessels in humans and transgenic rodents with vascular diseases. Experiments were performed *in vitro* on a double-layer vessel-mimicking phantom of 4.5-mm external diameter. The Lagrangian speckle model estimator was used to assess the 2D-strain tensor, and the composite Von Mises elastogram was computed. The two-layer vessel walls were clearly identifiable. The feasibility of NIVE for small vessel elasticity imaging was demonstrated. To our knowledge, these are the first experimental results reported on the non-invasive characterization of small vessel mechanical properties; and this was made possible with the use of a high resolution ultrasound system by Visualsonics. It may be noted, however, that the limited lateral resolution of the ultrasound system restricts the strain contrast mainly in an axial region where tissue motion mostly runs parallel to the ultrasound beam.

20

FIELD OF THE INVENTION

This invention relates generally to the field of endovascular ultrasound elastography (EVE) and more particularly, but not exclusively, to a model-based approach to investigate EVE.

BACKGROUND OF THE INVENTION

Intravascular elastography, or equivalently endovascular elastography (EVE), was introduced in the late nineties as a new imaging modality that aims to outline the elastic properties of vessel walls. In EVE, the vascular tissue is compressed by applying a force from within the lumen. Indeed, the compression can be induced by the normal cardiac pulsation or by using a compliant intravascular angioplasty balloon. Phantom studies were conducted to validate the feasibility of EVE. In most cases, tissue-mimicking phantoms with typical morphology and hardness topology synthesizing atherosclerotic vessels were constructed. de Korte et al. (1997) demonstrated that EVE may allow identifying hard and soft plaques independently of the echogeneity contrast between the plaque and the vessel wall. The potential of such an approach was then emphasized by the fact that it provides information that may be unavailable from IVUS B-scans alone. At the same period, Soualmi et al. (1997) used finite element analysis to investigate vessel wall elasticity images and to demonstrate the feasibility of EVE.

In vitro studies with excised vessels were also conducted to further validate EVE. For instance, de Korte et al. (1998, 2000a) computed elastograms from diseased human femoral and coronary arteries. They found different strain values between fibrous, fibro-fatty and fatty plaques, indicating the potential of EVE to distinguish different plaque constituents. Such results were compared with IVUS echograms and were corroborated with histology. They found that the elastograms were capable of demarcating regions within the plaque representing differences in

strain, whereas in IVUS B-scans, these regions could not be discriminated. Similar results were observed by Brusseau et al. (2001) using excised postmortem carotid arteries. In vitro EVE experimentation was also conducted by Wan et al. (2001). They used an optical flow-based algorithm to estimate the displacement field from B-mode data collected from porcine arteries; they computed the elasticity modulus distributions by solving a mechanical inverse problem. While low spatial resolution of envelope data remains a limitation, the method seemed encouraging because of the highest accessibility of B-mode compared to radio-frequency (RF) instrumentation.

10

However, in vivo, the position of the catheter in the lumen is generally off center and may move in response to the flow pulsatility; moreover, the lumen geometry is often not perfectly circular. In such conditions, the ultrasound beam does not run parallel with tissue displacements, and appropriate coordinate systems are required to model both the ultrasound propagation and the tissue motion. A consequence of this misalignment is that substantial decorrelation between the pre- and the post-tissue-compression echoes is induced and must be compensated for. Ryan and Foster (1997) then proposed to use a 2D correlation-based speckle tracking method to compute vascular elastograms. Additionally, to circumvent catheter movement, Shapo et al. (1996a, 1996b) suggested to compute the tissue motion in the reference frame of the lumen's geometric center of the angioplasty balloon. As this reference frame depends only on the balloon shape, it can remove artifacts associated with probe motion. Both of those phantom investigations tended to demonstrate the feasibility of EVE in the presence of motion artifacts, and its potential to provide new diagnosis information that may help in the functional assessment of atherosclerosis.

20

30

Another strategy was proposed by de Korte et al. (2000b) to minimize artifacts due to catheter motion; it consisted in using pre- and post-motion images near end-diastole for a pressure differential of approximately 5 mmHg. The computed in vivo elastograms could detect an area composed of hardened material, which was

corroborated with IVUS B-scans that revealed a large calcified area. This last method may become a standard procedure if one considers EVE without the use of an angioplasty balloon.

So far, EVE appears a very attractive and promising tool to characterize the mechanical properties of vessel walls; but, in return, it is potentially limited by signal decorrelation. This paper describes a new model-based approach for strain computation in EVE. Assuming that speckle can be seen as a material property, tissue motion is investigated in the Lagrangian coordinate system (or, equivalently, in the material coordinate system) instead of the Eulerian coordinate system. The Lagrangian speckle model estimator (LSME) (Maurice and Bertrand, 1999a) is then used to assess tissue motion. The optical flow equations are derived and are integrated in the LSME process to provide accurate tissue motion estimates. The proposed method is implemented using the Levenberg-Marquardt algorithm. The theoretical model is validated with biomechanical simulations of the vascular wall properties.

20 SUMMARY OF THE INVENTION

According to the present invention there is provided a model-based method devoted to endovascular elastography, the method comprising the steps of :

A) performing a modeling in performing the sub-steps of :

A1) modeling the polar static-image formation;

A2) modeling the tissue-motion;

A3) modeling the polar dynamic-image-formation;

B) estimating tissue motion in performing the sub-steps of :

B1) assuming speckle is a material property;

B2) providing LSI (Lagrangian speckle images);

B3) using the Lagrangian Speckle Model Estimator (LSME) to assess tissue motion;

B4) solving a non linear minimization problem;

B5) using the optical flow equations;

thereby providing an accurate tissue motion estimate for providing an elastogram of the tissue.

10 According to the present invention, there is also provided an apparatus for characterising the mechanical properties of tissues, the apparatus comprising :

- a CVIS ultrasound scanner;
- a 30-40 MHz mechanical rotating single element transducer;
- an oscilloscope;
- a pressuring system; and
- a computer.

10 Intravascular ultrasound (IVUS) is known to be the reference tool for pre-operative vessel lesion assessments and for endovascular therapy planning. Nevertheless, IVUS echograms only provide subjective information about vessel wall lesions. Since changes in the vascular tissue stiffness are characteristic of vessel pathologies, catheter-based endovascular ultrasound elastography (EVE) was
20 proposed to outline the elastic properties of vessel walls. In EVE, the catheter is subjected to cyclic movements in the lumen because of the pulsatile blood flow motion; additionally, its position may be off center, and the lumen geometry is generally not circular. As a result of those particularities, the tissue displacements

and the ultrasound beam may misalign and cause substantial decorrelation between the pre- and the post-tissue-motion signals. Accordingly, EVE does require robust motion estimators. In this paper, a model-based approach is proposed to investigate EVE; it considers the speckle as a material property. Such an assumption leads to the derivation of the optical flow equations, which are suitably combined with the Lagrangian speckle model estimator to provide accurate tissue motion assessments. The theoretical framework is validated with simulated RF data of vessel wall pathologies. Results show the potential of the method to dissociate atherosclerotic plaques and healthy vascular tissue.

10

The method and the apparatus will be detailed in the section below.

BRIEF DESCRIPTION OF THE DRAWINGS

Figure 6.- Schematic illustration of the image acquisition process in EVE. The transducer is placed at the tip of the catheter and cross-sectional imaging of the vessel is generated by sequentially sweeping the ultrasound beam in a 360° angle. In this ideal situation, the ultrasound beam runs parallel with the vascular tissue motion, i.e. in the (r, ϕ) coordinate system.

20

Figure 7.- Image-formation model for a 20 MHz polar scan system; a) shows the beam profile as a function of depth; b) presents the simulated polar B-mode image for an homogenous vessel section; c) is the IVUS simulated image.

Figure 8.- Schematic representation of an "ideal" plaque. The Young's modulus for the normal vascular tissue was 80 kPa, while the plaque (three times stiffer) was set at 240 kPa. To emulate boundary conditions as provided by the surrounding environment, the Young's modulus for the surrounding tissue was set at 1000 kPa.

30

Figure 9.- a) In vivo IVUS cross-sectional image of a coronary plaque; b) 2D finite element mesh of the unloaded real geometry with spatial distribution of the plaque

constituents. The Young's modulus for the healthy vascular tissue (or adventicia & media) was 80 kPa, while the dense fibrosis (three times stiffer) was set at 240 kPa, and the cellular fibrosis at 24 kPa (ten times softer than the dense fibrosis).

Figure 10.- Schematic implementation of the polar dynamic image-formation model.

Figure 11.- a) Theoretical radial strain elastogram for the idealized plaque; b) theoretical radial strain distributions along the vertical and horizontal lines specified on (a); c) radial strain elastogram as computed with the LSME; d) LSME radial strain distributions along the vertical and horizontal lines specified on (c).

Figure 12.- a) Strain-decay-compensated LSME elastogram, showing substantial contrast improvement between hard and soft materials; b) vertical 1D plot from the elastogram showing a contrast ratio close to 3 between the plaque and the normal vascular tissue, as it can be expected; c) horizontal 1D plot from the elastogram, showing effective strain decay compensation, and thus a substantial improvement of the contrast ratio.

Figure 13.- a) Theoretical radial strain elastogram for the real plaque, showing very complex strain patterns; b) and c) show vertical and horizontal 1D plots from the elastogram, respectively. Strain decay is specifically observed at the inner portion of the vessel wall.

Figure 14.- a) Radial strain elastogram as computed with the LSME for the real plaque; b) and c) vertical and horizontal 1D plots from the elastogram, respectively. Because of strain decay, there is not a clear demarcation between cellular and dense fibroses, specifically in c).

Figure 15.- a) Strain-decay-compensated LSME elastogram for the real plaque, showing a substantial contrast improvement; b) and c) vertical and horizontal 1D

plots from the elastogram showing more effective contrast ratio between dense and cellular fibroses, after strain decay compensation.

DETAILED DESCRIPTION OF A PREFERRED EMBODIMENT OF THE INVENTION

The forward problem in EVE is addressed; it is followed by the derivation of the tissue motion estimator, and by the biomechanical simulations of the vessel walls. Results are presented in the following section, followed by the discussion of the results and the conclusions and perspectives to this work.

METHODOLOGY

Endovascular elastography (EVE) is a catheter-based modality, which gives insights about mechanical properties of the vessel wall. Following the example of IVUS, the transducer is placed at the tip of the catheter and cross-sectional imaging of a vessel is generated by sequentially sweeping the ultrasound beam in a 360° angle. Mechanical parameters (radial strain, in this case) are estimated from analyzing the kinematics of the vascular tissue during the normal cardiac cycle (or, in some instances, in response to an angioplasty-balloon push). Figure 6 presents a schematic illustration of such a process.

The forward problem in EVE

The polar static-image-formation model

The image-formation model, presented here, is for a rotating beam (single element or an array transducer system) and is thus expressed in polar coordinates. It is based on previous works by Bamber and Dickinson (1980). Such a model was used by Meunier and Bertrand (1995) to study speckle dynamics; it was also considered to investigate speckle motion artifacts (Kallel and Bertrand, 1994; Maurice and Bertrand, 1999b). Under assumptions such as space-invariance of

the imaging system, and plane strain conditions for the motion (that is no transverse motion is involved), the following simple 2D model was used (Maurice and Bertrand, 1999b):

$$I(x,y) = h(x,y) \otimes z(x,y), \quad (1)$$

where $I(x,y)$ is the RF image, $h(x,y)$ is the point-spread function (PSF) of the ultrasound system, \otimes is the 2D convolution operator, and $z(x,y)$ is the acoustic impedance function, which can be modeled as a white Gaussian noise (random distribution of uncorrelated scatterers within the region of interest). As it will be seen further in this section, the notation " " is only for convenience and it does not refer to any mathematical operator.

Because the speckle dimension varies with depth for polar scan systems such as the one described in Fig. 6, Eq. 1 is valid only for small regions of interest (ROI). Accordingly, the linear image-formation model is formulated using the superposition integral, given by:

$$I(r,\phi) = \iint h(r,\phi,r',\phi') z(r',\phi') r' dr' d\phi', \quad (2)$$

where r and ϕ are the radial (depth) and angular coordinates, respectively; $I(r,\phi)$, $h(r,\phi)$, and $z(r,\phi)$ are the polar RF image, polar PSF, and the acoustic impedance function mapped in polar coordinates, respectively. Furthermore, for a polar scan system, $h(r,\phi)$ can be considered angular-position invariant; therefore, Eq. 2 becomes:

$$I(r,\phi) = \iint h(r,r',\phi-\phi') z(r',\phi') r' dr' d\phi'. \quad (3)$$

It is convenient to model the PSF as a cosine modulated by a 2D Gaussian envelope; that is a simple approximation of the far field PSF. The mathematical formulation can be expressed as:

$$h(r, r', \varphi - \varphi') = e^{-\left(\frac{(r-r')^2}{2\sigma_r^2} + \frac{(\varphi-\varphi')^2}{2\sigma_\varphi^2}\right)} \cos\left(2\pi \frac{f_{tr}}{c/2} (r-r')\right), \quad (4)$$

where σ_r is a pulse length parameter; $\sigma_\varphi \equiv \sigma_\varphi(r)$ is a beam-width parameter (the dependence in "r" is because of the radial-position variance of the PSF); f_{tr} and c are the transducer frequency and the sound velocity in soft tissue, respectively.

10 For simplicity, it is assumed that $\sigma_\varphi(r)$ is a linear function of r ; it is expressed as:

$$\sigma_\varphi(r) = \frac{r}{R_L} \sigma_0, \quad r \geq R_L \quad (5)$$

with R_L being the lumen radius and σ_0 the beam width at $r = R_L$. In such a situation, the beam forms a divergent cone with a section that linearly increases with depth through the vessel wall. It is important to notice that Eqs 4 and 5 define a very simple approximation of the PSF in the far-field. In practice, the near field beam profile is more complex. However, it can be assumed that the transducer is positioned near the middle of the lumen, so that the vessel wall is not in the near field¹⁾. Additionally to the divergence of the ultrasound beam profile, the curvature of the wave-fronts also raises the complexity of the polar scan model; this will be argued in the discussion.

20 In theory, $\sigma_\varphi(r)$ is a continuous function of r . However, for simplification it will be considered as a piecewise constant function, the n partitioning regions being

¹⁾ Whereas the lumen is in practice in the near field, it is here simulated as being in the far field (with a beam width $\sigma_\varphi(r) = \sigma_0$). This simplifying hypothesis does not alter the generality of the model, since tissue motion assessment is not relevant for the lumen.

defined by the boundaries $0 = r_0 < r_1 < r_2 < \dots < r_n$. For convenience, each partition will be denoted as P_k , that is:

$$P_k =]r_{k-1}, r_k], \quad k = 0, \dots, n \quad (6)$$

A discrete approximation of $\sigma_\varphi(r)$ is then defined as follows:

$$\sigma_\varphi(r)|_{r \in P_k} \cong \sigma_\varphi(P_k) = \frac{\overline{P_k}}{R_L} \sigma_0 \quad (7)$$

- 10 where $\overline{P_k}$ is the mean radial distance of the interval P_k . Now, assuming that the PSF is locally depth-invariant, i.e. on each P_k , the linear model of Eq. 3 can be approximated by the following convolution form:

$$I(r, \varphi) \cong \sum_k^n I(P_k, \varphi) = \sum_k^n [h(P_k, \varphi) \otimes z(P_k, \varphi)] \quad (8)$$

with:

$$h(P_k, \varphi) = h(r, \varphi)|_{r \in P_k} = e^{-\left(\frac{r^2}{2\sigma_r^2} + \frac{\varphi^2}{2\sigma_\varphi(r)^2}\right)} \cos\left(2\pi \frac{f_{tr}}{c/2} r\right).$$

- 20 While the continuity of $I(r, \varphi)$ at the boundaries of the partitions can be questioned, Eq. 8 presents a simple approximation model of a polar scan system. Figure 7 illustrates the implementation of such a model for a 20 MHz transducer with a 60% bandwidth at -3 dB and a beam width (width at half maximum = $2.35 \times \sigma_0$) of 0.1 mm. It is important to remember that $z(r, \varphi)$ is the acoustic impedance function mapped in polar coordinates. $z(r, \varphi)$ is assumed to be a continuum, which can be modeled as a normal statistical process. For the purpose of simulations presented

below, $z(r, \phi)$ was obtained simply by generating a 2D normally distributed random field. The lumen and the tissue surrounding the vessel were assumed to be respectively 2.5 and 1.67 times less echoic than the wall.

Figure 7a shows the beam profile as a function of depth. The beam width increases linearly, being minimal in the lumen and maximal in the surrounding tissue; the partition number n was set at 5. Figure 7b presents a simulated polar B-mode image for an homogenous vessel section, whereas Figure 7c gives the equivalent IVUS image (in Cartesian coordinates).

10 The tissue-motion model

For a small ROI, tissue motion can be approximated by an affine transformation; this can be expressed in Cartesian coordinates as:

$$\begin{bmatrix} p(x, y, t) \\ q(x, y, t) \end{bmatrix} = \underbrace{\begin{bmatrix} \theta_1 \\ \theta_4 \end{bmatrix}}_{Tr} + \underbrace{\begin{bmatrix} \theta_2 & \theta_3 \\ \theta_5 & \theta_6 \end{bmatrix}}_{LT} \begin{bmatrix} x \\ y \end{bmatrix} \quad (9)$$

where θ_i is a function of time t ($\theta_i(t)$). Equation 9 is the result of a translation (vector $[Tr]$) and of a linear geometrical transformation of coordinates (matrix $[LT]$); it can also be seen as trajectories that describe a tissue motion in a region of constant strain (Maurice and Bertrand, 1999a). Strain is usually defined in terms of the gradient of a displacement field; since $p(x, y, t)$ and $q(x, y, t)$ represent the new position of a point (x, y) , the (u_x, u_y) components of the displacement vector in the (x, y) coordinate system are given by:

$$\begin{bmatrix} u_x \\ u_y \end{bmatrix} = \begin{bmatrix} p(x, y, t) - x \\ q(x, y, t) - y \end{bmatrix} = \begin{bmatrix} \theta_1 \\ \theta_4 \end{bmatrix} + \Delta \begin{bmatrix} x \\ y \end{bmatrix} \quad (10)$$

with: $\Delta = \begin{bmatrix} \theta_2 - 1 & \theta_3 \\ \theta_5 & \theta_6 - 1 \end{bmatrix}$

In the above equation, Δ can be defined as the Cartesian deformation matrix. The ε_{ij} , which are the components of the strain tensor ε , are expressed in terms of the Δ_{ij} components as:

$$\varepsilon_{ij}(t) = \frac{1}{2}[\Delta_{ij}(t) + \Delta_{ji}(t)]. \quad (11)$$

Furthermore, the radial and tangential components of the displacement vector (u_r , u_φ) in the (r, φ) coordinate system are, respectively, given as:

$$u_r = \sqrt{u_x^2 + u_y^2} \quad (12)$$

$$u_\varphi = \arctan\left(\frac{u_y}{u_x}\right), \quad \text{with } u_x \equiv u_x(x(r, \varphi), y(r, \varphi)) \quad \text{and} \quad u_y \equiv u_y(x(r, \varphi), y(r, \varphi))$$

The polar deformation matrix, labeled as $\xi(t)$, then can be derived from Eqs 12 and 10; it is given as:

$$\xi(t) = \begin{bmatrix} \frac{\partial u_\varphi}{\partial \varphi} & \frac{\partial u_\varphi}{\partial r} \\ \frac{\partial u_r}{\partial \varphi} & \frac{\partial u_r}{\partial r} \end{bmatrix} = \begin{bmatrix} \frac{\partial u_\varphi}{\partial u_x} & \frac{\partial u_\varphi}{\partial u_y} \\ \frac{\partial u_r}{\partial u_x} & \frac{\partial u_r}{\partial u_y} \end{bmatrix} \begin{bmatrix} \frac{\partial u_x}{\partial x} & \frac{\partial u_x}{\partial y} \\ \frac{\partial u_y}{\partial x} & \frac{\partial u_y}{\partial y} \end{bmatrix} \begin{bmatrix} \frac{dx}{d\varphi} & \frac{dx}{dr} \\ \frac{dy}{d\varphi} & \frac{dy}{dr} \end{bmatrix} \quad (13)$$

$$= \begin{bmatrix} \frac{\partial u_\varphi}{\partial u_x} & \frac{\partial u_\varphi}{\partial u_y} \\ \frac{\partial u_r}{\partial u_x} & \frac{\partial u_r}{\partial u_y} \end{bmatrix} \Delta \begin{bmatrix} \frac{dx}{d\varphi} & \frac{dx}{dr} \\ \frac{dy}{d\varphi} & \frac{dy}{dr} \end{bmatrix} \quad \text{with: } \begin{cases} x = r \cos \varphi \\ y = r \sin \varphi \end{cases}$$

The map of the ξ_{rr} ($= \varepsilon_{rr}$) component is known in EVE as the radial elastogram; ξ_{rr} can be expressed as a function of the Cartesian deformation matrix (Δ) as:

$$\xi_{rr}(t) = \frac{\partial u_r}{\partial r} = \left[\frac{\partial u_r}{\partial u_x} \quad \frac{\partial u_r}{\partial u_y} \right] \Delta \begin{bmatrix} \cos \varphi \\ \sin \varphi \end{bmatrix} \quad (14)$$

For a small pressure from within the vessel lumen, ξ_{rr} is expected to provide a cartography of relative tissue stiffness inside the vessel wall.

The polar dynamic-image-formation model

The 2D polar dynamic-image-formation model for an in-plane tissue motion is now derived. It is worth to remember that $z(r, \varphi)$ is a map of the acoustic impedance function $z'(x, y)$ in polar coordinates. That can mathematically be expressed as:

$$z(r, \varphi) = z'(x, y) \Big|_{\substack{x=r \cos \varphi \\ y=r \sin \varphi}} \quad (15)$$

The affine transformation on $z'(x, y)$ can be set by only changing the (x, y) coordinates. Without lost of generality, it is assumed that translation is absent or is appropriately compensated for, and $[T_r]$ in Eq. 9 can thus be neglected. The compensation for translation can be done using correlation techniques; such a processing is known, in the literature, as companding (Chaturvedi et al., 1998a and 1998b). It is also interesting to notice that impressing $[LT]$ on the tissue to simulate motion requires to compute the inverse transformation $[LT^{-1}]$ on the coordinates. Hence, for an (r, φ) in-plane motion, the 2D RF polar dynamic-image-formation model at time t becomes:

$$I(r, \varphi, t) \cong \sum_k^n I(P_k, \varphi, t) = \sum_k^n \left[h(P_k, \varphi) \otimes z_{LT_p^{-1}}(P_k, \varphi) \right] \quad (16)$$

with $z_{LT_p^{-1}}(P_k, \varphi) = z_{LT_p^{-1}}(r, \varphi) \Big|_{r \in P_k} = z'_{LT^{-1}}(x, y) \Big|_{\substack{x=r \cos \varphi \\ y=r \sin \varphi}}$

In Eq. 16, $z'_{LT^{-1}}(x,y)$ indicates a change in coordinates for the function $z'(x,y)$; that change involves the 2×2 matrix $[LT^{-1}]$. Similarly, $z_{LT_p^{-1}}(P_k, \phi)$ indicates a change in coordinates for the function $z(P_k, \phi)$ where the 2×2 matrix $[LT_p^{-1}]$ is involved. Implicitly, this means that $[LT]$ (as well as $[LT_p]$) is invertible. This assumption is valid for incompressible continuum.

Tissue motion estimation

Lagrangian speckle image (LSI)

Vascular tissue is subjected to complex movement. For instance, it may rotate, shear, stretch, or compress in the measurement plane. As a result of such kinematics, the relative positions of the speckle change; this sets a fundamental limitation to correlation-based tissue motion estimators. However, it was demonstrated that the effects of such position changes can be compensated for in the process of motion assessment by pre-processing the signals using temporal stretching (Ophir et al., 1999) or companding (Chaturvedi et al., 1998a and 1998b). Interestingly, the Lagrangian speckle image (LSI) was introduced to describe the ultrasound signals compensated for tissue motion (Maurice and Bertrand, 1999a). For example, in the dynamic image-formation model of Eq. 16, tissue motion is induced by applying the linear transformation matrix $[LT_p^{-1}]$ to $z(r, \phi)$; hence, the motion-compensated image, said the LSI, is obtained through applying $[LT_p]$ (the inverse of $[LT_p^{-1}]$) to a post-motion RF image at time t given by $I(r, \phi, t)$. For the polar dynamic image-formation model given by Eq. 16, the LSI (noted as I_{Lag}) is then expressed as:

$$\begin{aligned}
 I_{\text{Lag}}(r, \varphi, t) &= [I(r, \varphi, t)]_{LT_p} \equiv \left[\sum_k^n h(P_k, \varphi) \otimes z_{LT_p^{-1}}(P_k, \varphi) \right]_{LT_p} \\
 &= \sum_k^n [h_{LT_p}(P_k, \varphi) \otimes z(P_k, \varphi)]_{LT_p}
 \end{aligned} \tag{17}$$

In the above equation, $|LT_p|$ is the determinant of the matrix $[LT_p]$.

The Lagrangian speckle model and the minimization problem

As described in Maurice and Bertrand (1999a), the motion compensated RF image is labeled as the Lagrangian Speckle image, because the correction for tissue displacement directly involves the Lagrangian description of motion. For instance, it is expressed in Eq. 17 that the LSI brings back material points to the positions where they originally stood. Accordingly, a convenient model to formulate the LSI can be given as:

$$I(r, \varphi, 0) = I_{\text{Lag}}(r, \varphi, t) + \mathfrak{R}(r, \varphi, t) = [I(r, \varphi, t)]_{LT_p} + \mathfrak{R}(r, \varphi, t), \tag{18}$$

where $\mathfrak{R}(r, \varphi, t)$ can be seen as an error term. The mathematical model for a tissue motion estimator then can be formulated as:

$$\begin{aligned}
 \min_{LT_p} \|I(r, \varphi, 0) - [I(r, \varphi, t)]_{LT_p}\|^2 &= \min_{LT_p} \|I(r, \varphi, 0) - I_{\text{Lag}}(r, \varphi, t)\|^2 \\
 &= \min_{LT_p} \|\mathfrak{R}(r, \varphi, t)\|^2
 \end{aligned} \tag{19}$$

The minimum is obtained using the appropriate $[LT_p]$. It is worth to remember that $[LT_p]$ is a linear transformation matrix; it maps the Cartesian trajectories (Eq. 9) in a polar coordinate system. However, for a small ROI ($\Delta r, \Delta \varphi$) that is far from the lumen center, motion equivalently can be investigated using either polar or

coordinate system. In other words, the following approximation can be done to compute the elastogram:

$$\xi \equiv LT - I \quad (20)$$

where I is the 2D-identity matrix.

The Levenberg-Marquardt nonlinear minimization

Several gradient-based methods exist to numerically solve minimization problems as given by Eq. 19. For instance, the Gauss-Newton proceeds iteratively towards the minimum using a linear approximation of $\Re(r, \phi, t)$. Because $I_{Lag}(r, \phi, t)$ and $\Re(r, \phi, t)$ are implicit functions of θ_i (Eq. 9), and without loss of generality, let's rewrite $I_{Lag}(r, \phi, t)$ as $I_{Lag}(\bar{\theta})$ and $\Re(r, \phi, t)$ as $\Re(\bar{\theta})$, respectively; $\bar{\theta}$ is the vectorization of $[LT_p]$. At the k^{th} iteration, one will have:

$$\Re(\bar{\theta}^k) = \Re(\bar{\theta}^{k-1} + \Delta\bar{\theta}^k) = I_0 - I_{Lag}(\bar{\theta}^{k-1}) - \sum_i^n \frac{\partial I_{Lag}}{\partial \theta_i} \Delta\theta_i^k \Big|_{\bar{\theta}^{k-1}} \quad (21)$$

with $I_0 = I(r, \phi, 0)$

In Eq. 21, $\bar{\theta}^{k-1}$ is computed at iteration $k-1$, $\Delta\theta_i^k$ is the increment of the i^{th} component of $\bar{\theta}$, $I_{Lag}(\bar{\theta}^{k-1})$ is the Lagrangian image at iteration $k-1$, and $\frac{\partial I_{Lag}}{\partial \theta_i}$ are partial derivative of I_{Lag} with respect to each component of $\bar{\theta}$. A more compact formulation of Eq. 21 is given as:

$$\bar{I}_0 - \bar{I}_{\text{Lag}}(\bar{\theta}^{k-1}) = [J_{k-1}] \bar{\Delta\theta}^k + \bar{\mathcal{R}}$$

$$\text{with } J_{k-1} = \begin{bmatrix} \frac{\partial \bar{I}_{\text{Lag}}}{\partial \theta_1} & \frac{\partial \bar{I}_{\text{Lag}}}{\partial \theta_2} & \dots & \frac{\partial \bar{I}_{\text{Lag}}}{\partial \theta_n} \\ \vdots & \vdots & & \vdots \\ \frac{\partial \bar{I}_{\text{Lag}}}{\partial \theta_1} & \frac{\partial \bar{I}_{\text{Lag}}}{\partial \theta_2} & \dots & \frac{\partial \bar{I}_{\text{Lag}}}{\partial \theta_n} \end{bmatrix}, \quad (22)$$

where \bar{I}_0 , $\bar{I}_{\text{Lag}}(\bar{\theta}^{k-1})$, and $\bar{\mathcal{R}}$ are vectorizations of I_0 , I_{Lag} , and \mathcal{R} , respectively; $[J_{k-1}]$ is the Jacobian matrix; and $\bar{\Delta\theta}^k$ is a vector of increments used to update the Lagrangian images ($\bar{\Delta\theta}^k$ is also known in the literature as the step size). For such a model, the least-square error solution is given as:

$$\Delta\theta^k = [J_{k-1}^T J_{k-1}]^{-1} J_{k-1}^T (\bar{I}_0 - \bar{I}_{\text{Lag}}(\bar{\theta}^{k-1})), \quad (23)$$

- 10 where the subscript T designates the transpose operator. When $J_{k-1}^T J_{k-1}$ is not invertible, a regularized version of Eq. 23 may be required to ensure the convergence of the solution. The Levenberg-Marquardt method (L&M) converges to a potential solution for such a problem (Levenberg, 1963; Marquardt, 1944). The L&M regularized inversion was implemented as:

$$\bar{\Delta\theta}^k = [J_{k-1}^T J_{k-1} + \lambda_k I]^{-1} J_{k-1}^T (\bar{I}_0 - \bar{I}_{\text{Lag}}(\bar{\theta}^{k-1})), \quad (24)$$

- 20 where λ_k is a non-negative scalar, and I is the identity matrix. It is interesting to know that the L&M algorithm was chosen for its robustness; it combines the best features of the gradient and of the Gauss-Newton methods. Indeed, as $\lambda_k \rightarrow 0$,

$\overline{\Delta\theta}^k$ is given by the Gauss-Newton method, that allows fast convergence in the vicinity of the solution; and as $\lambda_k \rightarrow \infty$, $\overline{\Delta\theta}^k$ becomes parallel to the steepest-descent direction, that allows to converge even when the initial guess is outside the region of convergence for other methods. In the current study, the identity matrix was used as the initial guess.

The optical flow equations and the Jacobian matrix

The optical flow equations, or material derivatives, give a relationship between measures in Eulerian and Lagrangian coordinate systems, respectively (Horn, 1986). For instance, $I_{\text{Lag}}(\bar{\theta}^{k-1})$ can be seen as a function that describes a material property. Assuming that such a material property is preserved with motion, the total derivative of $I_{\text{Lag}}(\bar{\theta}^{k-1})$ can be expressed as:

$$\begin{aligned} \frac{dI_{\text{Lag}}(\bar{\theta}^{k-1})}{d\theta_i} &= \frac{\partial I_{\text{Lag}}(\bar{\theta}^{k-1})}{\partial r} \frac{dr}{d\theta_i} + \frac{\partial I_{\text{Lag}}(\bar{\theta}^{k-1})}{\partial \phi} \frac{d\phi}{d\theta_i} + \frac{\partial I_{\text{Lag}}(\bar{\theta}^{k-1})}{\partial \theta_i} = 0 \\ \therefore \frac{\partial I_{\text{Lag}}(\bar{\theta}^{k-1})}{\partial \theta_i} &= - \frac{\partial I_{\text{Lag}}(\bar{\theta}^{k-1})}{\partial r} \frac{dr}{d\theta_i} - \frac{\partial I_{\text{Lag}}(\bar{\theta}^{k-1})}{\partial \phi} \frac{d\phi}{d\theta_i} \\ \text{with } \frac{\partial I_{\text{Lag}}(\bar{\theta}^{k-1})}{\partial \bar{\theta}} &= I_{\text{Lag}}(\bar{\theta}^{k-1} + \overline{\Delta\theta}^k) - I_{\text{Lag}}(\bar{\theta}^{k-1}). \end{aligned} \tag{25}$$

As discussed above, under the assumption of a small ROI (Δr , $\Delta \phi$) that is far from the lumen center, tissue motion equivalently can be investigated using either the Cartesian or polar coordinates. Additionally, for small motion, the gradient of $I_{\text{Lag}}(\bar{\theta}^{k-1})$ should not be significantly different from the gradient $I(r, \phi, 0)$. These hypotheses, in conjunction with Eq. 9, lead to:

$$\frac{\partial I_{\text{Lag}}(\bar{\theta}^{k-1})}{\partial \bar{\theta}} = \frac{\partial I(\bar{\theta}^{k-1})}{\partial \bar{\theta}} = - \left\{ \frac{\partial I}{\partial x}, \frac{\partial I}{\partial x} x, \frac{\partial I}{\partial x} y, \frac{\partial I}{\partial y}, \frac{\partial I}{\partial y} x, \frac{\partial I}{\partial y} y \right\}. \quad (26)$$

Eq. 26 gives the full expression for the 6 components of the Jacobian matrix $[J_{k-1}]$ (Eq. 22). This is an interesting result, since using the optical flow equations to compute the gradient appears more robust than the conventional finite difference method. It is thus expected that such a combination of the optical flow equations with the L&M minimization algorithm may lead to more accurate tissue motion estimates. This last approach was used in the current study.

Biomechanical simulations of vessel wall kinematics

10 Model design and image analysis

The computational structural analysis was performed on one idealized coronary plaque (Figure 8), and on one typical composite plaque identified from an in vivo IVUS image (Figure 9a). For the idealized case, the lumen cross-sectional area (LA) was 3,08 mm², the external elastic membrane cross-sectional area (EEMA) was 12,32 mm², the plaque + media cross-sectional area (P+MA=EEMA-LA) was 9,24 mm², and the plaque burden (PB%=100*(P+MA)/EEMA) was 75 % (Mintz et al., 2001). Equivalently, for the real case, the LA was 3,78 mm², the EEMA was 34,29 mm², and the PB% was 89 %.

- 20 The major difficulty in computational structural analysis based on in vivo imaging is to determine the unloaded physiological configuration of the artery; i.e., the configuration when the artery is subjected to no external load. This configuration has to be known for finite element (FE) simulations. To obtain this unloaded state, adenosine triphosphate (ATP) (Striadyne®, Wyeth France Laboratories) was injected to the patient, as previously described by Ohayon et al. (2001). All contours in the IVUS image were manually traced (Figure 9b). These contours are those of the lumen border, media, adventicia, and plaque components (dense

fibrosis, mixed fibrosis, and cellular fibrosis). The adventicia contour was added in the simulation and it had a mean thickness of 350 μm (Rioufol et al., 1999), so as to take account of its protective role against any radial overstretching of the artery (Rachev, 1997). The various contours were digitized using the Un-Scan-It® software (Silk Scientific, Inc., Orem, UT).

Material properties

For the two models, the materials were considered as quasi-incompressible (Poisson ratios $\nu=0.49$) and isotropic with linear elastic properties. The Young's modulus for the healthy vascular tissue (or adventitia & media) was 80 kPa (Williamson et al., 2003), while the dense fibrosis (much stiffer) was set at 240 kPa, and the cellular fibrosis (softer than the dense fibrosis) was chosen at 24 kPa (Ohayon et al., 2001; Treyve et al., 2003). As to emulate boundary conditions provided by the surrounding environment, these two vessel sections were assumed to be imbedded in a 1000 kPa Young's modulus tissue.

Structural analysis

FE computations were performed using the ANSYS 5.7® software (Ansys, Inc., Cannonsburg, PA). Static simulations of coronary plaque under loading blood pressure were performed on the geometrical models previously described (Figs 8 and 9b). Nodal displacements were set to zero on the external boundaries of the surrounding tissue.

The various regions of the plaque components were then automatically meshed with triangular (6 nodes) and quadrangular (8 nodes) elements. The FE models were solved under the assumption of plane and of finite strains. The assumption of plane strain was made because axial stenosis dimensions were of at least the same order of magnitude as the radial dimensions of the vessel. Moreover, the assumption of finite deformation was required as the strain maps showed values of 30% for physiological pressures (Loree et al., 1992; Cheng et al., 1993; Lee et al., 1993; Ohayon et al., 2001; Williamson et al., 2003). The Newton-Raphson

iterative method with a residual nodal tolerance of 4×10^{-4} N was used to solve the FE models. The calculations were performed with a number of elements close to 7200.

This computational structural FE analysis was used to perform the kinematics of the vascular tissue. The dynamic image-formation model (Eq. 16) was implemented using the Matlab software (The MathWorks Inc, MA, USA, ver. 6.0). The process to simulate polar radio-frequency (RF) images is schematically presented in Figure 10, for a homogeneous (pathology-free) vessel wall; it can be summarized as follows. It started by generating in Matlab a scattering function that simulated the acoustical characteristics of a transverse vascular section in Cartesian coordinates; that provided $z'(x,y)$. The axial and lateral displacement fields were computed with Ansys and were applied upon $z'(x,y)$ to perform motion and then to provide $z'_{LT^{-1}}(x,y)$.

The next step consisted in mapping $z'(x,y)$ and $z'_{LT^{-1}}(x,y)$ in a polar coordinate system (r,ϕ) to provide $z(r,\phi)$ and $z_{LT^{-1}}(r,\phi)$ (Eqs 15 and 16). Both polar-mapped acoustic impedance functions were then convolved with the polar PSF to provide polar pre- and post-tissue-motion RF images $I(r,\phi,0)$ and $I(r,\phi,t)$, given by Eq. 16). Those images were used as inputs to the LSME (Eq. 19).

In summary, the static and the dynamic image-formation models associated with a polar scan were derived in section II.A, whereas the LSME was adapted for EVE in II.B. In the Results section below, this new approach is validated using the biomechanical simulations of the vessel wall kinematics (for the "ideal" and the "realistic" plaque geometries) presented in section II.C.

Results

The idealized vessel measured about 3.8 mm in outer diameter, whereas the RF images extended to 4 mm × 4 mm. The real case vessel measured about 7 mm in outer diameter, whereas the RF images extended to 8 mm × 8 mm. For the purpose of simulations, the intraluminal pressure gradient for both vessel-wall geometries described above was set such as the dilation at the inner wall was around 7 %. The PSF characterized a 20 MHz central frequency transducer, as described in the forward problem (section II.A). The LSME (described in section II.B) was implemented to assess tissue motion; measurement-windows of 0.38 mm × 0.40 mm and 0.77 mm × 0.80 mm, with 90 % axial and lateral overlaps, were used for the idealized and the realistic cases, respectively. For more details concerning the definition of the measurement-window required with the LSME, the reader is referred to Fig. 1 of Maurice et al. (2003).

Investigation of the "ideal" plaque pathology

Figure 11a presents the theoretical radial strain elastogram, computed for the "ideal" pathology case. The plaque can slightly be differentiated from the normal vascular tissue, whereas a region of higher strain values is observed at the right portion of the inner vessel wall. Those "mechanical artifacts" are a direct consequence of the well known strain decay phenomenon²⁾ (Shapo et al., 1996a). For a more quantitative illustration, are presented in Figure 11b plots from the theoretical elastogram for two orthogonal orientations along x and y. Indeed, the vertical plot (—) shows low contrast between the plaque and the normal vascular tissue, whereas the horizontal plot (---) clearly points out the presence of strain decay.

Figure 11c presents the radial strain elastogram as computed with the LSME, using simulated RF images. As for the theoretical elastogram in Figure 11a, the plaque is slightly distinguishable from the normal vascular tissue and a region of higher strain values is also observed. The plots of Figure 11d confirm such

²⁾ Radial strain ϵ_r is proportional to $1/r^2$. This decreasing of ϵ_r with depth is usually defined as strain decay.

observations. Notice that lower strain values were computed in the LSME elastogram than in theory, specifically at the inner wall; that is due to the windowing process required to assess tissue motion with the LSME.

For the purpose of compensating for strain decay, the LSME radial strain elastogram was post-processed. Indeed, ϵ_{rr} was modulated with a function proportional to the square of the vessel radius³⁾. In Figure 12a is presented the strain-decay-compensated LSME elastogram, showing substantial contrast improvement. For instance, the axial plot of Figure 12b shows an effective contrast ratio close to 3 between the plaque and the normal vascular tissue, as it can be expected; equivalently, Figure 12c also shows some valuable contrast ratio improvement.

Investigation of a "realistic" vessel wall pathology

Figure 13a presents the theoretical radial strain elastogram, computed for the "realistic" pathology case. Interestingly, complex strain patterns are observed; nevertheless, different regions can be identified. For instance, since the ratio of Young's moduli between the dense and the cellular fibroses was arbitrarily set to 10, both of those materials can be distinguished. Less contrast is seen between the cellular fibrosis and the healthy vascular tissue because their Young's modulus contrast was set to 3. As illustrated with vertical and horizontal 1D plots from the elastogram (Figs 13b and 13c, respectively), strong strain decay is observed specifically at the inner portion of the vessel wall.

Figure 14a presents the radial strain elastogram as computed with the LSME, using simulated RF images. As for the theoretical elastogram in Figure 13a, very complex strain patterns are observed. Moreover, the dense and the cellular fibrosis tissues can be identified. However, while less prominent than in the "ideal"

³⁾ Since radial strain ϵ_{rr} decreases proportionally to $1/r^2$, the compensation for strain decay consists in multiplying ϵ_{rr} by a function proportional to r^2 (Shapo *et al.*, 1996a). However, for non symmetric vessel

case study, strain decay remains a significant factor to compensate for to improve image interpretation. This is illustrated in Figs 14b and 22c, where vertical and horizontal 1D plots from the elastogram are presented. Whereas low strain values clearly indicate the presence of stiff materials in Figure 14b, this is not the case in Figure 14c.

10 In Figure 15a is presented the strain-decay-compensated LSME elastogram, showing substantial contrast improvement. Now, the vertical plot (Figure 15b) as well as the horizontal one (Figure 15c) show more effective contrast ratio between dense and cellular fibroses, and between cellular fibrosis and the normal vascular tissue. Moreover, it is interesting to notice the presence of moderate strain values (around 0.6 to 0.8 %) at the extremities of the plots; this characterizes regions of healthy vascular tissue, namely the media and adventicia.

Discussion

20 Pathological conditions of vascular tissues often induce changes in the vessel wall elasticity. For instance, plaque deposit stiffens the vascular wall and then counteracts its dilation under systolic blood pressure. Hence, investigating mechanical and elastic properties of the arteries seem suitable to appreciate the dynamics of the arterial wall and its pathologies. In this paper, a model-based approach devoted to outline the elastic properties of the vessel wall with endovascular elastography (EVE) was presented. Results obtained from numerical simulations establish the potential of such a method to reliably assess very complex strain patterns.

About the forward problem

Regarding the forward problem (FP) in EVE, a polar static image-formation model was introduced. Taking into account the spatial variation with depth associated to polar scan systems, this image-formation model was formulated using the

geometries, as it is the case in this study, this process may require to segment the vessel lumen as to provide the vessel geometric center.

superposition integral. The radial variation was conveyed with the beam width, that increases as a linear function of depth. This is actually a relatively simplistic approximation. In practice, the transducer point-spread function (PSF) is expected to be more complex. Indeed, the PSF geometry could be more curved than linear (Kallel and Bertrand, 1994; Maurice and Bertrand, 1999b); such a curvature may appear very important for tissue motion estimation, since it was demonstrated that it would induce speckle motion artifacts (Kallel and Bertrand, 1994; Maurice and Bertrand, 1999b). It would be worth, in the future, to address the polar dynamic image-formation model with a more complex ("realistic") PSF geometry.

10 About the tissue motion estimation

To assess tissue motion, the Lagrangian speckle model estimator (LSME) was used. The LSME is a 2D model-based estimator that allows computing the full 2D-strain tensor. In this paper, it was adapted for EVE investigations. While the full 2D polar strain tensors were computed, only the radial strain parameters were mapped to provide the elastograms. This was motivated by the fact that tissue motion, in EVE, is expected to run parallel with the ultrasound beam. However, in real-life situations, this is not always the case. Inherent motions of the vessel wall that are due to the pulsatile blood flow, for instance, may misalign the ultrasound beam and the tissue motion. While a 2D model partially compensates for such a decorrelation, the adapted Levenberg-Maquardt algorithm presented here also
20 should help in circumventing this drawback. Indeed, the Jacobian matrix, as implemented with the optical flow equations (Eq. 26), provides a more robust gradient estimation method than the finite-difference method generally used.

As discussed above, the pre- and post-motion RF images are, in practice, subjected to motion artifacts due to the complexity of the beam geometry for polar scan systems. Accordingly an estimator, that allows counteracting such motion artifacts, could be required. For instance, the application of the Lagrangian filter, as described in Maurice and Bertrand (1999a and 1997), could be a potential
30 solution. Indeed, the Lagrangian filter was proposed to take into account the PSF

term in the motion estimation process; it thus potentially allows to compensate for artifacts introduced by instrumentation. We look forward for the implementation of the filtered-version of the LSME for future clinical applications.

Conclusion

10 A new approach devoted to endovascular elastography (EVE) was presented. As a first step, a polar static image-formation model was described; it took into account the spatial variation of the PSF with depth associated to polar scan systems. The Lagrangian speckle model estimator (LSME) was then adapted for EVE investigations. Indeed, the LSME was formulated as a nonlinear minimization problem, for which an analytical formulation of the Jacobian matrix was derived. The hypothesis behind this model-based approach was that speckle is a material property. While the full 2D polar strain tensor was assessed, only the radial strain parameter was mapped to provide the elastogram. This was motivated by the fact that, in EVE, tissue motion is expected to run parallel with the ultrasound beam. To validate the method, biomechanical simulations of the vessel wall kinematics were conducted. The results allow believing in the potential of this model-based approach to reliably assess very complex strain patterns; interestingly, it provides mechanical property insights that are occlusive to IVUS B-scans.

FIELD OF THE INVENTION

This invention relates generally to the field of endovascular ultrasound elastography (EVE) and more particularly, but not exclusively, to an apparatus and a method to detect hard plaques in the blood vessels.

BACKGROUND OF THE INVENTION

10 Atherosclerosis, disease of the intima layer of arteries, remains a major cause of mortality in western countries. This pathology is characterized by a focal accumulation of lipids, complex carbohydrates, blood cells, fibrous tissues and calcified deposits, forming a plaque that thickens and hardens the arterial wall. A severe complication of atherosclerosis is thrombosis, consequently to plaque rupture or fissure, that might lead, according to the event localization, to unstable angina, brain or myocardial infarction, and sudden ischemic death. Plaque rupture is a complicated mechanical process, correlated with plaque morphology, composition, mechanical properties and with the blood pressure and its long term repetitive cycle. Extracting information on the plaque local mechanical properties and on the surrounding tissues may thus reveal relevant features about plaque vulnerability. Unfortunately no imaging modality, currently in clinical use, allows the
20 access to these properties.

So far, diagnosis and prognostic of atherosclerosis evolution mainly rest on plaque morphology and vessel stenose degree. These information can be accurately accessed with IntraVascular UltraSound (IVUS) imaging, since this modality provides high resolution cross-sectional images of arteries. Accurate quantitative analysis of the disease is thus easily performed by precise measurements of the lumen area, arterial dimensions and dimensions specific to the plaque. Moreover, IVUS permits a characterization of plaque components, but roughly, in terms of fatty, fibrous or calcified plaques and with possible misinterpretations. This makes
30 IVUS, alone, insufficient to predict the plaque mechanical behavior. However,

elastic properties of vessel walls can be derived from radio-frequency (RF) IVUS images, by integrating elastographic processing methods. Indeed, endovascular ultrasound elastography (EVE) is an in-development imaging technique which aims to outline elastic properties of vessel walls. Its principle consists of acquiring sequences of cross-sectional vessel ultrasound images, while the vascular tissue is compressed by applying a force from within the lumen; strain distribution is then estimated by tracking, within the signals, the modifications induced by the stress application. In practice, in EVE, such a stress can be induced by the normal cardiac pulsation or by using a compliant intravascular angioplasty balloon.

10

As primary investigations on EVE feasibility, phantom studies were conducted. In general, tissue-mimicking phantoms with typical morphology and hardness topology synthesizing atherosclerotic vessels were constructed. Namely, de Korte et al. have demonstrated the potential of EVE to identify different vascular tissue structures (hard and soft plaques) independently of the echogeneity contrast with the healthy vessel wall. The potential of EVE was then emphasized by the fact that it provides information that may be unavailable from IVUS alone.

20

In vitro studies with excised vessels were also conducted to further validate EVE feasibility. de Korte et al. computed elastograms from diseased human femoral and coronary arteries. They found different strain values between fibrous, fibrofatty and fatty plaques, indicating the potential of EVE to distinguish different plaque constituents. Those results were compared with IVUS echograms and were corroborated with histology. The elastograms were found capable of demarcating regions within the plaque representing differences in strain, whereas in IVUS echograms, these regions could not be discriminated. Using excised postmortem carotid arteries, similar results were also observed by Brusseau et al.

30

In vitro experimentation of EVE was also conducted by Wan et al., using porcine arteries. In this case, an optical flow method algorithm was used to estimate the displacement from B-mode data. The elasticity modulus distributions were

computed within the framework of the inverse-problem solution. While low spatial resolution of envelope data remains a limitation, the conclusion was the same: EVE may allow identifying different vascular tissue structures such as hard and soft plaques.

However, many difficulties arise from in vivo applications of EVE. For example, one of them concerns the fact that the position of the catheter in the lumen is normally off center and not parallel to the vessel axis, and the geometry of the lumen is generally not circular. In such conditions, tissue displacements may be misaligned with the ultrasound beam, introducing substantial decorrelation between the pre- and the post-tissue-compression signals. Ryan and Foster addressed this problem and proposed, to compensate for misalignment between tissue displacements and the ultrasound beam, the use of a two-dimensional correlation-based speckle tracking method to compute vascular elastograms.

Another potential drawback, associated with EVE in vivo applications, stems from the eventual cyclic catheter movement in the vessel lumen; that is due to the pulsatile blood flow motion. This may constitute source of signal decorrelation between pre- and post-tissue-compression signals. To circumvent such a catheter movement, Shapo et al. proposed to compute the tissue motion in the reference frame of the lumen's geometric center of the angioplasty balloon. This was justified by the fact that such a reference frame depends only on the balloon shape; it thus removes artifacts associated with probe motion within the balloon. Another strategy, proposed by de Korte et al. to minimize artifacts due to catheter motion, was to acquire pre- and post-motion images near end-diastole; that is for a pressure differential of approximately 5 mmHg. Their approach was validated in vivo on patients referred to percutaneous coronary intervention. However, only one elastogram was computed; their results were corroborated with IVUS echograms, showing an area of hard material because of low strain values were observed.

Furthermore, vascular tissue is heterogeneous, and its kinematics is complex. For instance, it may be subjected to rotation, shear and strain. As a consequence to that, changes in the relative position of the speckles within the measurement-window and the changes in speckle morphology induce a noise component, which increases the variance of the motion estimates. In addition, because of the force from within the lumen (from blood pressure excitation or from the compliant intravascular angioplasty balloon), the vessel wall is also under the distension stress; out-of-plane motion will then occur in the kinematics between the pre- and the post-motion images. This is another potential source of signal decorrelation limiting the reliability of tissue motion estimators in EVE.

So far, EVE seems potentially limited by signal decorrelation. Recently, a model-based approach with adaptation for EVE applications was proposed. It assumed that speckle is a material property; such an assumption allows considering the speckle dynamics in the Lagrangian coordinate system instead of the conventional Eulerian coordinate system. From that, the optical flow equations were derived, and were suitably combined with the Lagrangian speckle model estimator (LSME) to assess tissue motion. The approach, detailed in, combines the potential features of the LSME with those of the optical flow equations. It is worth to remember that the LSME is a 2D-tissue-motion estimator, that is implemented through an iterative procedure using the regularized nonlinear minimization method known as the Levenberg-Marquardt (L&M) algorithm. The L&M algorithm is known for its robustness, since it combines the best features of the gradient and of the Gauss-Newton methods. Indeed, the Gauss-Newton solution allows fast convergence in the vicinity of the solution, while the gradient method allows to converge even when the initial guess is outside of the region of convergence for other methods. The optical flow equations are used to compute the Jacobbian matrix that is required to implement the L&M algorithm.

SUMMARY OF THE INVENTION

According to the present invention there is provided a method for detecting the hard plaque in the blood vessels, the method comprising the steps of :

- collecting a sequence of RF images while incrementally adjusting the intraluminal static pressure;
- characterising the the hard plaque from the normal vascular tissue.

10 According to the present invention, there is also provided an apparatus for detecting the hard plaque in the blood vessels, the apparatus comprising :

- a CVIS ultrasound scanner;
- a 30 MHz mechanical rotating single element transducer;
- an oscilloscope;
- a pressuring system; and
- a computer.

20 Endovascular ultrasound elastography (EVE) was recently introduced to supplement IVUS echograms in the assessment of vessel lesions and for endovascular therapy planning. Indeed, changes in the vascular tissue stiffness are characteristic of vessel wall pathologies, and EVE appears as a very appropriate imaging technique to outline the elastic properties of vessel walls. Recently, a model-based approach was proposed to assess tissue motion in EVE. It specifically consisted of a nonlinear minimization algorithm that was adapted to speckle motion estimation. Regarding the theoretical framework, such an approach considered the speckle as a material property; this assumption then led to the derivation of the optical flow equations, which were suitably

combined with the Lagrangian speckle model estimator to provide the full 2D polar strain tensor. In this study, the proposed algorithm was validated in vitro using a fresh excised human carotid artery. The experimental set-up consisted of a CVIS ultrasound scanner, working with a 30 MHz mechanical rotating single element transducer, a digital oscilloscope Lecroy 9374L and a pressuring system. A sequence of RF images was collected while incrementally adjusting the intraluminal static pressure steps. The results showed the potential of EVE to characterize and to distinguish atherosclerotic plaques from the normal vascular tissue. Namely, the geometry as well as some mechanical characteristics of the detected plaque were in good agreement with histology. The results suggested that there may exist a range of intraluminal pressures for which plaque detectability is optimal.

This study consists in an in vitro validation of the adapted LSME. Indeed, a fresh excised human carotid artery was investigated. The experimental set-up consisted of a CVIS ultrasound scanner, working with a 30 MHz mechanical rotating single element transducer, a digital oscilloscope Lecroy 9374L and a pressurizing system. A sequence of 11 RF images was collected while incrementally adjusting the intraluminal static pressure steps. The elastograms were computed using the adapted LSME. Comparisons with histology allow believing in the potential of EVE to characterize and to distinguish atherosclerotic plaques from the healthy vascular tissue. As it will be seen, the results also suggested that there may exist a range of intraluminal pressures for which plaque detectability is optimal.

The method and the apparatus will be detailed in the section below.

DETAILED DESCRIPTION OF A PREFERRED EMBODIMENT OF THE INVENTION

There are presented the experimental set-up description, the data acquisition protocol, and a summary of the Lagrangian strain estimation technique. Results on a fresh excised human carotid artery are presented after, while the discussion of the results and drawing of conclusions and perspectives to this work follow.

10 Materials and methods

Experiments were performed with a fresh excised human carotid artery. This section gives an overview of the specific device that allowed both pressure variations inside the arterial lumen and RF data acquisition; it also summarizes the baselines of the method.

Experimental set-up description

The experimental set-up was mainly made of a CVIS ultrasound scanner, working with a 30-40 MHz mechanical rotating single element, a digital oscilloscope LECROY 9374L and a self-made pressuring system (Figure 16). Artery extremities were fixed to two rigid sheaths by watertight connectors. The intravascular
20 catheter was introduced through the proximal sheath into the lumen of the artery, and then through the distal sheath. The distal sheath was closed with a clamp to insure watertightness of the system. Because of the sheath rigidity and of the system watertightness, injecting fluid inside the system will result in an increase of the pressure inside the arterial lumen. A syringe was then connected to the proximal sheath and the inner pressure was increased or decreased by manually varying the fluid volume (precision : $\Delta V = 0.01$ ml) inside the lumen. The probe was fixed approximately at the centre of the arterial lumen tank to two guiding

elements. This has been performed in order to limit probe motion and accordingly reduce geometrical artefacts.

Data acquisition

In vitro experiments with the fresh carotid artery were performed at room temperature. At each static pressure, a scan of 256 angles was performed. Sampling of the data was phase-synchronised, with the top image synchroniser and the RF signal synchronisation (external output of the CVIS ultrasound scanner). The top image synchroniser allows the user to select an angular position from which the acquisition started; it thus permits the acquisition of sets of images angularly aligned. RF data were digitised at a 500 MHz sampling frequency in 8 bits format, stored on a PCMCIA hard disc in the LeCroy oscilloscope and processed off line.

Methods

The tissue motion estimator, that was used to compute the elastograms, is described in details in. Assuming a small region of interest (ROI) and small tissue motion, it can mathematically be formulated as the following nonlinear minimization problem:

$$\min_{LT_p} \|I(r, \phi, 0) - I_{Lag}(r, \phi, t)\|^2 \quad (1)$$

Where (r, ϕ) defines the image coordinate system, while "t" gives the time. $I(r, \phi, 0)$ is the pre-tissue-motion RF image, and $I_{Lag}(r, \phi, t)$ is the Lagrangian speckle image (LSI) at time "t". So far, it is worth to remember that the LSI was defined as a post-tissue-motion RF image that was compensated for tissue motion, as to achieve the best match possible with $I(r, \phi, 0)$. The appellation "Lagrangian" refers to the Lagrangian description of motion. The minimum of Eq. 1 is obtained using the appropriate $[LT_p]$, a linear transformation matrix.

So far it is important to remember that, as demonstrated in, for a small ROI (Δr , $\Delta \phi$) that is far from the lumen center, motion can equivalently be investigated using either polar or coordinate system. In other words, the following approximation can be done:

$$\Delta \cong LT - I \quad (2)$$

10 where I is the 2D-identity matrix; $[LT]$ is a linear transformation matrix; and Δ can be defined as the Cartesian deformation tensor. Furthermore, it is known that for a small ROI, tissue motion can be approximated by an affine transformation; this can be expressed in Cartesian coordinates as:

$$\begin{bmatrix} p(x, y, t) \\ q(x, y, t) \end{bmatrix} = \underbrace{\begin{bmatrix} \theta_1 \\ \theta_4 \end{bmatrix}}_{Tr} + \underbrace{\begin{bmatrix} \theta_2 & \theta_3 \\ \theta_5 & \theta_6 \end{bmatrix}}_{LT} \begin{bmatrix} x \\ y \end{bmatrix} \quad (3)$$

20 where θ_1 is a function of time t ($\theta_1(t)$). Eq. 3 is the result of a translation (vector $[Tr]$) and of a linear geometrical transformation of coordinates (matrix $[LT]$). Eq. 3 can also be seen as trajectories that describe a tissue motion in a region of constant strain. Assuming that (u_x, u_y) represent the displacement field in the (x, y) coordinate system, $[LT]$ relates the strain tensor (ϵ) through the following relationship:

$$\begin{bmatrix} u_x \\ u_y \end{bmatrix} = \begin{bmatrix} p(x, y, t) - x \\ q(x, y, t) - y \end{bmatrix} = \begin{bmatrix} \theta_1 \\ \theta_4 \end{bmatrix} + \Delta \begin{bmatrix} x \\ y \end{bmatrix}$$

$$\text{with } \Delta = \begin{bmatrix} \theta_2 - 1 & \theta_3 \\ \theta_5 & \theta_6 - 1 \end{bmatrix}, \quad (4)$$

$$\epsilon_{ij}(t) = \frac{1}{2} [\Delta_{ij}(t) + \Delta_{ji}(t)]$$

The radial strain then becomes equivalent to ϵ_{22} ($= \Delta_{22} = \theta_6 - 1$). The map of ϵ_{22} distribution provides the radial elastogram.

Eq. 1 was numerically solved with an iterative procedure, that uses the regularized nonlinear minimization method, known as the Levenberg-Marquardt (L&M) algorithm. The optical flow equations were used to compute the Jacobian matrix ($[J]$) that is required to implement the L&M algorithm. $[J]$ was derived in; at the k^{th} iteration, it can be expressed as:

$$J_k = \begin{bmatrix} \frac{\partial I_{\text{Lag}}}{\partial \theta_1} & \frac{\partial I_{\text{Lag}}}{\partial \theta_2} & \dots & \frac{\partial I_{\text{Lag}}}{\partial \theta_n} \\ \vdots & \vdots & & \vdots \\ \frac{\partial I_{\text{Lag}}}{\partial \theta_1} & \frac{\partial I_{\text{Lag}}}{\partial \theta_2} & \dots & \frac{\partial I_{\text{Lag}}}{\partial \theta_n} \end{bmatrix} \quad (5)$$

θ_i are motion parameters, as given by Eqs 3 and 4. $[J_k]$ is a " $m \times n$ " matrix, where " m " is the number of pixels in the ROI and " n ", the 6 elements of the affine transformation. To complete, it was demonstrated in that, at the $(k-1)^{\text{th}}$ iteration, the Jacobian matrix can be implemented as:

$$\frac{\partial I_{\text{Lag}}(\bar{\theta}^{k-1})}{\partial \bar{\theta}} \approx \frac{\partial I(\bar{\theta}^{k-1})}{\partial \bar{\theta}} = - \left\{ \frac{\partial I}{\partial x}, \frac{\partial I}{\partial x} x, \frac{\partial I}{\partial x} y, \frac{\partial I}{\partial y}, \frac{\partial I}{\partial y} x, \frac{\partial I}{\partial y} y \right\} \quad (6)$$

Eq. 6 gives the full expression for the 6 components of the Jacobian matrix $[J_k]$ (Eq. 5). The following section presents results obtained with the proposed method, using data acquired from the excised human carotid artery.

Results

Results are reported here for experiments performed with the excised carotid artery. This artery was characterized by a thin atherosclerotic plaque. A set of 11 RF images were acquired for consecutive increasing physiologic fluid pressure levels. Figure 17 presents a histological section along with an IVUS image. Histology (Figure 17a) shows a very small atherosclerotic plaque (located at 3 o'clock), that is only restricted to a confined angular sector. The coloration with saffron haematoxylin-eosin revealed that the plaque contained cholesterol crystals and inflammatory cells. Notice that the IVUS image does not allow to clearly differentiate the plaque from the healthy vascular tissue.

10

To implement the method, a $526 \mu\text{m} \times 781 \mu\text{m}$ (200 samples \times 20 RF lines) measurement-window, with 86 % axial and 90 % lateral overlaps, was used. For the purpose of compensating for strain decay, the elastograms were post-processed. In other words, they were modulated with a function proportional to the square of the vessel radius. Furthermore the elastograms were low-pass filtered, using a $500 \mu\text{m} \times 500 \mu\text{m}$ (6×6 pixels) kernel Gaussian filter. Figure 18 presents an overview of 10 elastograms that were computed. For instance, Figure 18a is for the lowest intraluminal pressure, while Figure 18j is for the highest one. Indeed, maximum strain values close to .6 % are observed in Figure 18a, whereas the maximum is close to 3 % in Figure 18j. To summarize, elastograms in Figs 18a and 18j respectively are the least representative, whereas those from Figure 18c to Figure 18e present very good plaque detectability, accuracy in plaque dimensions, and significant contrast between plaque and surrounding tissue. In other words, it does exist an optimal range of intraluminal pressures for which tissue motion estimation appears optimal.

20

30

Figure 19 presents comparisons between histology (Figure 19a) and elastogram (Figure 19b). This elastogram (the same as Figure 18c) was chosen simply because it appears in the range of optimality described above. Indeed, looking at the plaque geometry, the dimensions are very close to those observed in histology. Furthermore, from a biomechanical point of view, stiffness ratio between

plaque and healthy vascular tissue is close to 3; this is quite reasonable, regarding ranges of Young's moduli for atherosclerotic plaques [xx kPa, yy kPa] and for normal vascular tissue [aa kPa, bb kPa] in the literature.

Non-invasive Vascular Elastography: Theoretical Framework

Changes in vessel wall elasticity may be indicative of vessel pathologies. It is known, for example, that the presence of plaque stiffens the vascular wall, and that the heterogeneity of its composition may lead to plaque rupture and thrombosis. Another domain of application where ultrasound elastography may be of interest is the study of vascular wall elasticity to predict the risk of aneurysmal tissue rupture. In this paper, this technology is introduced as an approach to non-invasively characterize superficial arteries. In such a case, a linear array ultrasound transducer is applied on the skin over the region of interest, and the arterial tissue is dilated by the normal cardiac pulsation. The elastograms, the equivalent elasticity images, are computed from the assessment of the vascular tissue motion. Investigating the forward problem, it is shown that motion parameters might be difficult to interpret; that is because tissue motion occurs radially within the vessel wall while the ultrasound beam propagates axially. As a consequence of that, the elastograms are subjected to hardening and softening artefacts, which are to be counteracted. In this paper, the Von Mises coefficient is proposed as a new parameter to circumvent such mechanical artefacts and to appropriately characterize the vessel wall. Regarding the motion assessment, the Lagrangian estimator was used; that is because it provides the full 2D-strain tensor necessary to compute the Von Mises coefficient. The theoretical model was validated with biomechanical simulations of the vascular wall properties. The results allow believing in the potential of the method to differentiate hard plaques and lipid pools from normal vascular tissue. Potential *in vivo* implementation of non-invasive vascular elastography to characterize abdominal aneurysms and superficial arteries such as the femoral and the carotid is discussed.

Index terms: Ultrasound elastography, Vascular wall, Mechanical properties, Non-invasive scanning, Mathematical modeling, Vascular pathologies.

INTRODUCTION

Pathological conditions often induce changes in biological tissue stiffness. That is, for example, the basic hypothesis supporting palpation as a screening method to detect hard tumors in the breast, prostate and other organs. However, in many instances, such an approach is impracticable when deep organs are considered. This gave rise to elasticity imaging, which aims to outline the elastic properties of biological soft tissues using ultrasound.

In the early nineties, Ophir *et al.* introduced elastography, which is defined as biological tissue elasticity imaging. Primary objectives of elastography were to complement B-mode ultrasound as a screening method to detect hard areas in the breast, and to investigate prostate cancers. Such approaches are sometimes referred to as *computed palpation*. Basically, the tissue under inspection is externally compressed and the displacement between pairs of pre- and post-compression radio frequency (RF) lines is estimated using cross-correlation analysis. The strain profile in the tissue is then determined from the gradient of the axial displacement field.

Elastography has also found application in vessel wall characterization. Until now, vascular elastography is invasive and is known in the literature as intravascular ultrasound elastography or, sometimes, as endovascular elastography (EVE). In EVE, the vascular tissue is compressed by applying a force from within the lumen. Indeed, the compression can be induced by the normal cardiac pulsation or by using a compliant intravascular angioplasty balloon. Such a balloon may also be used to stabilize the EVE catheter position in the lumen. This approach can be seen as a complement to B-mode intravascular ultrasound (IVUS).

REPORTED WORKS ON EVE (RELEVANT TO THE CURRENT STUDY)

Simulations and phantom studies

One of the first investigations on endovascular elastography was presented by Soualmi *et al.* in 1997. Indeed, they used finite element analysis to better understand the vessel wall elasticity images. To validate the feasibility of EVE, phantom studies have been proposed. In most cases, tissue-mimicking phantoms with typical morphology and hardness topology synthesizing atherosclerotic vessels were constructed, de Korte *et al.* concluded that EVE may allow identifying hard and soft plaques independently of the echogeneity contrast between the plaque and the vessel wall. The potential of such an approach was emphasized by the fact that it provides information that may be unavailable from IVUS alone.

In vivo, the position of the catheter in the lumen is normally off center, and the geometry of the lumen is generally not circular. In such cases, tissue displacements may be misaligned with the ultrasound beam, introducing substantial decorrelation between the pre- and the post-tissue-compression signals. As to prevent such limitations, Ryan and Foster proposed the use of a two-dimensional correlation-based speckle tracking method to compute vascular elastograms. While questioning the limitations of the lateral tracking performance, they concluded their phantom studies claiming that EVE may provide a new spectrum of information to aid in the assessment of atherosclerotic lesions.

Additionally, *in vivo*, the catheter may cyclically move in the lumen because of the pulsatile blood flow motion. This constitutes another potential source of decorrelation for the pre- and the post-tissue-compression signal treatment. To counteract that, Shapo *et al.* proposed to compute the tissue motion in the reference frame of the lumen's geometric center of the angioplasty balloon. Such a reference frame depends only on the balloon shape, it thus removes artefacts

associated with probe motion within the balloon. Their phantom investigations also tended to demonstrate the feasibility of EVE and its potential to differentiate between hard and soft plaques.

More recent results on endovascular phantom studies were obtained by Brusseau *et al.*. Instead of the traditional correlation-based methods, they used an iterative approach to compute a scaling factor between pre- and post-compression signal segments. From that, the strain was estimated. This adaptive method is expected to be accurate in a wider range of strains than the commonly used
10 gradient-based methods, and it may prove better for investigating highly heterogeneous tissues.

In vitro studies with excised vessels

One more step to validate the feasibility of EVE is *in vitro* experiments. de Korte *et al.* computed elastograms from diseased human femoral and coronary arteries. They found different strain values between fibrous, fibro-fatty and fatty plaques, indicating the potential of EVE to distinguish different plaque constituents. Such results were compared with IVUS echograms and corroborated with
20 histology. One of their principal findings was that the elastograms were capable of demarcating regions within the plaque representing differences in strain, whereas in IVUS echograms, these regions could not be discriminated. Using excised postmortem carotid arteries, similar results were recently observed by Brusseau *et al.*

In vitro endovascular elastography also was conducted by Wan *et al.* They used an algorithm-based optical flow method to estimate the displacement from B-mode data collected from porcine arteries. They also computed the elasticity modulus distributions within the framework of the inverse-problem solution
30 (estimation of the Young's modulus). While low spatial resolution of envelope data

remains a limitation, the method seemed encouraging because of the highest accessibility of B-mode compared to RF instrumentation.

In vivo studies

Currently, *in vivo* applications of EVE are scarce. de Korte *et al.* attempted to compute elastograms *in vivo* from patients referred to percutaneous coronary intervention. Indeed, as pre-intervention IVUS assessment of the lesions was performed, RF data were acquired to compute elastograms. To minimize artefacts due to catheter motion, pre- and post-tissue-motion images were acquired near end-diastole; that is for a pressure differential of approximately 5 mmHg. One elastogram was presented; it identified an area as being composed of hard material since low strain values were found. Such a finding was corroborated with the IVUS echograms that revealed a large calcified area. That result allows believing in the potential of EVE for follows-up of patients with vascular diseases.

NON-INVASIVE VASCULAR ELASTOGRAPHY (NIVE)

So far, vascular elastography is invasive. Its clinical application is thus restricted to a complementary tool to assist IVUS echograms in pre-operative lesion assessments and to plan endovascular therapy. It has also found application in *in vitro* studies to characterize vascular tissues. Nevertheless, elastography is a very attractive and promising approach to characterize the mechanical properties of vascular walls. In this paper, the feasibility of non-invasive vascular elastography is investigated.

In the next sections, the Lagrangian estimator and its implementation for vessel wall characterization are summarized. The full 2D-strain tensor ϵ is provided, but the so-called elastogram is given by the strain component ϵ_{yy} , which corresponds to the strain in the direction of the ultrasound propagation.

Investigating the forward problem, it is shown in section 2 that such an elastogram is subjected to hardening and softening artefacts; that is explained by the fact that motion occurs radially within the vessel wall while the ultrasound beam propagates axially. To circumvent such incoherence, the Von Mises coefficient is proposed as a new parameter to non-invasively characterize the vessel wall. Results from biomechanical simulations of wall tissue displacement validate the potential of the approach to accurately differentiate hard plaques and lipid pools from the normal vascular tissue. Potential *in vivo* implementation of non-invasive vascular elastography to characterize abdominal aneurysms and superficial arteries, such as the femoral and the carotid, is discussed in section 4.

METHODOLOGY

In conventional elastography, an axial compression is applied so that the tissue motion occurs in the ultrasound beam axis. In such a case, 1D estimator can provide reliable tissue motion assessment. In some circumstances, 2D companding may be required to compensate for non-axial motion. In non-invasive vascular elastography (NIVE), the challenge stems from the fact that motion occurs radially within the vessel wall section while the ultrasound beam propagates axially (linear array transducers are considered in the present study). Regarding that, 1D estimators are not appropriate. In this paper, the Lagrangian speckle model estimator (LSME) is thus proposed to non-invasively characterize vascular tissues. Indeed, the LSME is a 2D model-based estimator that allows computing the full 2D-strain tensor. The approach relies on a tissue-motion model and on a dynamic image-formation model that are summarized in the next sections.

THE TISSUE-MOTION MODEL

Subjected to blood flow pressure, the apparent motion of an artery is dilation; however, because of the boundary conditions imposed by the surrounding tissues and organs, the vascular wall itself is compressed. Such a compression induces a radial strain that is maximum at the inner wall and minimum at the outer wall; this observation is referred to, in the literature, as the strain decay. However, as illustrated in Figure 20, motion occurs radially in NIVE and is parallel to the ultrasound beam only at angles ϕ of 0° and 180° (note that cross-sectional images are considered here). Moreover, the vascular tissue is heterogeneous; it is thus expected to deform non-uniformly. Accordingly, proceeding to motion estimation requires subdividing the region under study into several 2D sub-regions of interest (ROI). This is shown in Figure 21, where the ROIs are represented by the measurement-windows W_{mn} .

For small ROIs (W_{mn}), tissue motion can be approximated by the zero-order and first-order terms of a Taylor-series expansion; this can be expressed as:

$$\begin{bmatrix} p(x,y,t) \\ q(x,y,t) \end{bmatrix} = \underbrace{\begin{bmatrix} \theta_1 \\ \theta_4 \end{bmatrix}}_{Tr} + \underbrace{\begin{bmatrix} \theta_2 & \theta_3 \\ \theta_5 & \theta_6 \end{bmatrix}}_{LT} \begin{bmatrix} x \\ y \end{bmatrix} \quad (1)$$

where θ_i is a function of time t ($\theta_i(t)$). Equation 1 defines an affine transformation, i.e., it is the result of a translation (vector $[T_r]$) and of a linear geometrical transformation of coordinates (matrix $[LT]$). Equation 1 can also be seen as trajectories that describe a tissue motion in a region of constant strain. Strain is usually defined in terms of the gradient of a displacement field; hence, as $p(x,y,t)$ and $q(x,y,t)$ represent the new position of a point (x,y) , the (u,v) components of the displacement vector in the (x,y) system are given by:

$$\begin{bmatrix} u \\ v \end{bmatrix} = \begin{bmatrix} p(x,y,t)-x \\ q(x,y,t)-y \end{bmatrix} = \begin{bmatrix} \theta_1 \\ \theta_4 \end{bmatrix} + \Delta \begin{bmatrix} x \\ y \end{bmatrix} \quad (2)$$

with: $\Delta = \begin{bmatrix} \theta_2 - 1 & \theta_3 \\ \theta_5 & \theta_6 - 1 \end{bmatrix}$

The ε_{ij} , which are the components of the strain tensor ε , can then be defined in terms of the θ parameters as:

$$\varepsilon_{ij}(t) = \frac{1}{2} [\Delta_{ij}(t) + \Delta_{ji}(t)] \quad (3)$$

For an ultrasound pulse propagating in the y-axis direction, ε_{xx} and ε_{yy} represent respectively the lateral and the axial strains; $\varepsilon_{xy} = \varepsilon_{yx}$ is the shear strain.

- 10 Because conventional elastography assumes a constant stress distribution in the ROI, the axial strain is inversely proportional to the Young's modulus. Accordingly ε_{yy} , known in the literature as the elastogram, can be seen as a map of the tissue stiffness. In other words, elastography may allow identifying different tissue structures such as hard plaques and lipid pools, or heterogeneity in the aneurysmal vessel wall.

THE DYNAMIC IMAGE-FORMATION MODEL

- 20 It is assumed that the image formation can be modeled as a linear space-invariant operation on a scattering function. If it is further assumed that the motion occurs in plane strain conditions (that is no transverse motion is involved), then the following simple 2D model can be used:

$$I(x,y) = H(x,y) \otimes Z(x,y) \quad (4)$$

where $I(x,y)$ is the RF image, $H(x,y)$ is the point-spread function (PSF) of the ultrasound system, \otimes is the 2D convolution operator, and $Z(x,y)$ is the acoustic impedance function, which can be modeled as a white Gaussian noise (random distribution of scatterers within the ROI).

Let's now derive the 2D dynamic image-formation model for an in-plane tissue motion. For small ROIs such as in Fig. 20, motion impressed on the tissue ($Z(x,y)$) can be assumed an affine transformation (Eq. 1). This means that such a motion can be set by only changing the (x,y) coordinates. Without loss of generality, it is assumed that the translation $[Tr]$ is absent (no rotation of the blood vessel during pulsation) or is appropriately compensated for, and can thus be neglected. The compensation for translation can be done using correlation techniques; such a processing is known, in the literature, as *companding*. It is also interesting to notice that impress $[LT]$ on the tissue requires to compute the inverse transformation $[LT^{-1}]$ on the coordinates. Hence, for an (x,y) in-plane motion, the 2D RF dynamic image-formation model is given by:

$$I(x,y,t) = H(x,y) \otimes Z_{LT^{-1}}(x,y) \quad (5)$$

where $Z_{LT^{-1}}(x,y)$ indicates a change in coordinates for the function $Z(x,y)$; that change involves the 2×2 matrix $[LT^{-1}]$. Implicitly, this means that $[LT]$ is invertible. This assumption is valid for incompressible continuum. Indeed, in such a case, the determinant of $[LT]$ (also known as the Jacobbian) is unity, so $[LT]$ is nonsingular and invertible.

Biomechanical simulation of tissue motion

As a first step, the Matlab software (The MathWorks Inc, MA, USA, ver. 6.0) was used to simulate the simple case of a homogeneous vessel wall. The process is schematically presented in Fig. 21 and can be summarized as follows. It started

by generating in Matlab a scattering function that simulated the acoustical characteristics of a transverse vascular section; that provided $Z(x,y)$. The analytical solution for a pressurized thick-wall cylindrical blood vessel embedded in an elastic coaxial cylindrical medium was then derived (Appendix I). From that, the axial and lateral displacement fields were computed. Those displacement fields were applied upon $Z(x,y)$ to perform motion and then to provide $Z_{LT^{-1}}(x,y)$. Finally, $Z(x,y)$ and $Z_{LT^{-1}}(x,y)$ were respectively convolved with $H(x,y)$ (the PSF) to produce the pre- and the post-tissue-motion RF images ($I(x,y,0)$ and $I(x,y,t)$, $t \neq 0$). As it is seen in the next section, those two images constitute the inputs to the Lagrangian speckle model estimator.

A pathologic (heterogeneous) vessel wall was also investigated, that is the case where the lumen is narrowed by the presence of a hard plaque at the intima. The process to simulate the pre- and the post-tissue-motion RF images was similar to the homogeneous case study, except that the Ansys finite-element modeling software (Ansys Inc., Canonsburg, PA, ver. 6.0) was used to describe the static mechanical behavior and the kinematics of the pressurized heterogeneous vessel.

20 THE LAGRANGIAN SPECKLE MODEL ESTIMATOR (LSME)

The Lagrangian speckle estimator was introduced and widely discussed. It is a model-based estimator that relies on the previous tissue-motion and dynamic image-formation models. It can be formulated as a nonlinear minimization problem. The LSME iteratively computes the $[LT]$ that allows the best match within a sequence of images; it thus provides the strain tensor through Eqs 1, 2 and 3. For simplicity and without loss of generality, let's consider only two images of the sequence: $I(x,y,t)$ at $t = 0$, that is $I(x,y,0) = I_0(x,y)$ which is labeled as the pre-motion image; and $I(x,y,t)$ at a given time ($t_1 \neq 0$) such that $I(x,y,t_1) = I_1(x,y)$, which

corresponds to the post-motion image. The estimator is schematically represented by the block-diagram of Fig. 22 and it can be expressed as:

$$\underset{\psi}{MIN} \quad \|I_0(x,y) - I_{lag}(x,y)\|^2 \quad (6)$$

with $\psi = [Tr; LT(:)]^4$. $I_{lag}(x,y)$ is labeled as the Lagrangian speckle image; it can be expressed as $[I_1(x,y)]_{LT}$, that is the post-motion RF image $I_1(x,y)$ compensated for tissue motion. In Fig. 22, this is implemented through an adapted version of the Levenberg-Marquardt (L&M) minimization algorithm.

10

Such an estimator provides many advantages. The major one is related to the fact that it allows computing the full 2D-strain tensor (Eq. 3). As Δ_{xx} ($= \epsilon_{xx}$) and Δ_{yy} ($= \epsilon_{yy}$), the divergence parameters, provide information about tissue stiffness, the shear parameters, Δ_{xy} and Δ_{yx} , may provide useful insights on the heterogeneous nature of the tissue under investigation. However, one should be aware that the accuracy of the lateral parameters (Δ_{xx} and Δ_{xy}) is potentially limited by the lateral resolution of ultrasound systems (the lateral resolution, that depends on the ultrasound beam characteristics, is generally lower than the axial resolution determined by the transducer bandwidth and the ultrasound system electronic properties).

20

THE FORWARD PROBLEM: TISSUE MOTION ANALYSIS

For a continuum, motion can be described in a Lagrangian coordinate system or in an Eulerian coordinate system. In the literature, the Eulerian coordinate system is sometimes referred to as the observer's coordinate system, whereas the Lagrangian coordinate system is known as the material coordinate system. The material coordinates allow to express each portion of the continuum

⁴ This is the Matlab notation for augmented vector (:) and matrix vectorisation (:). Hence, ψ is a 6×1 vector built from the 2×1 Tr vector and the 4×1 vectorisation of LT.

as a function of time and position. The difference between these two coordinate systems is illustrated in Fig. 23, where the (x,y) constitutes the observer's coordinates and the (r,ϕ) defines the material coordinates.

10 With most imaging systems, such as ultrasonography, the observer's and the material coordinate systems are generally the same; hence, most tissue motion estimators use, by definition, the observer's coordinate system. However, the material coordinates were presented as a suitable way to describe speckle dynamics. It was demonstrated that such a coordinate system leads to appropriate
10 signal processing, which allows to counteract speckle decorrelation effects in tissue motion assessment. In non-invasive vascular elastography, as illustrated in Fig. 20, the observer's coordinate system is the Cartesian (x,y) -plane. This system is different from the motion coordinate system that is in the radial (r,ϕ) -plane. In such a situation, the parameters of an estimator are expected to be very difficult to interpret. The challenge of non-invasive vascular elastography greatly concerns the interpretation of the estimated motion parameters to characterize the vascular tissue. In the next sections, such motion parameters are investigated and a proposition is given for a new tissue characterization parameter.

20 *Motion analysis for a homogenous tissue*

To initiate the forward problem, a pathology-free situation was considered, that is the simplest case of a circular, axis-symmetric and homogeneous vessel section. To take into account the constraints induced by the environmental tissues and organs, it is hypothesized that the vessel section is embedded in an infinite medium of higher Young's modulus. An exact solution of a pressurized thick-wall cylindrical blood vessel of inner and outer radii R_i and R_o respectively, embedded in an elastic coaxial cylindrical medium of radius R_e , is derived for our study in linear elasticity. The details are presented in Appendix I. In this study, it is
30 assumed that the plane strain condition for the vessel wall applies and also that

the two media are incompressible and isotropic. Referring to Appendix I, the displacement gradient components (Eq. 2) are given by:

$$\Delta(x,y) = \begin{bmatrix} K_{\infty} \frac{y^2 - x^2}{(x^2 + y^2)^2} & -2K_{\infty} \frac{xy}{(x^2 + y^2)^2} \\ -2K_{\infty} \frac{xy}{(x^2 + y^2)^2} & K_{\infty} \frac{x^2 - y^2}{(x^2 + y^2)^2} \end{bmatrix} \quad (7)$$

with:

$$K_{\infty} = \frac{3}{2} P_b \left[E^{(1)} \left(\frac{1}{R_i^2} - \frac{1}{R_o^2} \right) + \frac{E^{(2)}}{R_o^2} \right]^{-1} \quad (8)$$

Where ⁽¹⁾ and ⁽²⁾ respectively describe the vessel wall and the external medium; P_b defines the blood pressure and E is the Young's modulus.

Using Matlab software, Eqs 7 and 8 were processed to simulate the dynamics of a homogeneous vessel section subjected to an intraluminal pressure gradient of 73 mmHg; that is close to 6 % intraluminal dilation⁵ for the constitutive model presented in Appendix I. The physical vessel dimensions were 7-mm outer diameter and 4-mm inner diameter as to approximate the physiological case of a femoral artery. Figures 24a and 24b respectively present the lateral and axial displacement fields. Maximum motion occurred at the lumen. Figures 24c to 24f present the Δ_{ij} components of Eq. 7, which are respectively the lateral strain, the lateral shear, the axial shear and the axial strain.

The elastogram, i.e. the map of the axial strain distribution, is generally presented as a grayscale image. Because in conventional elastography, external y-axis compression is applied and also because 1D y-axis motion is assessed, Δ_{yy} is expected ≤ 0 . Traditionally, smaller strain amplitude values are associated with

⁵ Notice that 6 % intraluminal dilation is equivalent to 3 % compression of the intraluminal wall.

harder regions and are printed in black; equivalently, higher strain amplitude values are associated with softer regions and are printed in white. However in NIVE, as it can be observed in Fig. 24f, dilation can also be detected ($\Delta_{yy} \geq 0$) in the elastogram. In an elastographic sense, the dilation regions can be misinterpreted as soft tissue. Indeed, in Fig. 24f, two harder zones ($\Delta_{yy} \leq 0$) likely seem to be identified at 12 and 6 o'clock. Because, for the conditions simulated, the vessel wall is homogeneous, such a phenomenon is referred to as hardening artefact. Inversely, two softer zones ($\Delta_{yy} \geq 0$) at 3 and 9 o'clock seem also to be identified; they are referred to as softening artefacts. Such motion artefacts stem from the fact that motion occurs radially and is observed in Cartesian coordinates; this can constitute a potential limitation to non-invasive vascular elastography.

To go further with this observation, let's consider the motion parameters in their natural polar coordinate system, or material coordinate system. In Fig. 25a, is presented the radial displacement field computed from the lateral and axial displacement fields (Figs 24a and 24b, respectively). This radial displacement field is also presented in a polar (r, ϕ) coordinate system (Fig. 25b). The gradient of the latter displacement field thus provides the radial strain (Fig. 25c). In Fig. 25d is shown a plot of the radial strain at $\phi = \pi$. One can observe the monotonic profile of this plot, being maximal at the lumen and minimal at the outer side of the vessel; such a phenomenon is a consequence of the boundary conditions and is known in the literature as the strain decay. Finally in Fig. 25e, the radial strain is reported back in the (x, y) coordinate system. Regardless of the strain decay phenomenon, one can observe that no specific hard or soft region is identified. Fig. 25e thus illustrates a strain profile that is quite representative of a homogenous vessel wall behavior.

A new parameter for tissue characterization

Hopefully, elastograms such as the one in Fig. 25e are required to appropriately characterize the vessel wall. However, to prevent signal decorrelation in NIVE, motion is to be studied in the transducer coordinate system; that is the (x,y)-Cartesian coordinates. Accordingly, elastograms are expected to be as artefactual as the one in Fig. 24f. However, taking a close look at all the motion parameters in Fig. 24, one can observe that Δ_{xx} and Δ_{yy} are complementary, while $\Delta_{xy} = \Delta_{yx}$. In this paper, the Von Mises (VM) coefficient is proposed as a parameter to characterize the vessel wall. Indeed, VM is independent of the coordinate system and is a combination of the four displacement gradient components (Δ_{ij}) that is mathematically expressed as:

$$\begin{aligned}\xi &= \sqrt{\varepsilon_{xx}^2 + \varepsilon_{yy}^2 - \varepsilon_{xx}\varepsilon_{yy} + 3\varepsilon_{xy}^2} \\ &= \sqrt{\Delta_{xx}^2 + \Delta_{yy}^2 - \Delta_{xx}\Delta_{yy} + \frac{3}{4}(\Delta_{xy} + \Delta_{yx})^2}\end{aligned}$$

(9)

In Fig. 26, a comparison between ξ and the radial strain (Fig. 15e) is presented. Qualitatively, both parameters are equivalent. Fig. 26c shows the plots for the radial strain (—) and ξ (---) at $x = 0$. Analyzing those curves, one can observe that the VM coefficient likely improves the contrast between higher and lower strains while the profile remains the same. Moreover, regardless of the strain decay, ξ (as well as the radial strain) is interestingly free of hardening or softening artefacts. It is thus allowed believing that such a parameter could be very suitable to non-invasively characterize the vessel wall. To corroborate such an assumption, a more complex geometry, that is a heterogeneous vessel wall, is considered in the next section.

Characterization of an heterogeneous vessel wall

The case of a pathologic vessel wall is now investigated, that is when the lumen is narrowed by the presence of a hard plaque at the intima. It is assumed that the plaque is 10 times stiffer than the normal vascular tissue, a lipid pool 10 times softer than the normal vascular tissue immediately surrounds it. The geometry is schematically presented in Fig. 27a. To have approximately the same range of strains as in the homogenous case study, the intraluminal pressure gradient was set at 40 mmHg (intraluminal dilation close to 6 %). The outer diameter of the vessel was again set at 7 mm. In Figs 27b to 27e, the four Δ_{ij} tensor components are presented. One can appreciate the very complex patterns of those parameters. The elastogram (i.e., the axial strain map), presented in Fig. 27e (equivalently the lateral strain map of Fig. 27b), shows a region of relatively high strain values; this corresponds to the location of the lipid pool as it can be expected. Nevertheless, the elastogram does not undoubtedly allow differentiating between the plaque, the lipid pool and the normal vascular tissue.

In Fig. 28b, the *elastogram* computed using the VM parameter (ξ) is presented. Obviously, three main regions are identified: the hard plaque with lower strain values, the lipid pool with higher strain values and the normal tissue with moderate strain values. This elastogram can qualitatively be compared with the radial strain map presented in Fig. 28a. For a quantitative comparison, Fig. 18c shows plots of the radial strain and ξ at $x = 0$. In both of them, the three specific regions can be clearly differentiated. As it was also observed in the homogeneous case study, it is interesting to point out that ξ substantially improves the contrast between soft and hard tissues.

These observations are interesting and allow believing in the potential application of NIVE. Nevertheless, some artefacts still remain, specifically at the intersections between hard, soft and normal tissues. This is, unfortunately, quite expectable since those are sites of maximal stress concentrations. Such a problem could have been circumvented if the Young's modulus, instead of a strain parameter, was computed in ultrasound elastography. Another problem, which

could arise in the real-life situation, concerns the limited lateral resolution of current ultrasound systems. Because of that, variances in the lateral motion estimates (Δ_{yx} and Δ_{xy}) may in practice be large. This may constitute a potential limitation to the assessment of ξ . In the next sections, we present results from simulated RF data. All elastograms were computed with the Lagrangian speckle model estimator (LSME).

RESULTS

APPLICATION OF THE LSME TO SIMULATED RF ECHO SIGNALS

The dynamic image-formation model of Eq. 5 was used to simulate sequences of RF images. As illustrated in Fig. 21, the vessel section (the scattering function $Z(x,y)$) was modeled as a 2D white Gaussian noise (number of scatters in a resolution cell $\gg 5$). The lumen and the tissue surrounding the vessel were assumed to be respectively 2.5 and 1.67 times less echoic than the wall. $Z(x,y)$ was low-pass filtered before considering motion; the post-motion scattering function was expressed as $Z_{LT}(x,y)$. The radial displacement field used to mimic motion was obtained from the analytical biomechanical model presented in Appendix I (normal cylindrical vessel), and Ansys simulations (obstructed vessel with a plaque). It is important to remember that such a motion is normally induced by the cardiac pulsation. The imaging system PSF ($H(x,y)$) was defined as a 2D Gaussian wavelet, modeling a 10 MHz transducer with a 60% bandwidth at -3dB and a beam width (width at half maximum) of 0.6 mm. The simulated RF images (pre- and post-tissue motion images) were used as inputs by the LSME to compute the four displacement gradient components. Are presented, in the next two sections, results for the homogenous and the heterogeneous vessel wall studies, respectively.

Motion estimation for a homogenous vessel wall

As defined in section 2.4.1, a vessel of 7-mm outer diameter and 4-mm inner diameter was simulated. To take into account the surrounding tissue, the echo field was 8 mm \times 8 mm; that is 3000 samples axially \times 150 RF lines laterally. To apply the LSME, a measurement-window of 533 μ m \times 1 066 μ m (200 samples \times 20 RF lines) was chosen. As illustrated in Fig. 20, the motion was estimated for windows W_{mn} with 88 % and 90 % axial and lateral overlap, respectively.

10 The windowed data of the pre and post-tissue-motion images were pre-processed to compensate for tissue translation using 2D correlation. This left the LT matrix and eventually a small residual translation motion (θ_1 and θ_4) to estimate. In this paper, the translation motion parameters θ_1 and θ_4 were not considered. The four displacement gradient components, as computed with the LSME, are presented in Figs 29a to 29d.

20 Figs 29a and 29b present the maps of the lateral strain and shear, respectively. As it can be expected, those motion parameters show large variances. That is due to the limited lateral image resolution (53 μ m per RF line, for this study) used to simulate the performance of current ultrasound systems. Nevertheless, the lateral strain values are observed in a range, on average, that includes the theoretical results (Fig 14c). Figs 29c and 29d present maps of the axial shear and strain, respectively. The elastogram (Fig. 29d) is quantitatively similar to the theoretical one (Fig. 24f), showing strains in the interval of [-3 %, 3 %]. The pattern of the axial shear is also quantitatively similar to the theoretical one (Fig. 24e).

30 Are presented in Fig. 30, comparisons between the simulated and theoretical VM parameters ξ . For a quantitative comparison, Fig. 30b presents an average of three curves around $x = 0$, and at Fig. 30d the curve corresponds to $x =$

0. Notice the presence of strain decay in each curve. It is also important to emphasize that close to the lumen, motion estimates may be, in some instances, inaccurate. That is explained by the fact that in such locations, the measurement-windows may overlap the vessel wall (where pre- and post-tissue-motion signals are expected to be coherent) and the lumen (where pre- and post-tissue-motion signals are expected to be uncorrelated). As a consequence of that, such motion estimates may not be reliable. Because one is now aware of some of the eventual difficulties that could be encountered and, in the light of the promising results of Fig. 30, it allows believing in the potential of NIVE. In the next section, the heterogeneous vessel wall is investigated.

Motion estimation for a heterogeneous vessel wall

The vessel wall investigated is the same as in section 2.4.3. The data acquisition system (i.e. the PSF) and the parameters for motion assessment (W_{mn} , overlap, etc.) are the same as in the section 3.1.1 above. In Fig. 31, the results for the four displacement gradient components are presented. Figs 31a and 31b present the maps for the lateral strain and shear, respectively. As for the homogenous case, the variances for those motion estimates are large; they do not clearly allow differentiating between hard and soft structures. Nevertheless, a reasonable range of strain values is, on average, observed when comparisons are made with Fig. 27. The simulated elastogram (Fig. 31d) shows a slight underestimation of the axial strain values when compared to the theoretical one (Fig. 27e); strain values in the interval of $[-2,5 \%, 2,5 \%]$ are observed instead of $[-6 \%, 6 \%]$. That is, at least partially, due to the fact that high strain areas at the intersections between hard, soft and normal tissues are more prominent in the theoretical elastogram than in the simulated one. The axial shear is also qualitatively and quantitatively similar to the theoretical one (Fig. 27d). In Fig. 32a, is shown the composite elastogram (ξ). Even with the presence of large variances on the estimates of the lateral motion parameters, ξ allows identifying the hard

plaque and the soft lipid pool. For a quantitative validation, Fig. 32b shows an average of three curves around $x = 0$. Clearly the hard plaque (strain values less than 1 %) and the lipid pool (strain values around 4 %) are detected. Because of the strain decay phenomenon, the normal tissue presents strain values standing from 1 % up to 2 %. For comparison purpose, the same results are shown for the theoretical ξ in Figs 32c and 32d.

DISCUSSION

The vascular tissue is made of elastin, collagen and smooth muscle cells; its mechanical properties are thus very complex. Pathological conditions of such a tissue often induce changes in the vessel wall elasticity. For example, plaque deposit stiffens the vascular wall and then counteracts its dilation under systolic blood pressure. On the other hand, peripheral aneurysmal rupture of the aorta has been linked to changes in the proportion and integrity of collagen and elastin. Because of that, vessel diameters as well as their variations during the cardiac cycle were considered as indices to characterize vessel pathologies. Hence, from a biomechanical perspective, it can be understood that to better appreciate the dynamics of the arterial wall and its pathologies, a more detailed description of the mechanical and elastic properties of the arteries is required.

Elasticity is a very suitable parameter to describe vessel wall function. It may be quantified with compliance, a measurement that expresses the relative change in vessel cross-sectional area as a function of time. However, a more complete method to outline the elastic properties of the vessel wall seems to be the elastography; indeed, such a technology aims to provide images of the elastic properties of biological soft tissues.

This paper investigated the feasibility of NIVE. It was shown that a major difficulty with this approach stems from the fact that motion occurs radially within

the vessel wall while the ultrasound beam propagates axially (linear array transducers were considered in the present study). Regarding that, a 2D tissue-motion estimator was required. Moreover, in such a situation, the motion parameters are expected to be very difficult to interpret. One major challenge with NIVE then concerns the interpretation of the motion estimates to appropriately characterize the vascular tissue.

ABOUT THE FORWARD PROBLEM

- 10 As a first step, the forward problem (FP) in NIVE was addressed. Biomechanical simulations of the vascular wall properties were performed and motion parameters were investigated. The FP allowed to better understanding vascular tissue dynamics in NIVE. Indeed, the analytical solution for a homogeneous vascular section subjected to an intraluminal pressure was derived. Ansys simulations were also performed to address the more complex situation of a heterogeneous plaque. Because tissue motion occurs radially within the vessel wall while the motion is assessed in (x,y)-Cartesian coordinates, the elastogram (Δ_{yy}) was shown to be subjected to hardening and softening artefacts.
- 20 To overcome the problems related to those mechanical artefacts, a new characterization parameter (ξ) was proposed. Such a parameter, also known in the literature as the Von Mises (VM) coefficient, uses the full 2D-strain tensor to provide a measure free from hardening and softening artefacts. ξ likely allows characterizing the vessel wall in its natural coordinate system. Indeed, such an elastogram presents some similarities with the radial strain map, and even shows up the very well known strain decay as it should be expected. For the case of the simulated pathological vessel, the VM parameter successfully allowed differentiating between hard, soft and normal vascular tissues. NIVE should then be considered, in some instances, as a promising tool for non-invasively
- 30 investigating vessel walls.

ABOUT THE APPLICATION OF THE LSME

A 2D-tissue motion estimator, known in the literature as the Lagrangian speckle estimator (LSME), was used to assess motion. The LSME is a 2D model-based estimator that allows computing the full 2D-strain tensor. The approach relies on a tissue-motion model and on a dynamic image-formation model. It assumes that the image formation can be modeled as a linear space-invariant operation on a scattering function. Indeed, the simulated RF images result from the 2D-convolution operation between the point-spread function of an ultrasound system and the acoustic impedance functions, which were modeled as a white Gaussian noise.

The same data sets as for the FP were investigated. As well, for the homogeneous and heterogeneous vessels, the results seemed promising. The Von Mises characterization parameter (ξ) showed great potential to differentiate hard and soft tissues from the normal vascular one. However, the main problem with the LSME remains the assessment of the lateral motion parameters. As a matter of fact, due to the relatively poor lateral resolution of RF images, the variance for those motion estimates is large. It is also important to emphasize that the 2D motion estimator, presented in this paper, assumes that motion occurs in plane strain condition. However in practice, because of blood pressure excitation, the vessel wall is also expected to be under distension stress. As a consequence to that, out-of-plane motion will occur in the dynamics between the pre- and the post-motion RF images; this is another factor that may increase the variance of motion estimates. To at least partially counteract out-of-plane motion, one could ensure that a small intraluminal pressure gradient is induced. This could be done using an ECG gating along with the ultrasound acquisition system. The "Lagrangian" filter was also shown to be effective to compensate for such a source of decorrelation noise.

Another potential issue to vascular elastography is that vessel walls are subjected to residual stresses. Indeed, it was demonstrated that the magnitudes of such residual stresses (equivalently residual strains) may be relatively significant. Accordingly, vascular elastograms are expected to be fully valid whenever residual strains are much smaller than strains as induced by the intraluminal pressure gradient. Provided that, in NIVE, elastograms compute maps of relative stiffness, and provided that tissue motion is assessed over small regions of interest where linearity is assumed, residual stresses may not have significant effects. Furthermore, another potential solution may consist in setting an optimal pressure gradient such as the tissue strains are much larger than potential residual strains, but are small enough to be in the limits of linear elasticity.

CONCLUSION

An approach to non-invasively characterize vessel walls, labeled as NIVE, has been introduced. Whereas endovascular elastography is invasive and its clinical application restricted to a complementary tool to assist IVUS echograms in pre-operative lesion assessments and to plan endovascular therapy, NIVE method may be of value to investigate vascular tissue properties of patients under medication, and for post-surgical follow-up. Additional to that, NIVE could be of interest to investigate small vessels where catheterization and IVUS echography is not possible. While the use of a balloon catheter is not required in NIVE, such an option can be useful if a more precise dilation increment is needed. In this case, however, the technique would be invasive. Regarding the forward problem, the Von Mises coefficient has been proposed as a new characterization parameter. Numerical simulations showed the potential of the VM parameter to differentiate between hard, soft and normal vascular tissues. The lateral resolution of current ultrasound systems is, however, a limitation to such an approach.

FIGURE CAPTIONS

Figure 20.- Simplified illustration of NIVE (non-invasive vascular elastography) acquisition system, showing that the tissue motion occurs radially, whereas the linear-array transducer scans in the Cartesian coordinate system. Processing motion estimation requires 2D segmentation of the images; the W_{mn} represent the data windows that are used by the Lagrangian speckle model estimator.

10 **Figure 21.-** Schematic implementation of the dynamic image-formation model. For this example, the displacement field was computed from the analytical solution for a pressurized thick-wall cylindrical blood vessel embedded in an elastic coaxial cylindrical medium (Appendix I). The parameters on this figure refer to Eq. 5. The dynamic image-formation model was also applied to the case of the heterogeneous vessel. In this case, the displacement field was determined with Ansys simulations.

20 **Figure 22.-** Block-diagram showing the implementation of the Lagrangian speckle motion model estimator (Eq. 6). The algorithm searches the tissue motion vector ψ that best matches I_0 and I_1 . ψ_0 is the initial guess that is required to start the iterative process. In this study, a 2 % axial compression was assumed for the initial guess.

Figure 23.- Illustration of the difference between the observer's (x,y) and the material (r, ϕ) coordinate systems. The latter, also known as the Lagrangian coordinate system, considers each portion of a continuum as if it were a particle, for which the trajectory is described as a function of time.

30 **Figure 24.-** Motion parameters for a pressurized thick-wall cylindrical blood vessel, embedded in an elastic infinite medium. Figs 24a and 24b present respectively the lateral and axial displacement fields; the colorbars express the displacements in μm . Figs 24c to 24f show the Δ_{ij} components of Eq. 3, which are respectively the

lateral strain (Δ_{xx}), the lateral shear (Δ_{xy}), the axial shear (Δ_{yx}) and the axial strain (Δ_{yy}); the colorbars express the strain in percent.

Figure 25.- Radial strain, and strain decay for a homogeneous vessel wall. a) Radial displacement computed from the lateral and axial displacement fields; b) radial displacement field in a polar (r, ϕ) coordinate system; c) radial strain computed from the gradient of 25b; d) radial strain at $\phi = \pi$ showing the strain decay; e) radial strain reported back in the (x, y)-coordinate system.

- 10 **Figure 26.-** Comparison between the radial strain and the Von Mises parameter (ξ) for a homogeneous vessel wall. a) Radial strain in the (x, y)-coordinate system; b) Map of ξ ; c) curves from the radial strain (—) and ξ (---) at $x = 0$.

Figure 27.- Motion parameters for an heterogeneous vessel wall. a) Simplified representation of the geometry; b) to e) show the Δ_{ij} components of Eq. 3, which are respectively the lateral strain (Δ_{xx}), the lateral shear (Δ_{xy}), the axial shear (Δ_{yx}), and the axial strain (Δ_{yy}); they were computed from the gradients of the lateral and axial displacement fields. The colorbars express the strain in percent.

- 20 **Figure 28.-** Comparison between the radial strain and the Von Mises parameter (ξ). a) Map of the (x, y)-radial strain; b) map of ξ ; c) curves of a) (—) and b) (---) at $x = 0$.

Figure 29.- Motion parameters as computed with the Lagrangian speckle model estimator for a homogenous vessel wall; a) to d) Δ_{ij} components of Eq. 3, which are respectively the lateral strain (Δ_{xx}), the lateral shear (Δ_{xy}), the axial shear (Δ_{yx}), and the axial strain (Δ_{yy}).

- 30 **Figure 10.-** Comparison between simulated and theoretical Von Mises parameters (ξ) for a homogeneous vessel wall. a) Map of the simulated ξ ; b) curve of the

simulated ξ at $x = 0$; c) map of the theoretical ξ ; d) curve of the theoretical ξ at $x = 0$.

Figure 11.- Motion parameters as estimated with the Lagrangian speckle model estimator for an heterogeneous vessel wall; a) to d) Δ_{ij} components of Eq. 3, which are respectively the lateral strain (Δ_{xx}), the lateral shear (Δ_{xy}), the axial shear (Δ_{yx}), and the axial strain (Δ_{yy}).

10 **Figure 12.-** Comparison between simulated and theoretical Von Mises parameters (ξ) for an heterogeneous vessel wall. a) Map of the simulated ξ ; b) curve of the simulated ξ at $x = 0$; c) map of the theoretical ξ ; d) curve of the theoretical ξ at $x = 0$.

APPENDIX I

Thick-wall cylindrical blood vessel embedded in a finite (or infinite) medium

An exact solution of a pressurized thick-wall cylindrical blood vessel of inner and outer radii R_i and R_o respectively, embedded in an elastic coaxial cylindrical medium of radius R_e , can be found in linear elasticity. For the mathematical formulation, the cylindrical and Cartesian unit base vectors and their associated physical coordinates are noted $(\bar{e}_r, \bar{e}_\phi, \bar{e}_z)$, $(\bar{e}_x, \bar{e}_y, \bar{e}_z)$ and (r, ϕ, z) , (x, y, z) , respectively. In this mechanical problem, the Cartesian vessel wall displacement field and strain components are of interest. The assumption of plane strain was made (in the (r, ϕ) -plane) because the vessel length is at least of the same order of magnitude as its radial dimension.

The two elastic media are assumed to be incompressible and isotropic and are described by the constitutive laws:

$$[\sigma]^{(m)} = -p^{(m)}[I] + \frac{2}{3}E^{(m)}[\varepsilon]^{(m)} \quad (\text{A.1})$$

where the superscript 'm' denotes the considered medium ($m=1$ for the vascular wall for which $R_i \leq r \leq R_o$ and $0 \leq \phi \leq 2\pi$, and $m=2$ for the embedded tissue for which $R_o \leq r \leq R_e$ and $0 \leq \phi \leq 2\pi$). The parameters $[\sigma]^{(m)}$ and $[\varepsilon]^{(m)}$ are the stress and strain tensors, $[I]$ is the identity matrix, $E^{(m)}$ are the Young's moduli, and $p^{(m)}$ are the Lagrangian multipliers resulting from the incompressibility of the materials [38] given by the following kinematics constraints:

$$\nabla \cdot \tilde{u}^{(m)} = 0 \quad (\text{A.2})$$

where $\vec{u}^{(m)}$ are unknown displacement vectors. If gravity and inertial forces are neglected, the conditions of local equilibrium are $\nabla \cdot [\sigma]^{(m)} = \vec{0}$, or in terms of the displacement vectors:

$$\nabla p^{(m)} = \frac{E^{(m)}}{3} \nabla^2 \vec{u}^{(m)} \quad (\text{A.3})$$

The displacement fields $\vec{u}^{(m)}$ as well as the stress tensors $[\sigma]^{(m)}$ must satisfy the following boundary conditions. The blood pressure P_b is uniform,

$$10 \quad [\sigma]^{(1)} \vec{e}_r = -P_b \vec{e}_r \quad \text{at} \quad r = R_i \quad (\text{A.4})$$

no stresses are applied on the external surface of the surrounded tissue,

$$[\sigma]^{(2)} \vec{e}_r = \vec{0} \quad \text{at} \quad r = R_e \quad (\text{A.5})$$

and at the interface between the vessel wall and the surrounded tissue, we must have the continuity of displacement fields and equality of the stress vectors,

$$\vec{u}^{(1)} = \vec{u}^{(2)} \quad \text{at} \quad r = R_o \quad (\text{A.6})$$

$$20 \quad [\sigma]^{(1)} \vec{e}_r = [\sigma]^{(2)} \vec{e}_r \quad \text{at} \quad r = R_o \quad (\text{A.7})$$

Due to the symmetry of the mechanical problem and because the two media are incompressible, the displacement solutions are:

$$\vec{u}^{(1)}(r) = \vec{u}^{(2)}(r) = \frac{K}{r} \vec{e}_r \quad (\text{A.8})$$

where K is a constant. The equilibrium conditions (Eq. A.3) are satisfied only if the two Lagrangian terms $p^{(1)}$ and $p^{(2)}$ are constant. At the end, the three unknowns of the problem (K , $p^{(1)}$, $p^{(2)}$) are found by using the boundary conditions given by Eqs. (A.4), (A.5) and (A.7). Hence, for the value of K , we have:

$$K = \frac{3}{2} P_b \left[E^{(1)} \left(\frac{1}{R_i^2} - \frac{1}{R_o^2} \right) - E^{(2)} \left(\frac{1}{R_o^2} - \frac{1}{R_o^2} \right) \right]^{-1} \quad (\text{A.9})$$

In the particular case of a thick-wall cylindrical blood vessel embedded in an infinite medium, the new value of K is obtained from the limit $K_\infty = \lim_{R_o \rightarrow \infty} K$, and is

10 given by:

$$K_\infty = \frac{3}{2} P_b \left[E^{(1)} \left(\frac{1}{R_i^2} - \frac{1}{R_o^2} \right) + \frac{E^{(2)}}{R_o^2} \right]^{-1} \quad (\text{A.10})$$

So, the needed Cartesian components of the displacement vectors and strain tensors are:

$$u_x(x, y) = K_\infty \frac{x}{x^2 + y^2} \quad (\text{A.11})$$

$$u_y(x, y) = K_\infty \frac{y}{x^2 + y^2} \quad (\text{A.12})$$

$$\varepsilon_{xx}(x, y) = \frac{\partial u_x}{\partial x} = K_\infty \frac{y^2 - x^2}{(x^2 + y^2)^2} \quad (\text{A.13})$$

$$\varepsilon_{yy}(x, y) = \frac{\partial u_y}{\partial y} = K_\infty \frac{x^2 - y^2}{(x^2 + y^2)^2} \quad (\text{A.14})$$

$$\varepsilon_{xy}(x, y) = \frac{1}{2} \left(\frac{\partial u_x}{\partial y} + \frac{\partial u_y}{\partial x} \right) = -2K_\infty \frac{xy}{(x^2 + y^2)^2} \quad (\text{A.15})$$

FOOTNOTES

¹ This is the Matlab notation for augmented vector (;) and matrix vectorisation (:). Hence, ψ is a 6×1 vector built from the 2×1 Tr vector and the 4×1 vectorisation of LT.

² Notice that 6 % intraluminal dilation is equivalent to 3 % compression of the intraluminal wall.

CLAIMS

1. A method for characterising the mechanical properties of tissues in small vessels using the Non-Invasive Ultrasound Elastography (NIVE), the method comprising the steps of :

acquiring pre- and post- deformation images;

using the Lagrangian speckle tissue model estimator to assess the 2-D strain tensor;

computing the Von Mises elastograms; and

10 modelising the tissue mechanical characteristics.

2. An apparatus for investigating the feasibility of NIVE for characterising tissues in small vessels.

3. A model-based method devoted to endovascular elastography, the method comprising the steps of :

performing a modeling in performing the sub-steps of :

A1) modeling the polar static-image formation;

A2) modeling the tissue-motion;

20 A3) modeling the polar dynamic-image-formation;

estimating tissue motion in performing the sub-steps of :

B1) assuming speckle is a material property;

B2) providing LSI (Lagrangian speckle images);

B3) using the Lagrangian Speckle Model Estimator (LSME) to assess tissue motion;

B4) solving a non linear minimization problem;

B5) using the optical flow equations;

thereby providing an accurate tissue motion estimate for providing an elastogram of the tissue.

4. An apparatus for characterising the mechanical properties of tissues, the apparatus comprising :

a CVIS ultrasound scanner;

a 30-40 MHz mechanical rotating single element transducer;

an oscilloscope;

a pressuring system; and

a computer.

10 5. A method for detecting the hard plaque in the blood vessels, the method comprising the steps of :

collecting a sequence of RF images while incrementally adjusting the intraluminal static pressure;and

characterising the the hard plaque from the normal vascular tissue.

6. An apparatus for detecting the hard plaque in the blood vessels, the apparatus comprising :

a CVIS ultrasound scanner;

a 30 MHz mechanical rotating single element transducer;

an oscilloscope;

20 a pressuring system; and

a computer.

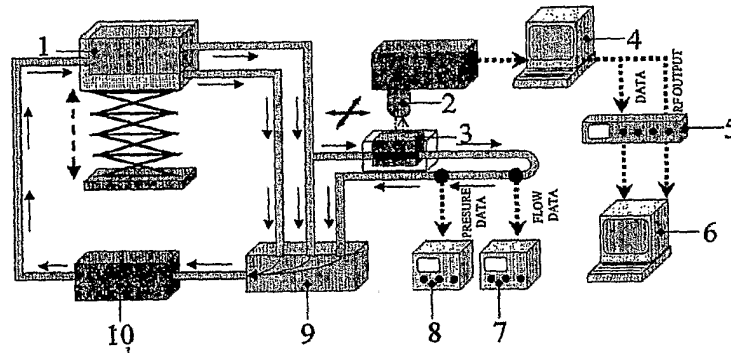


Fig. 1) Schematic description of the experimental set-up.

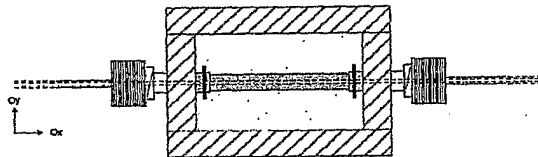


Fig. 2) Schematic illustration of the vascular flow phantom.

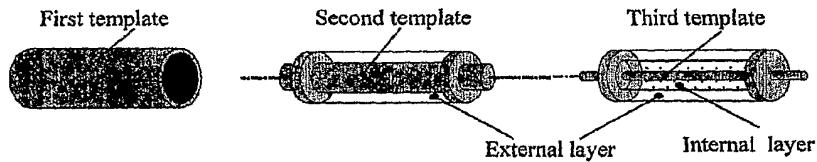


Fig. 3) Schematic representation of the moulds that were used to manufacture the double-layer PVA-C vessel-mimicking phantom. The simulated vessel had a 1.5-mm lumen diameter, 1.5-mm wall thickness (approximately 0.75-mm for each layer), and 52-mm length.

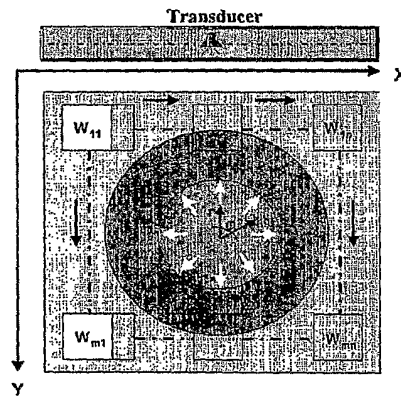


Fig. 4) Simplified illustration of NIVE acquisition system, showing that the tissue motion occurs radially, whereas the transducer scans in the Cartesian coordinate system. The approach assumes a constant deformation for each W_{mn} .

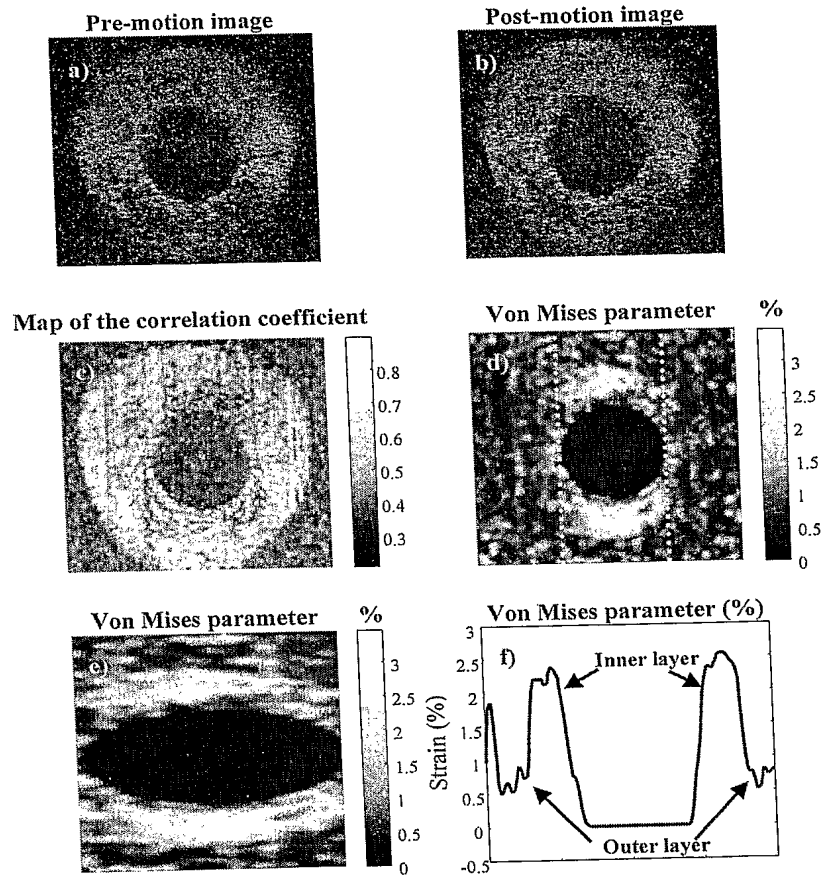


Fig. 5) a) and b) show pre- and post-motion B-mode images (RF images were processed to achieve tissue motion); c) presents a map of the correlation coefficient between the pre- and post-motion RF images; d) shows the composite elastogram (ξ) as computed by the LSME (the color bar indicates the strain in %); e) presents a zoomed axial portion of d, showing the inner layer (softer) with higher strain values, and the outer layer (harder) with lower strain values; f) plot of an average of 20 axial lines chosen in the middle of ξ .

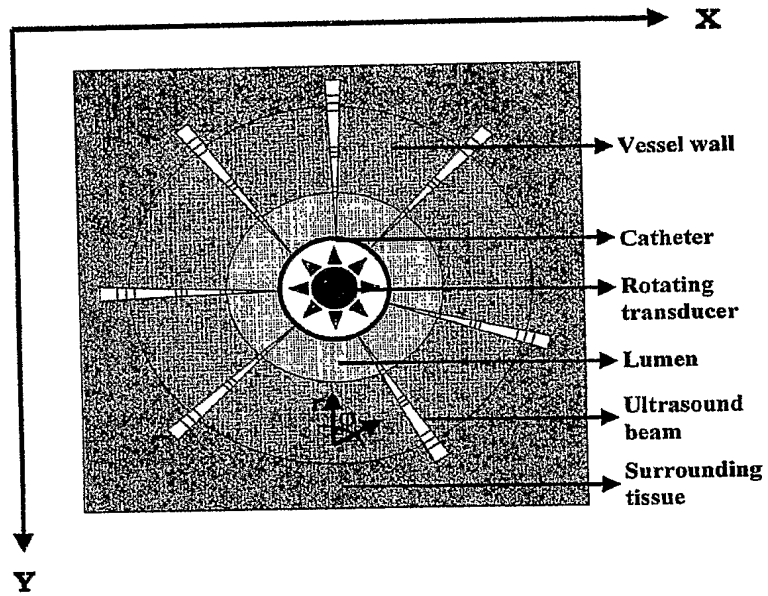


FIG. 6

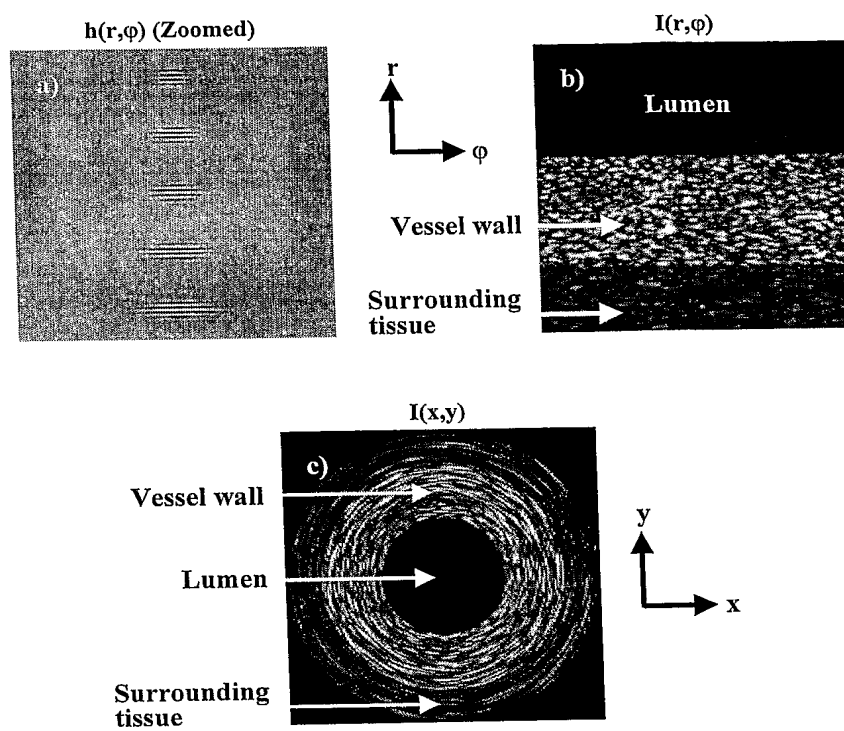


FIG. 7

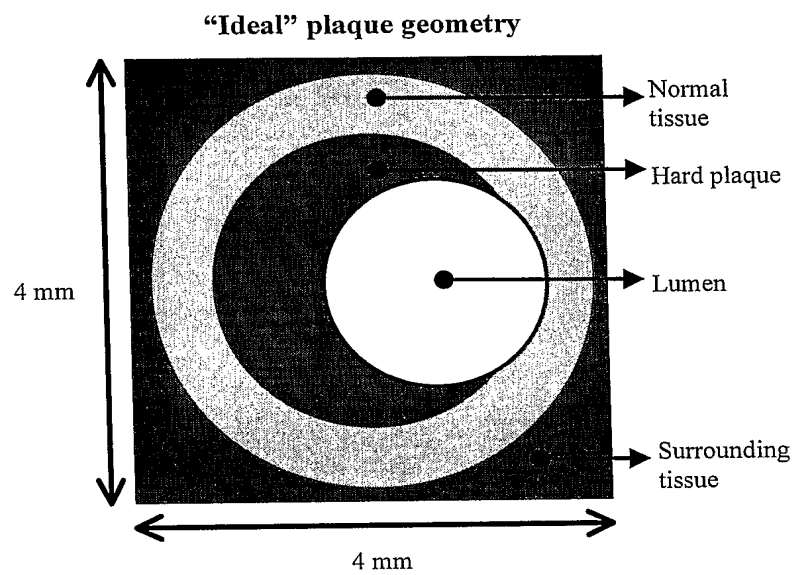


FIG. 8

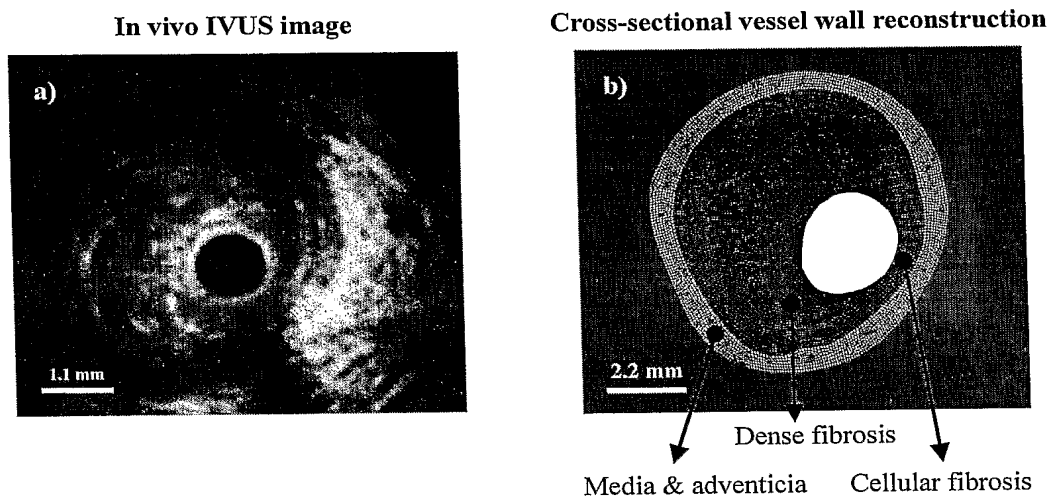


FIG. 9

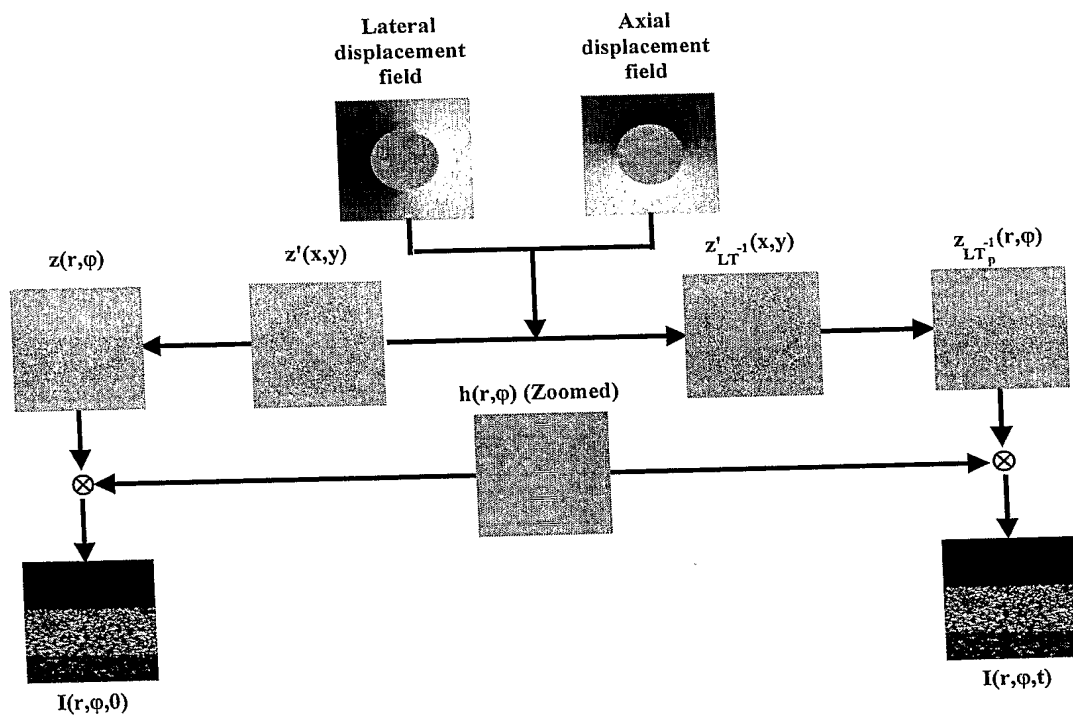


FIG. 10

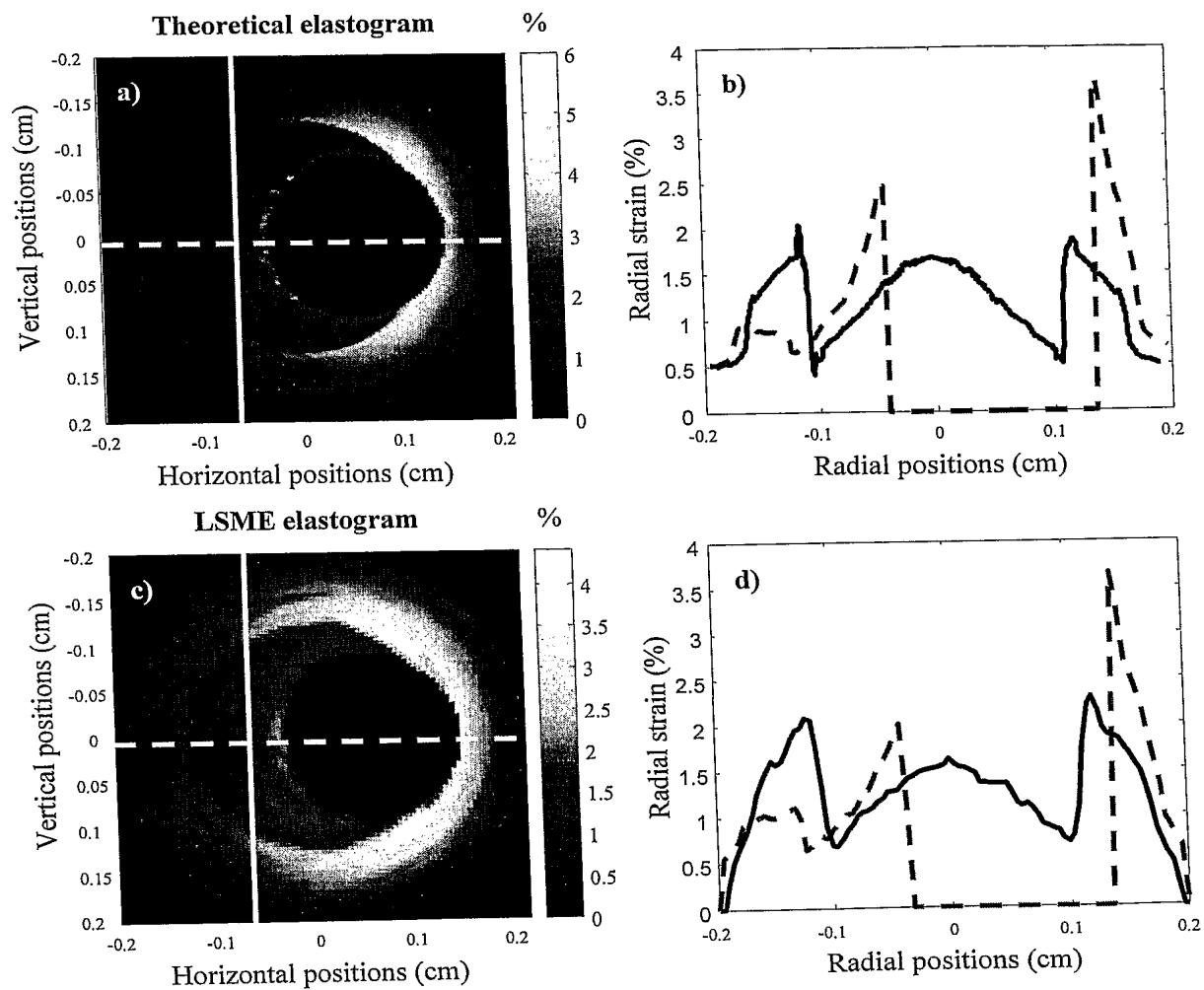


FIG. 11

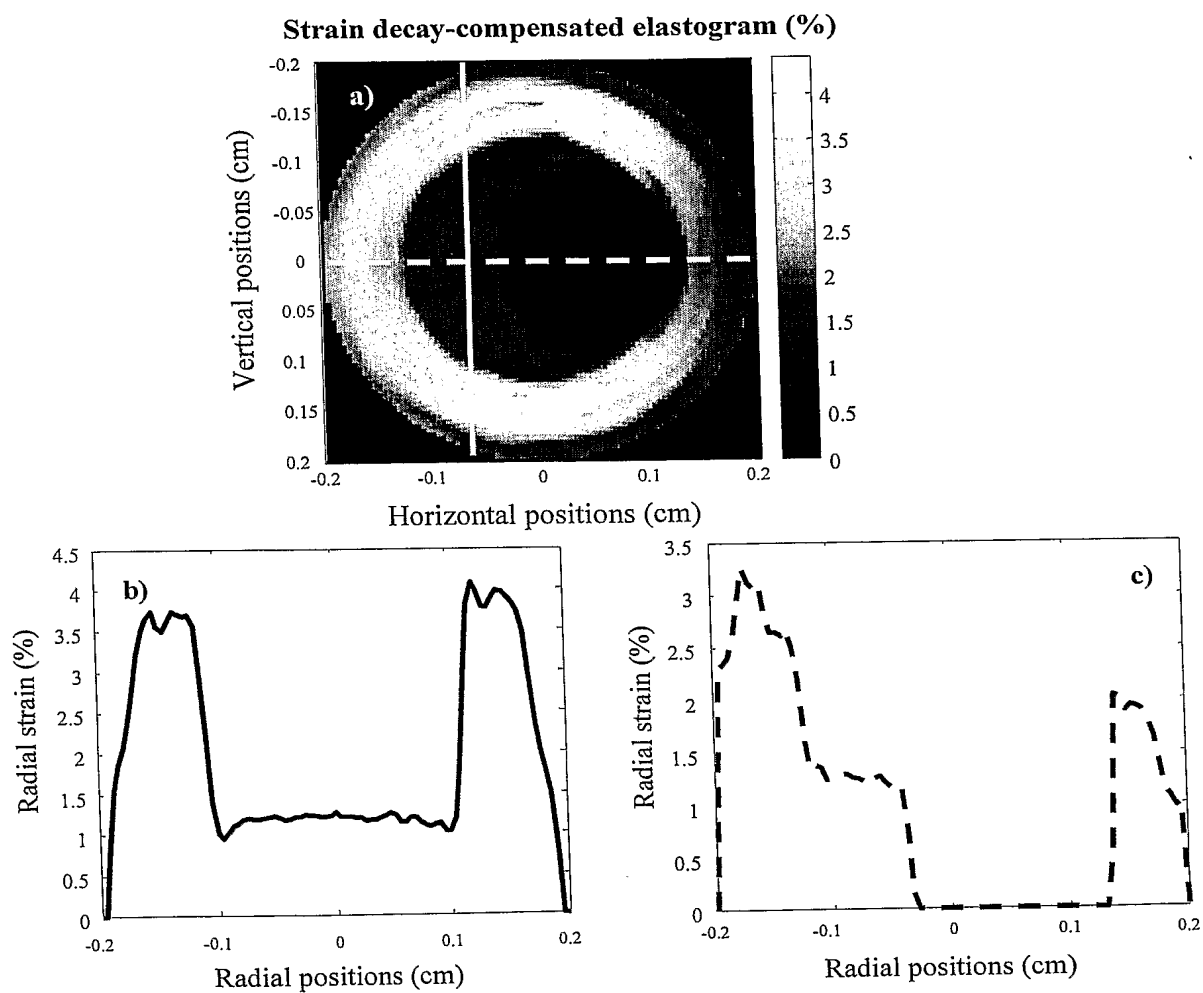


FIG. 12

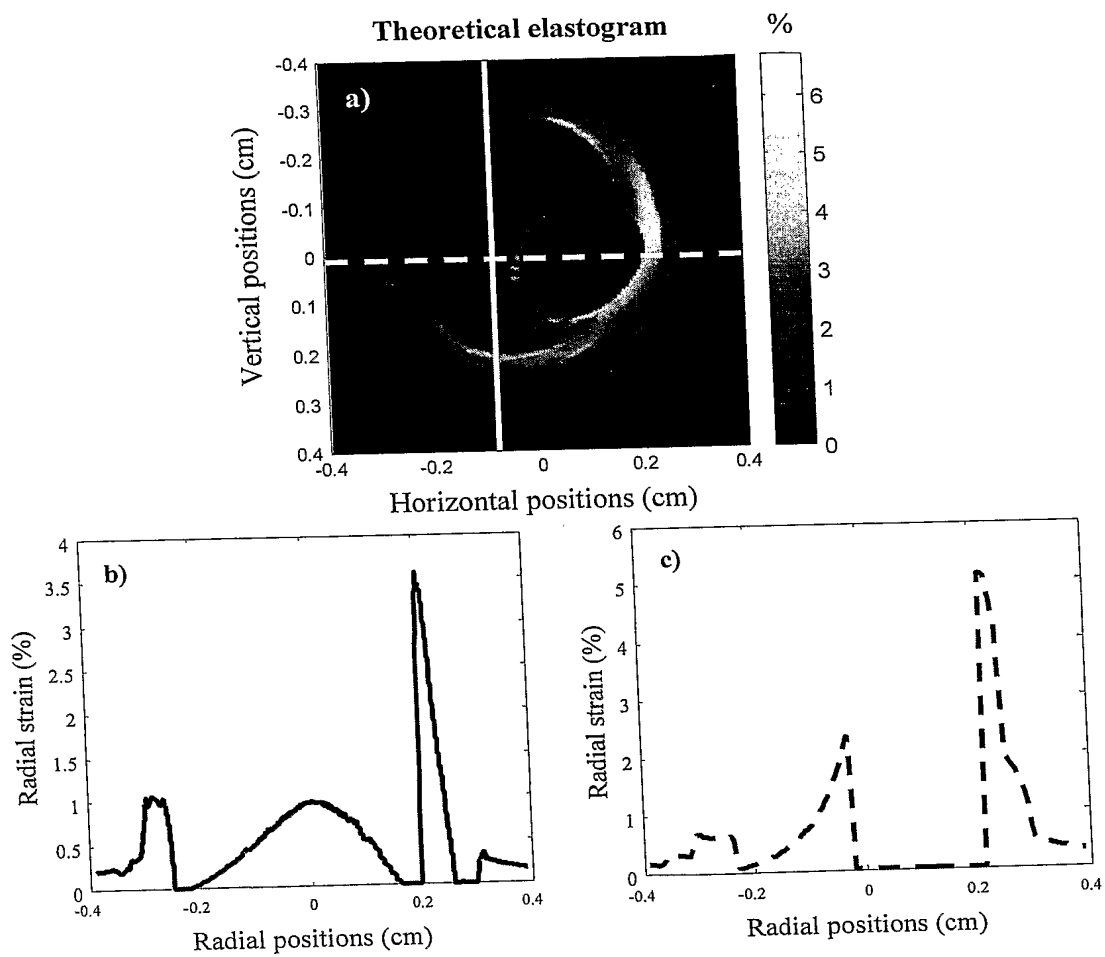


FIG. 13

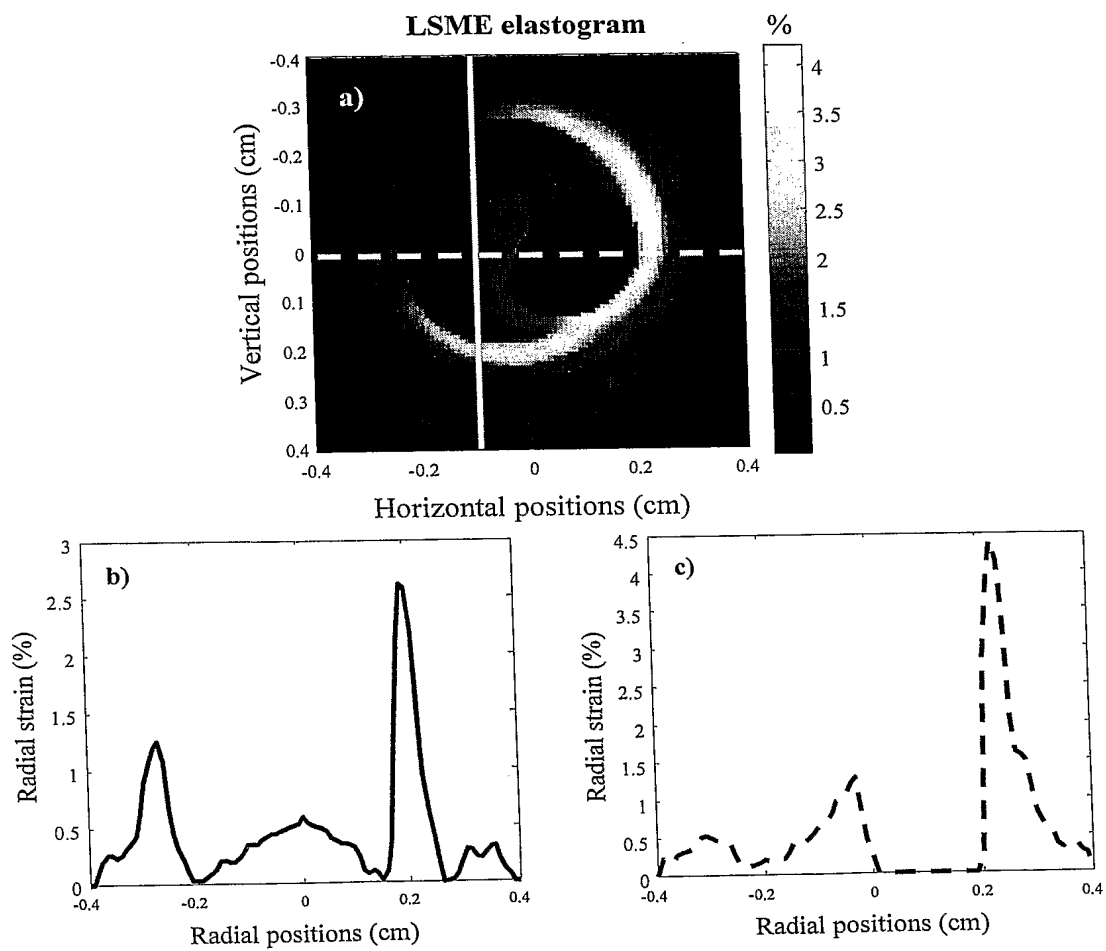


FIG. 14

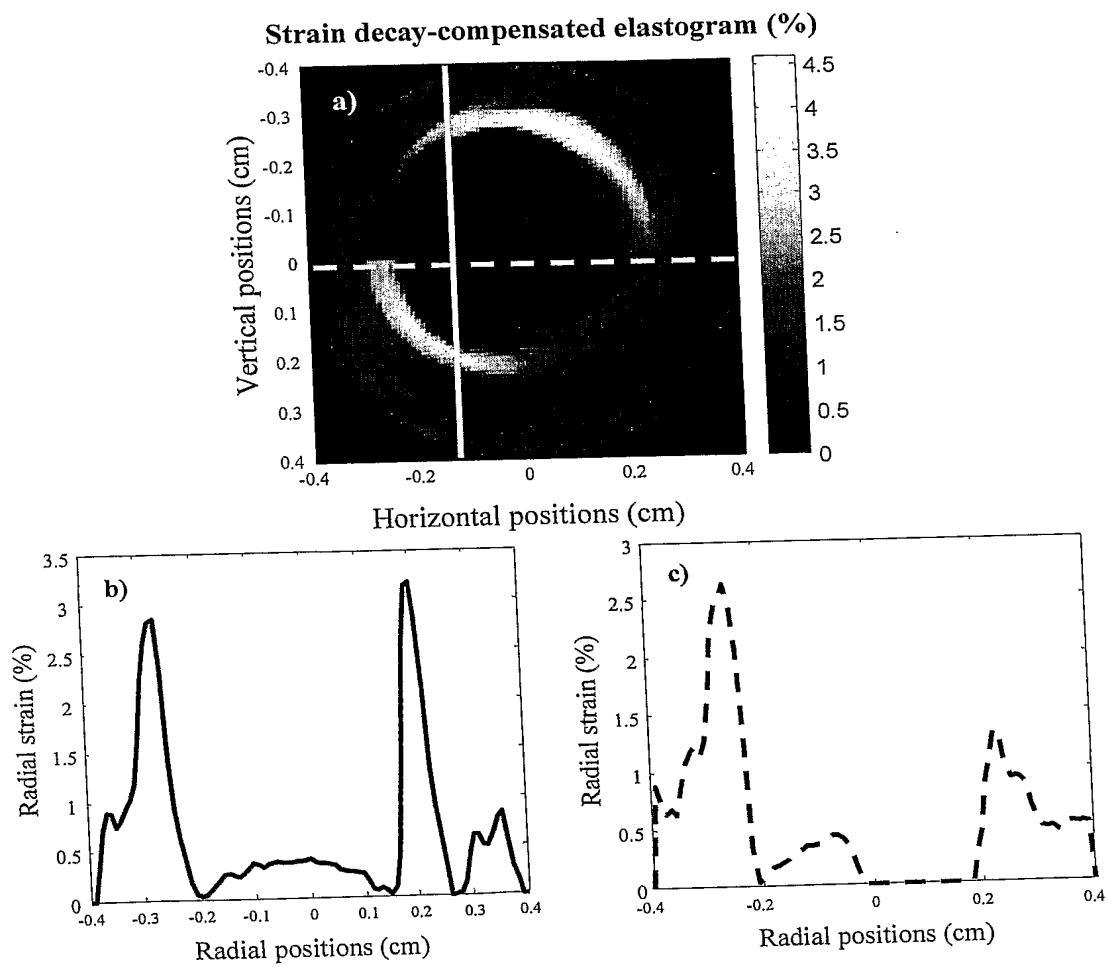


FIG. 15

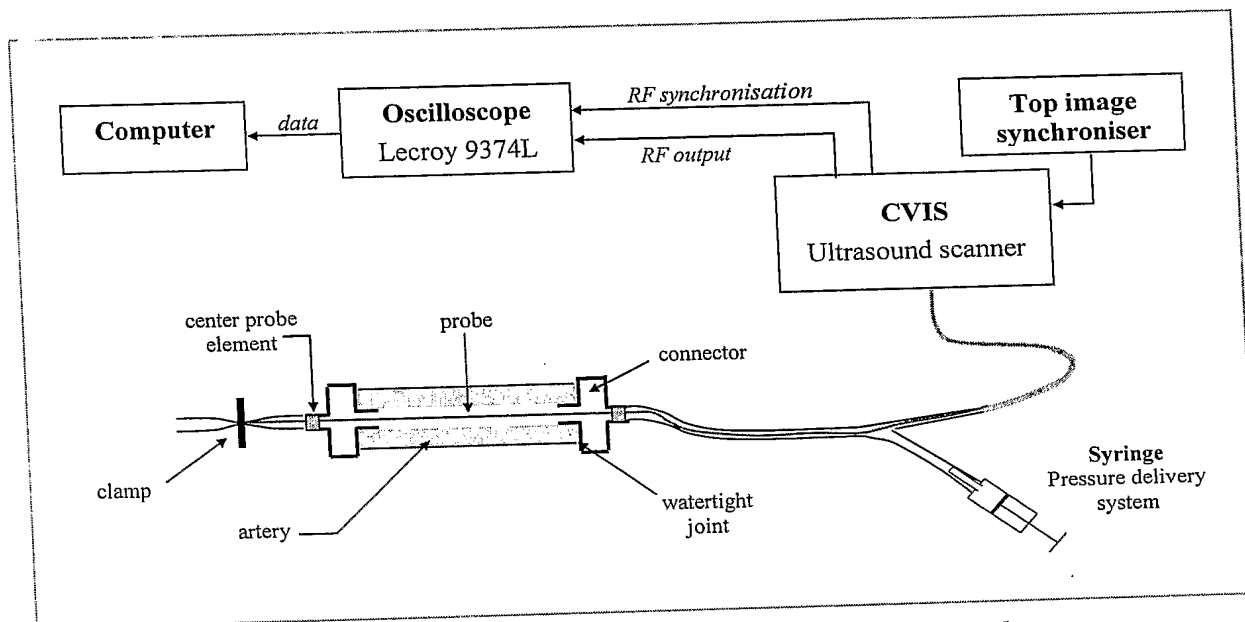


Fig. 16) Experimental set-up for intravascular elastographic investigations.

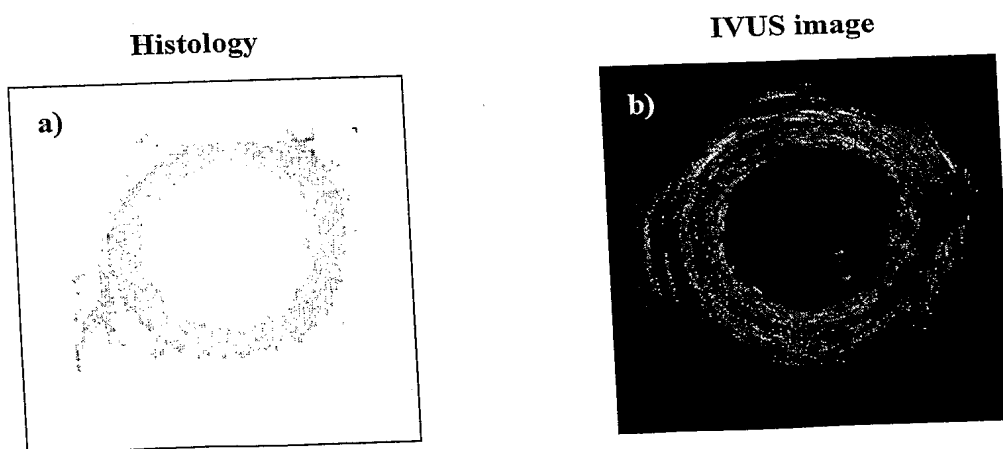
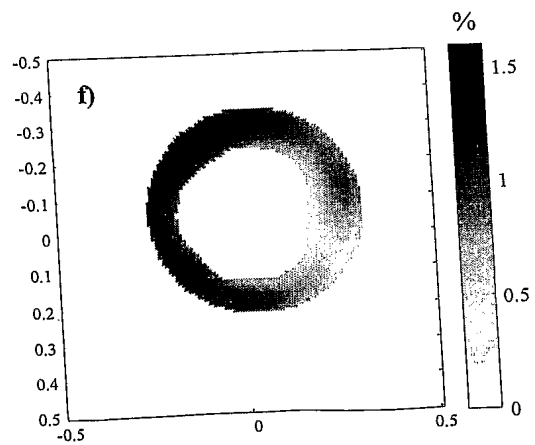
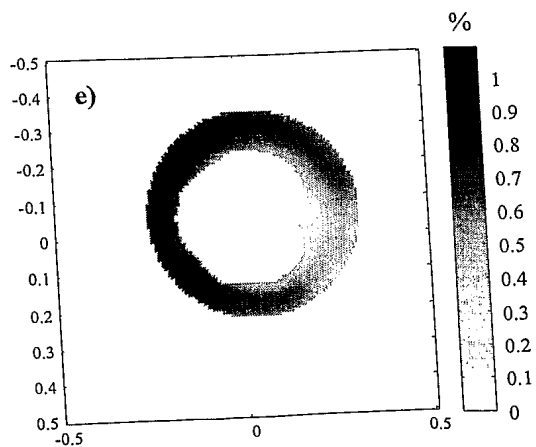
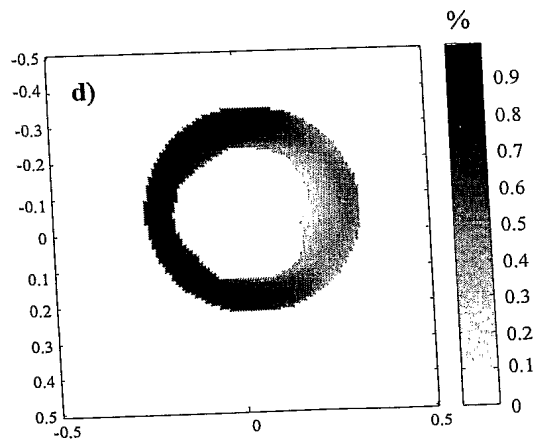
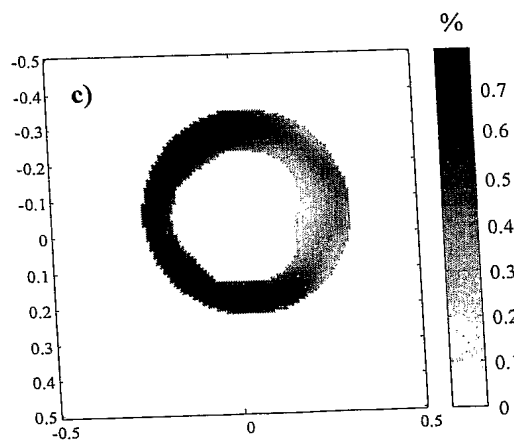
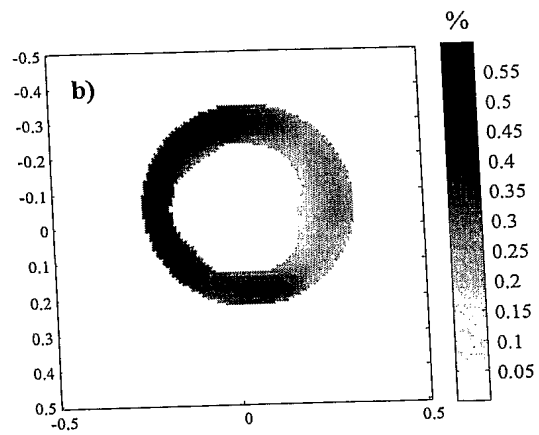
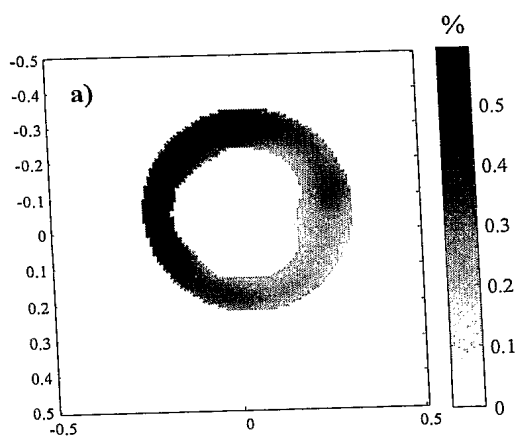


Fig. 17) a) Histological section, showing a very small atherosclerotic plaque at 3 o'clock; b) IVUS image. Notice that the IVUS image does not allow to clearly differentiate the plaque from the healthy vascular tissue.



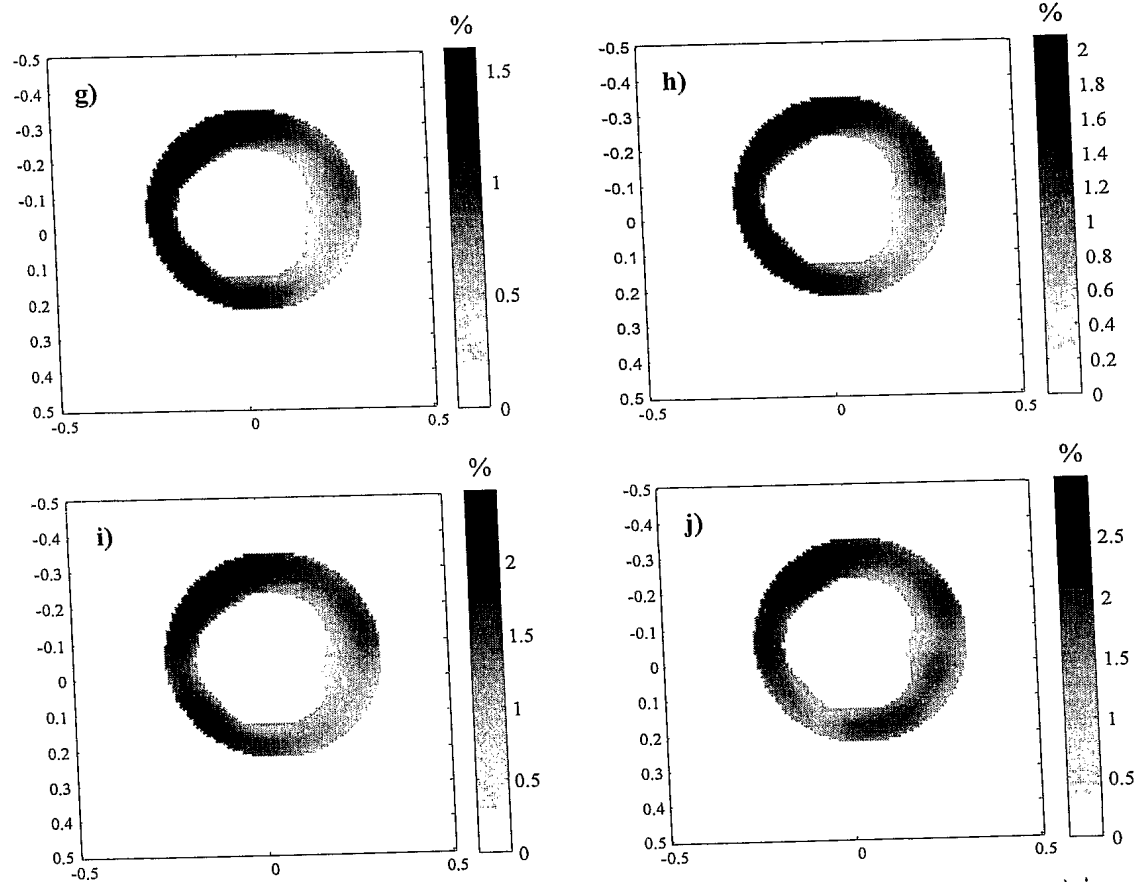


Fig. 18)- a) to j) are elastograms computed for consecutive increasing physiologic fluid pressure levels. Lateral and axial values are dimensions, while the colorbars give the strain in percent.

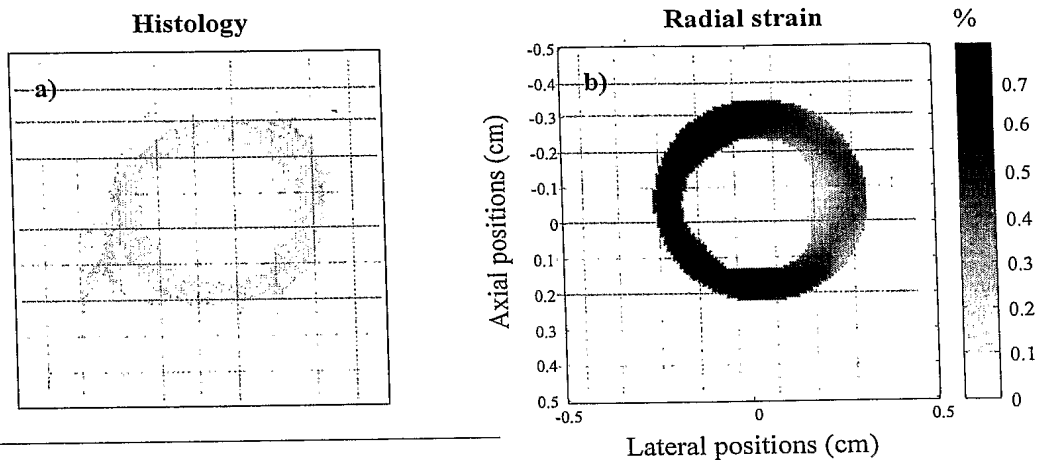


Fig. 19)- a) Histological section, showing a very small atherosclerotic plaque at 3 o'clock; b) Elastogram, showing very significant qualitative and quantitative similarities with histology.

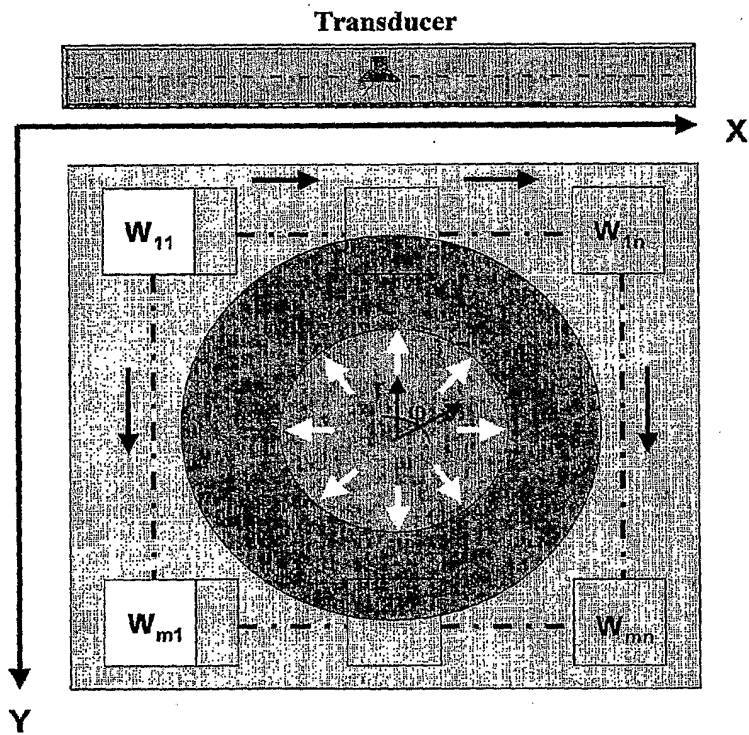


Figure 20

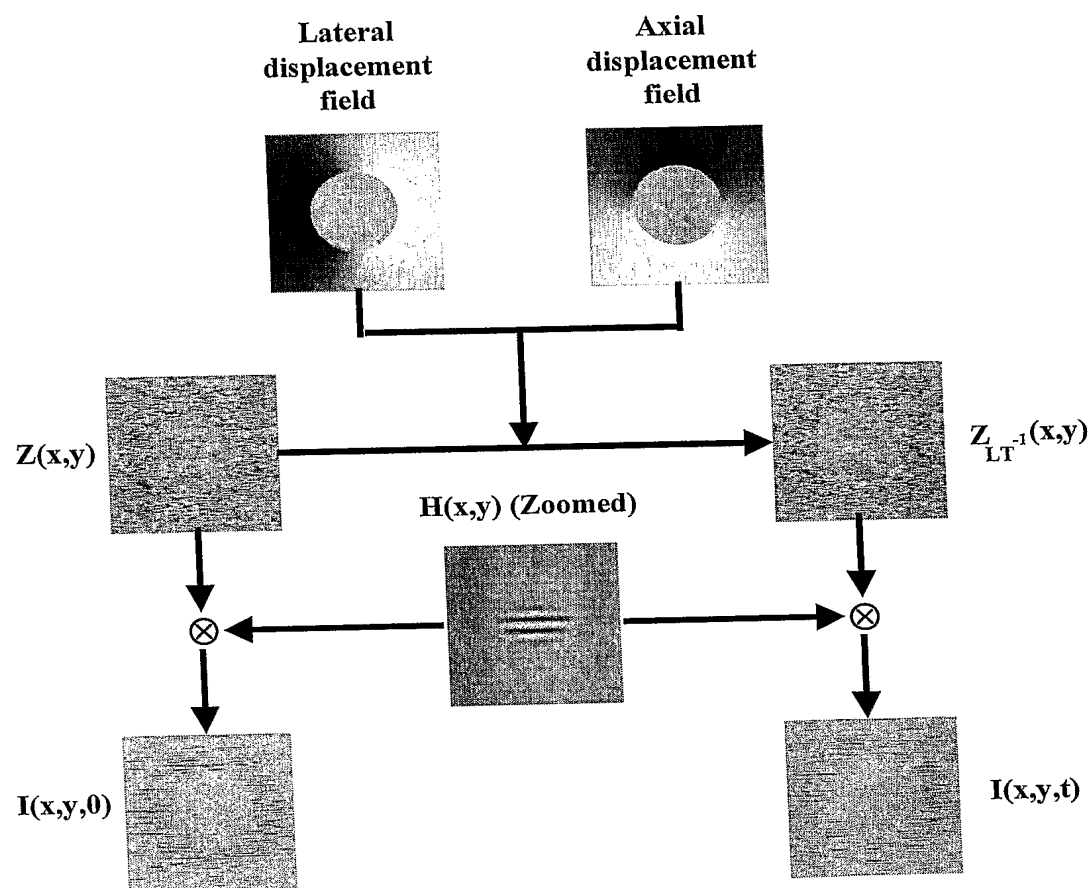


Figure 21

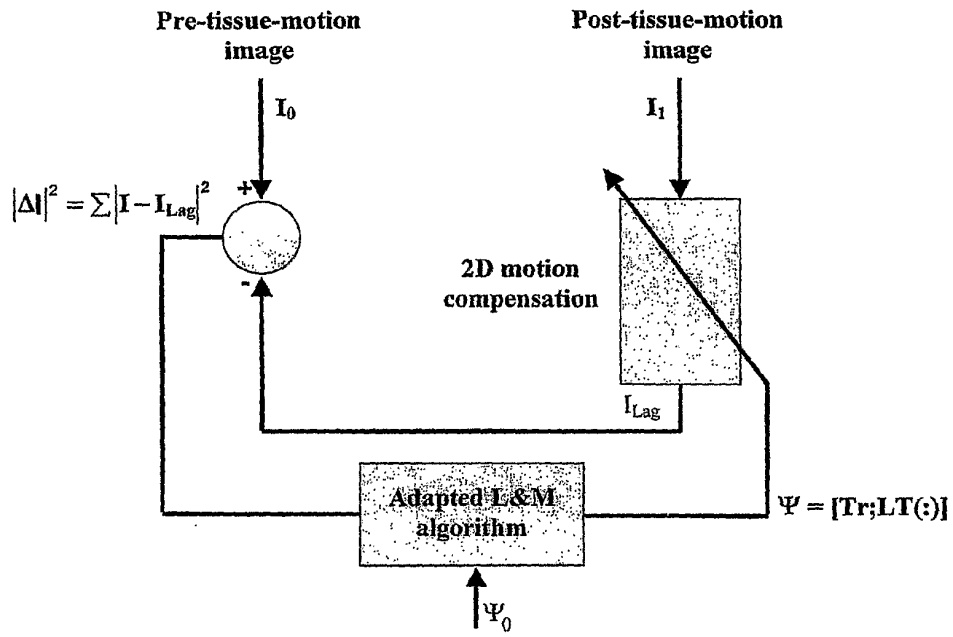


Figure 22

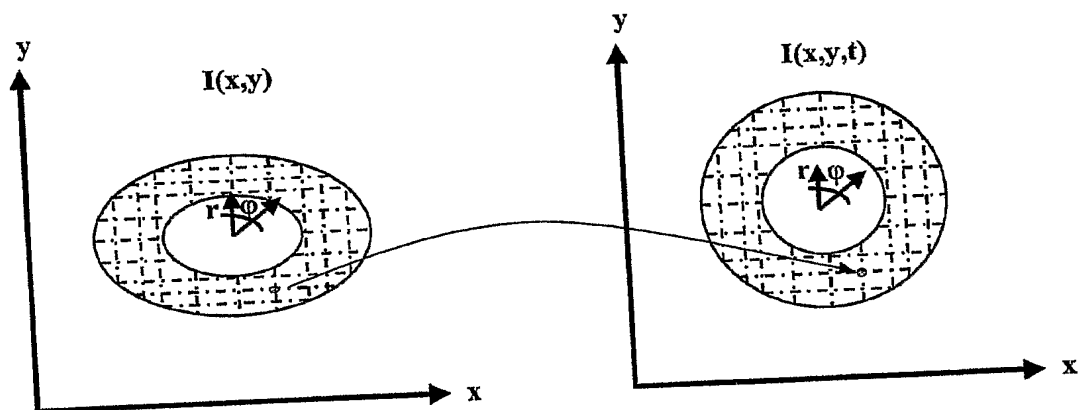


Figure 23

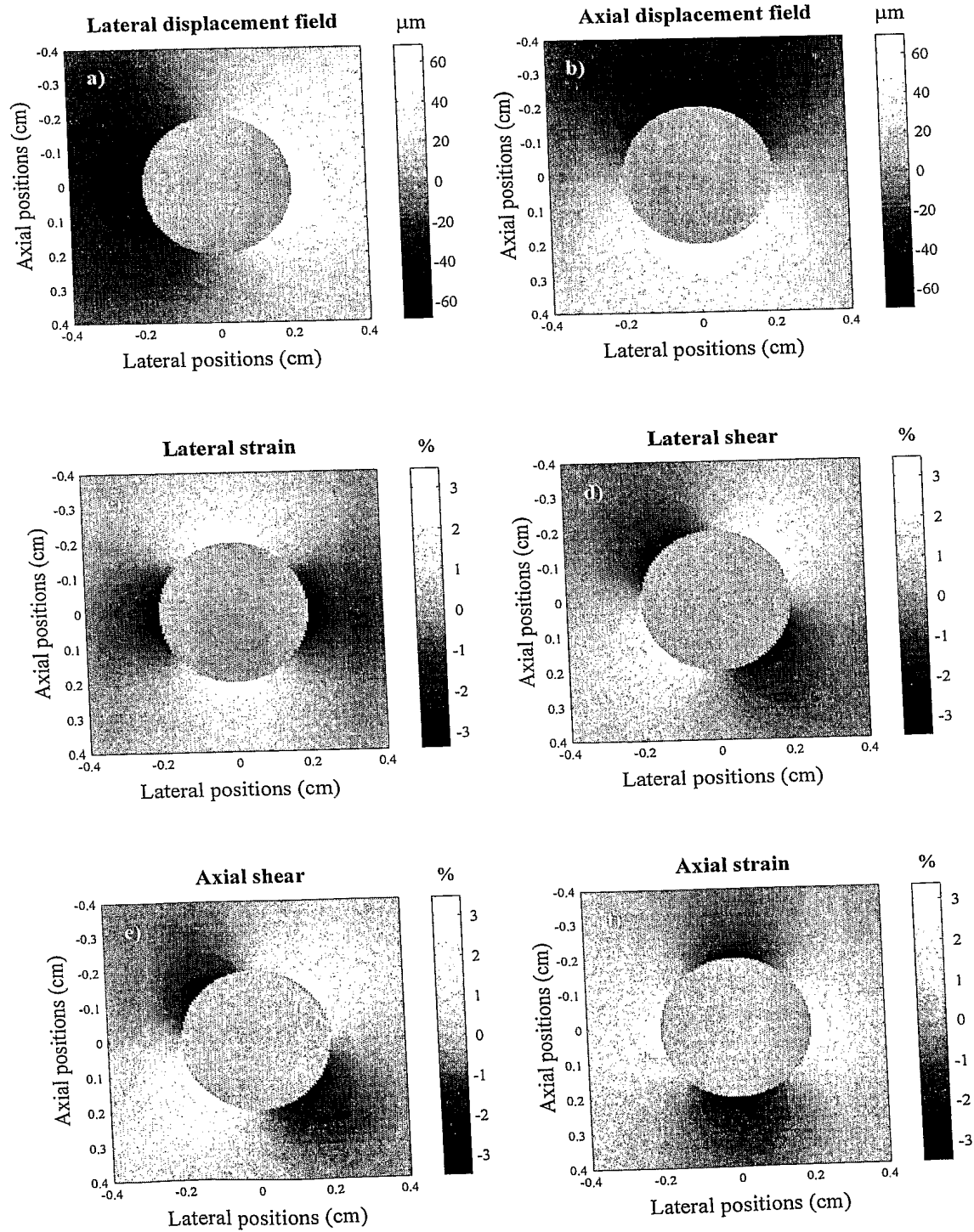


Figure 24

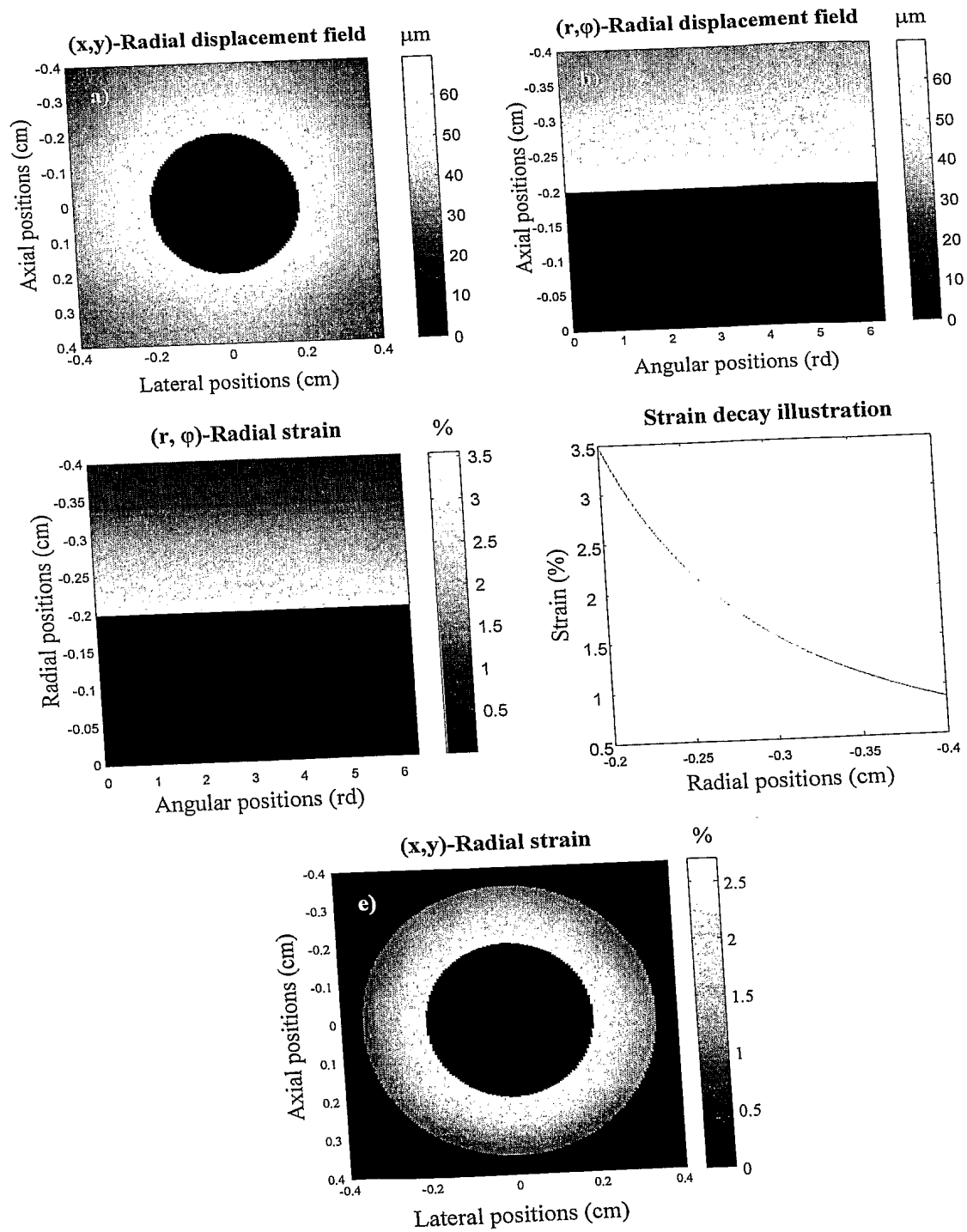


Figure 25

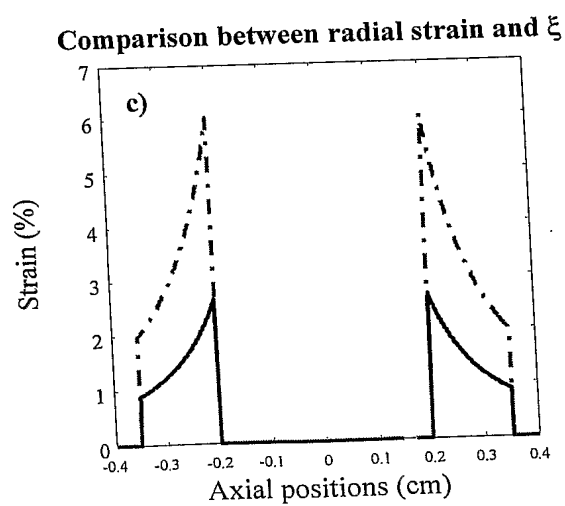
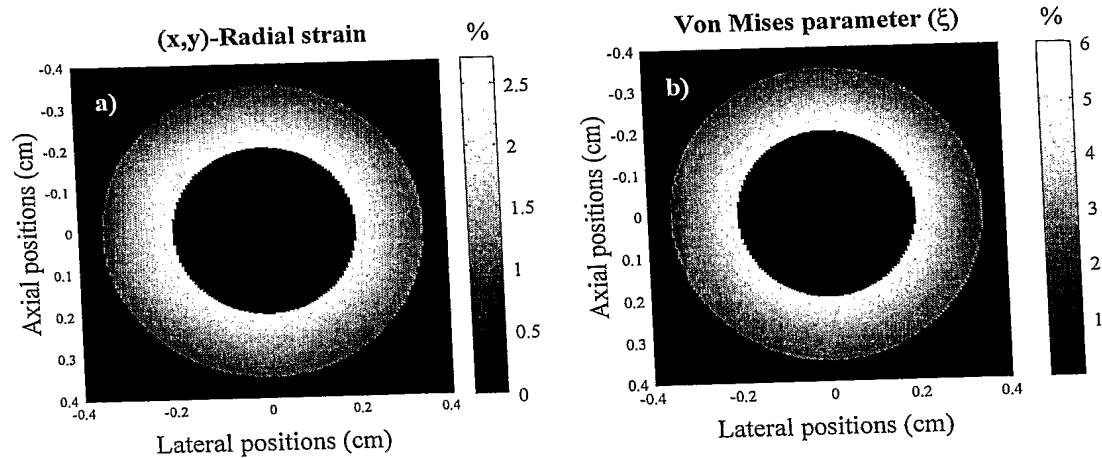


Figure 26

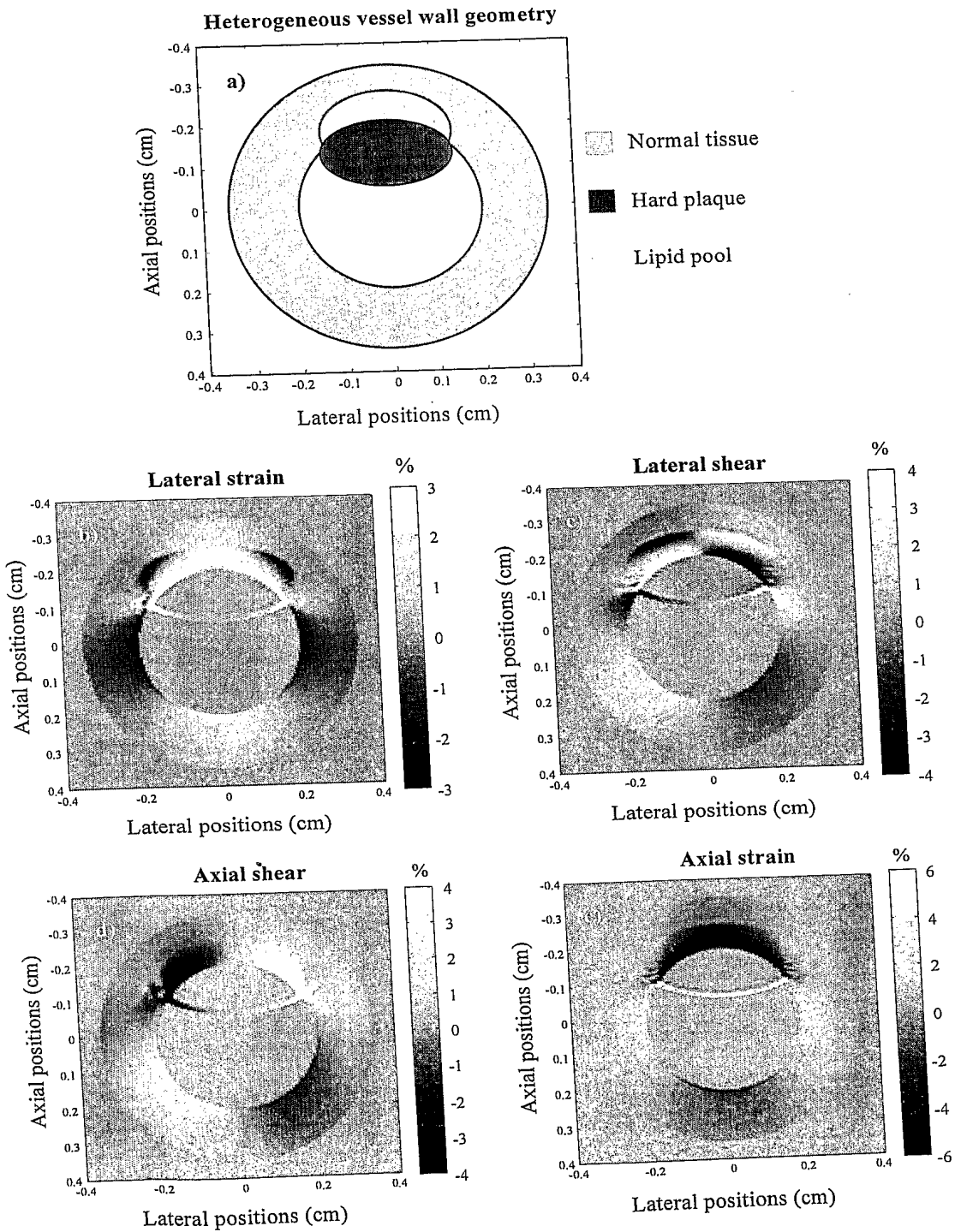


Figure 27

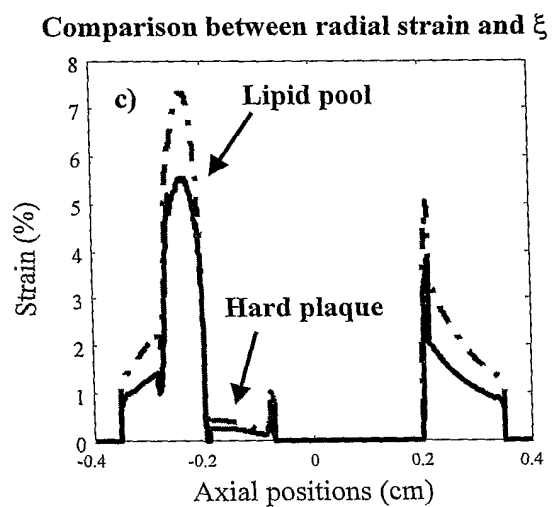
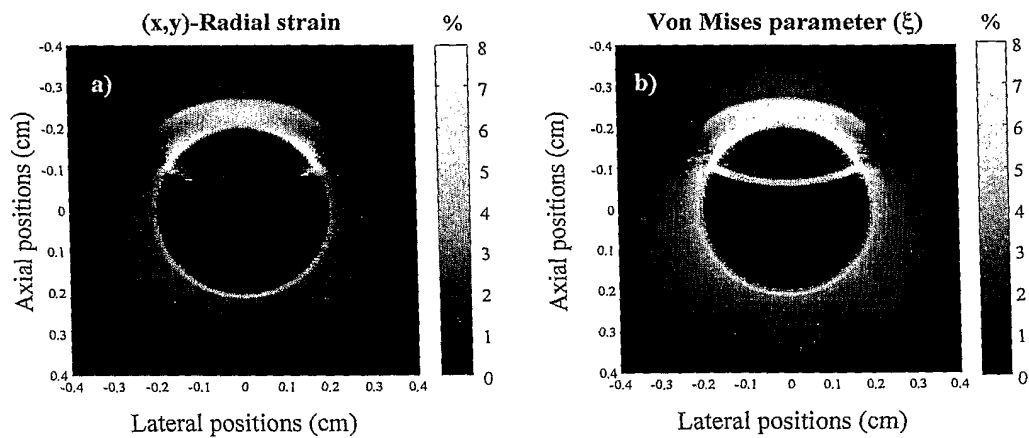


Figure 28

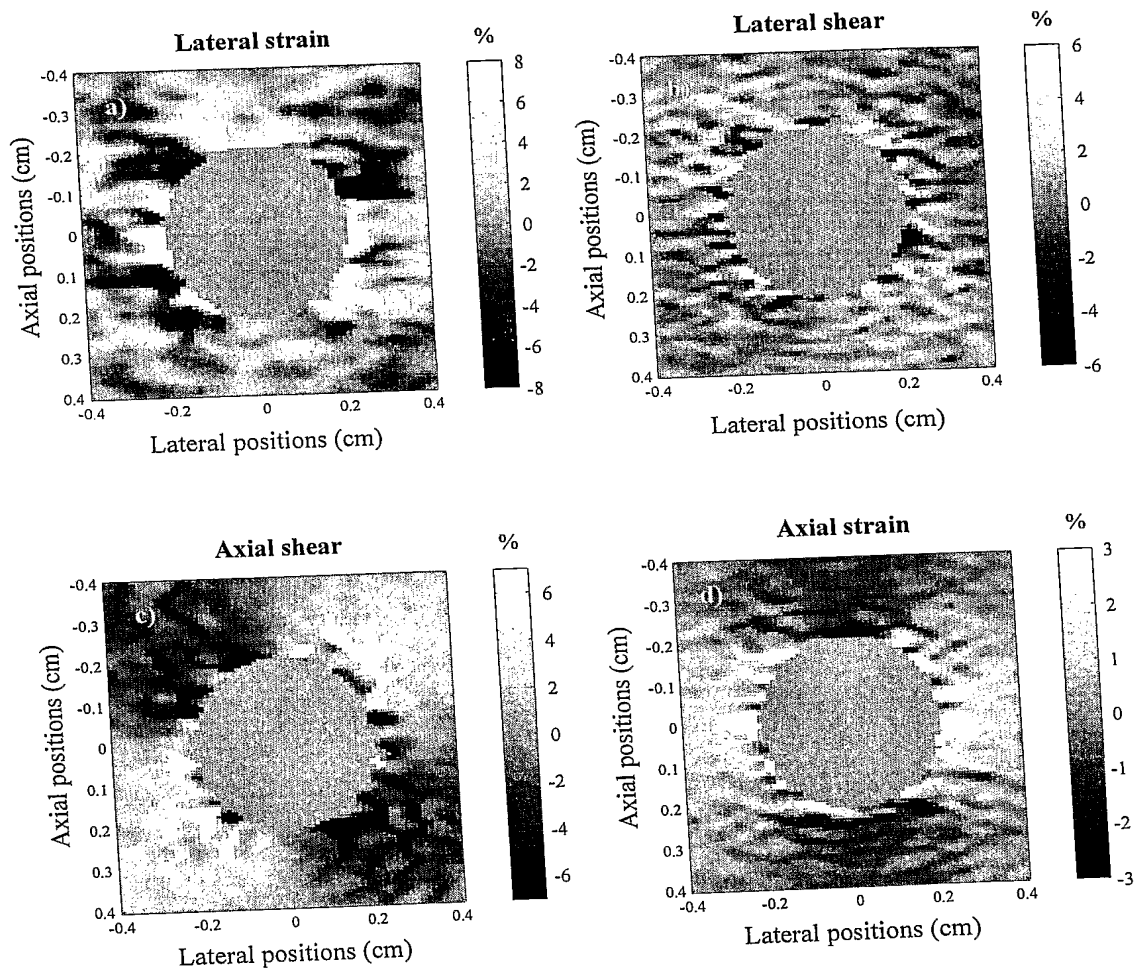


Figure 29

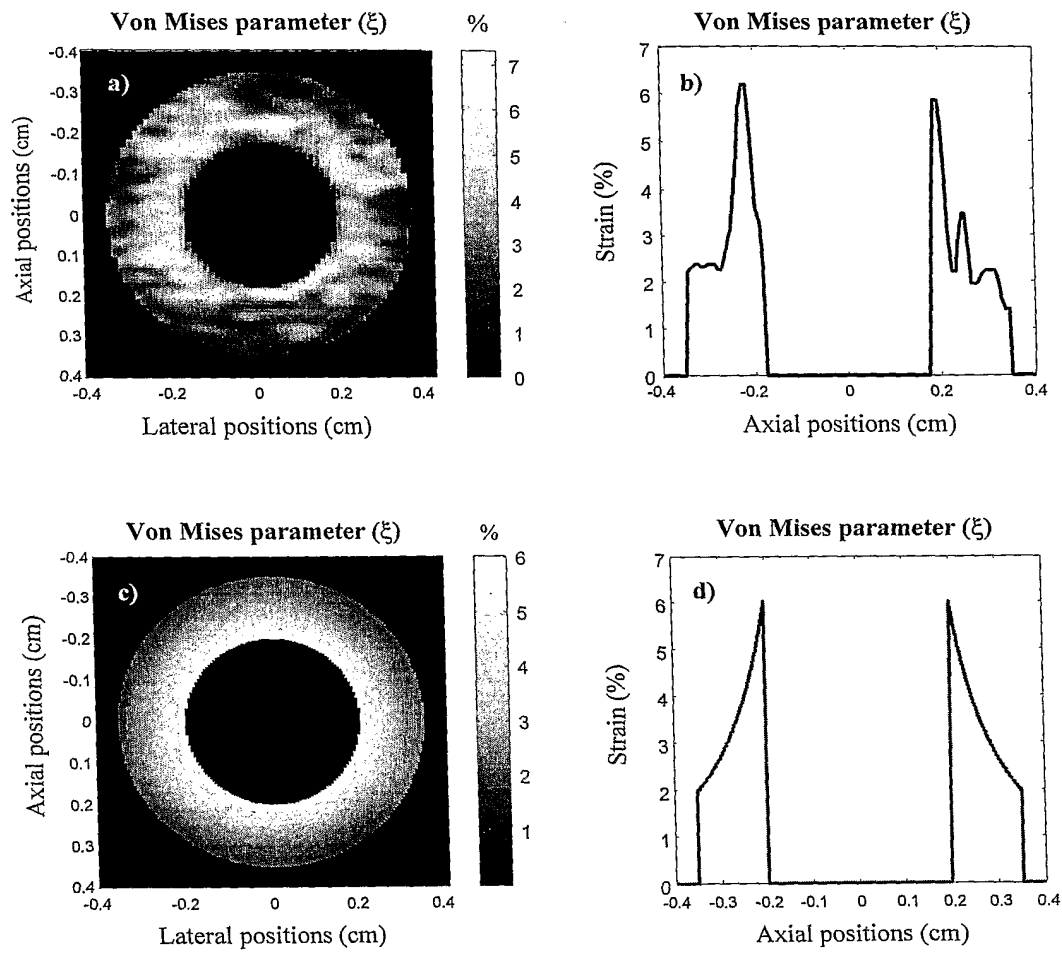


Figure 30

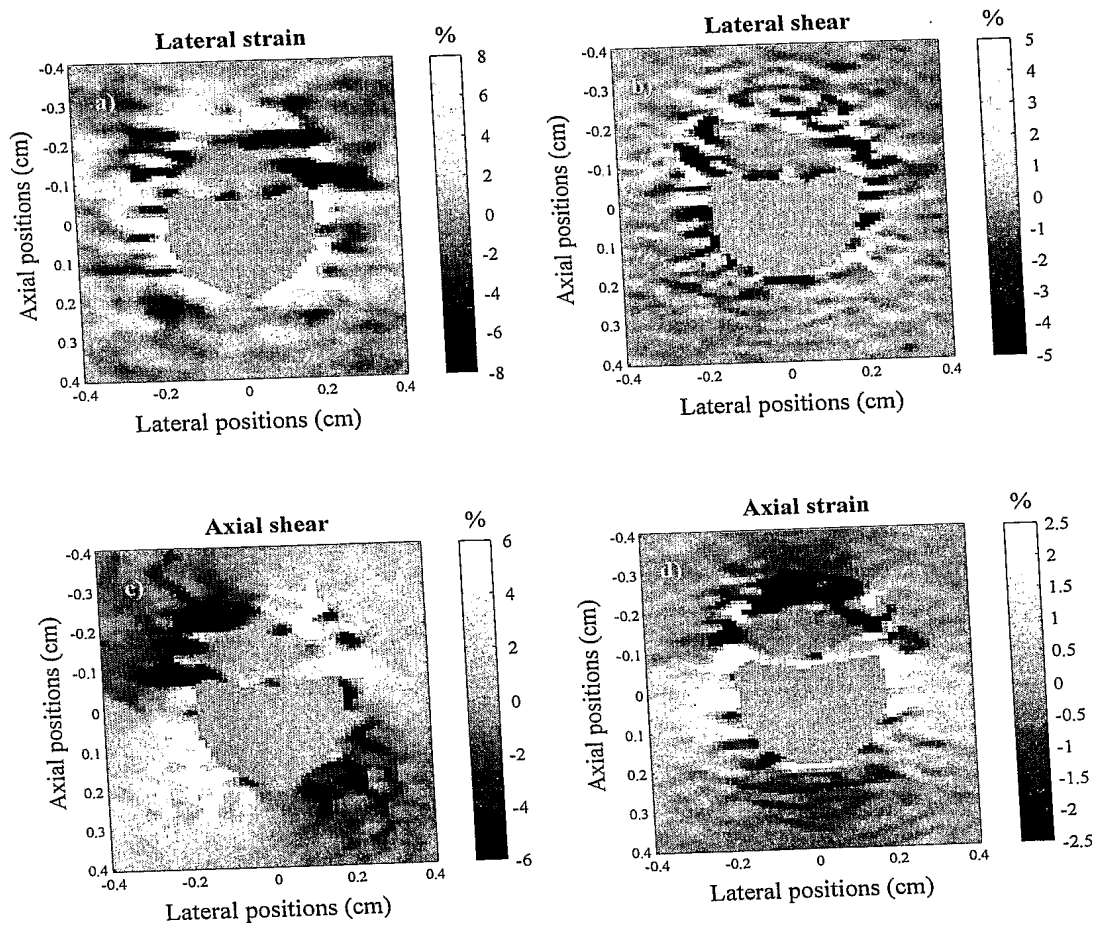


Figure 31

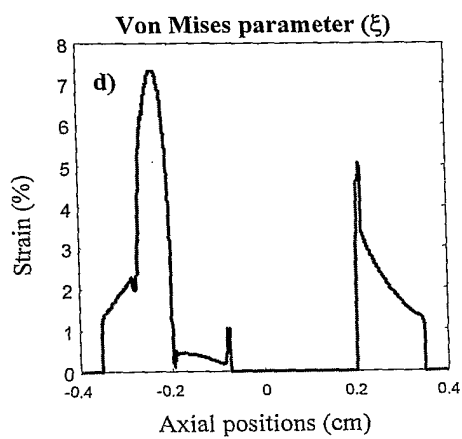
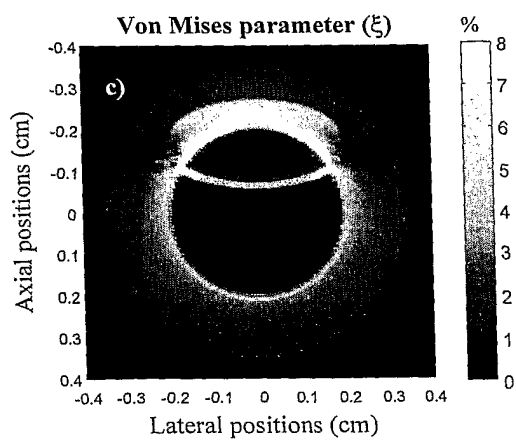
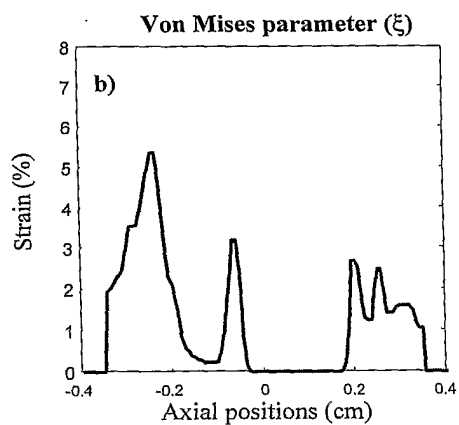
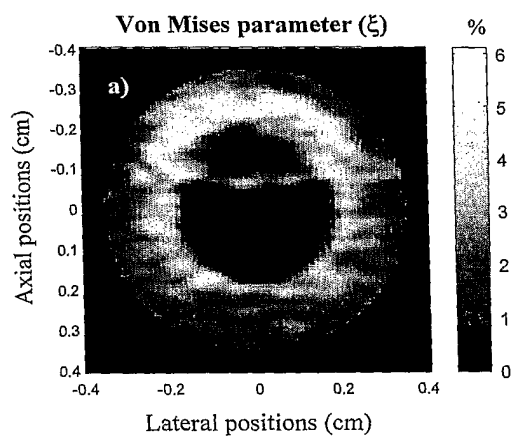


Figure 32

